Reservoir characterization of the Fruholmen and Stø Formations in the Hoop Fault Complex, SW Barents Sea

Reservoir quality as a function of provenance, depositional environment and diagenesis

Anna Clark

Master Thesis in Geosciences

60 credits

Faculty of Mathematics and Natural Sciences

UNIVERSITY OF OSLO

2017.06.01

Reservoir characterization of the Fruholmen and Stø Formations in the Hoop Fault Complex, SW Barents Sea

Reservoir quality as a function of provenance, depositional environment and diagenesis

Anna Clark

Master Thesis in Geosciences

60 credits

Faculty of Mathematics and Natural Sciences

UNIVERSITY OF OSLO

2017.06.01

© Anna Clark, 2017

Acknowledgements

This Master's Thesis was written during my final year of studies at the University of Oslo. I wish to extend my most sincere gratitude to my supervisor, Associate Professor Jens Jahren and co-supervisor, PhD student Lina Hedvig Line for their guidance and encouragement throughout the development of this project.

I would like to thank OMV Norge AS for permission to view and log cores and furthermore collect samples allowing me to develop and advance my knowledge of the reservoir sandstones found in the Hanssen and Wisting Central wells.

Technical support provided at the University of Oslo by Salahalldin Akhavan, Beyene Girma Haile and Berit Løken Berg has been of great value during the progression of this thesis.

Tyler, for the many discussions and your encouragement throughout this year I am forever grateful. Finally, a special thanks to my loving family who have supported me from afar during my many years of studies without whom, I would not be where I am today.

2017

Anna Clark

Abstract

Hydrocarbons have recently been discovered in the Realgrunnen Subgroup in two separate wells (Hanssen 7324/7-2 and Wisting Central 7324/8-1) in the Hoop Fault Complex, Barents Sea. The aim of this thesis is to interpret and analyse processes influencing the quality of reservoir sandstones within the Late Triassic Fruholmen Formation and Early Jurassic Stø Formation.

Sedimentological logging, petrographical analyses and petrophysical analyses have been conducted on core samples and well log data in order to gain an understanding of parameters such as provenance and depositional environment as well as subsequent diagenetic processes, all of which influence the quality of a reservoir. Results are based on individual facies analyses which were categorised during preliminary core logging.

Fruholmen Formation is subdivided into four facies which formed by progradation and compensational stacking of mouth bar and distributary channel elements. Facies 1 and 2 are interpreted as distal mouth bar deposits consisting predominantly of heterolithic fine-grained suspension and traction deposits, showing essentially negligible reservoir potential due to poor porosity and permeability. Facies 3 and 4 demonstrate higher-energy characteristics of a mouth bar and distributary channel environment consisting of compensationally stacked fine-grained sand intervals and mud-rich rip-up clasts. Based on intergranular volume measurements, a majority of porosity is lost due to mechanical compaction whereby reservoir potential for Facies 3 is projected as *fair* whereas Facies 4 shows *poor* reservoir characteristics. Chemical processes such as precipitation of kaolinite and quartz cement are moderately observed throughout Fruholmen Formation, causing further reductions in porosity.

Stø Formation (Facies 6) displays a markedly different depositional environment interpreted as a complex of subaqueous dunes formed in large sandflats within a high-energy shallow marine to fluvial transition zone. The mineralogically mature quartz arenite exhibits good porosity and permeability resulting in a *good* reservoir candidate. Infiltration of allogenic clay seen as partial grain coatings are interpreted to represent an important porosity preserving parameter, limiting the quartz cementation observed in Facies 6.

Based on results, mineralogical composition, depositional environment and diagenetic processes respectively, are of fundamental importance and largely determine the potential of sandstone reservoirs within the Hanssen (7324/7-2) and Wisting Central (7324/8-2) wells.

Table of Contents

1. Introduction

1.1 Aims and Objectives

Hydrocarbons have recently been discovered in the Realgrunnen Subgroup in two separate wells (Wisting Central 7324/8-1 and Hanssen 7324/7-2) within the Hoop Fault Complex, Barents Sea (Norwegian Petroleum Directorate [NPD], 2016). The aim of this thesis is to describe and compare properties of reservoir sandstones within these two wells of Late Triassic and Early Jurassic age. Mineralogical differences across the Triassic-Jurassic transition represented by Fruholmen and Stø Formations respectively are of particular interest. Different parameters such as provenance, climate and depositional environment control initial reservoir properties subsequently followed by subsurface diagenetic processes.

Improved understanding of potential reservoir distribution is of economic importance prior to drilling whereby sedimentological, petrographical- and petrophysical analyses will be conducted.

Porosity and permeability are of main concern when characterizing a reservoir as these determine the potential capacity and rate of fluid flow for hydrocarbons. Mineral composition, sorting and grain size are all factors that influence subsequent diagenetic processes which combined, result in the porosity and permeability seen in today.

1.2 Methods

In order to understand these properties and successfully predict the reservoir quality, sedimentological core logging, XRD-, SEM-, CL- and thin section analyses will be carried out. Results from each subsequent analysis will be illustrated and further associated with provenance, depositional environments and diagenesis. Well log data will be assessed in order to estimate maximum burial depths and temperatures to which sediments have been exposed. Conclusive discussions will determine the potential reservoir properties of Fruholmen and Stø Formations in accordance with reservoir appraisals published by Tissot & Welte (1989).

Access to core material from wells 7324/7-2 (Hanssen) and 7324/8-1 (Wisting Central) is provided by OMV Norge AS.

2. Geological History

2.1 Introduction

During the early 1980's the first major gas discovery was made in the Barents Sea, which has since become an area of great interest for hydrocarbon exploration. These discoveries were made in reservoir rocks of Middle Jurassic age in the Askeladden, North Albatross and Snøhvit Fields (Doré, 1995). Since then studies have been conducted by the United States Geological Survey (USGS), who have further approximated that 30% of the world's undiscovered gas and 13% oil, may reside in the Artic region (Smelror et al., 2009).

Geographically the Barents Sea comprises an area of approximately 1.3 million km^3, bordered by the Norwegian and Russian mainland, the Novaya Zemlya, Franz Josef Land and Svalbard archipelagos, and the eastern margin of the Atlantic Ocean (Doré, 1995) (Figure 2.1). The offshore Barents Shelf is further subdivided into an eastern and correspondingly western province, separated by a large north-south trending monoclinal structure (roughly coinciding with the disputed border between Norway and Russia) (Worsley, 2008).
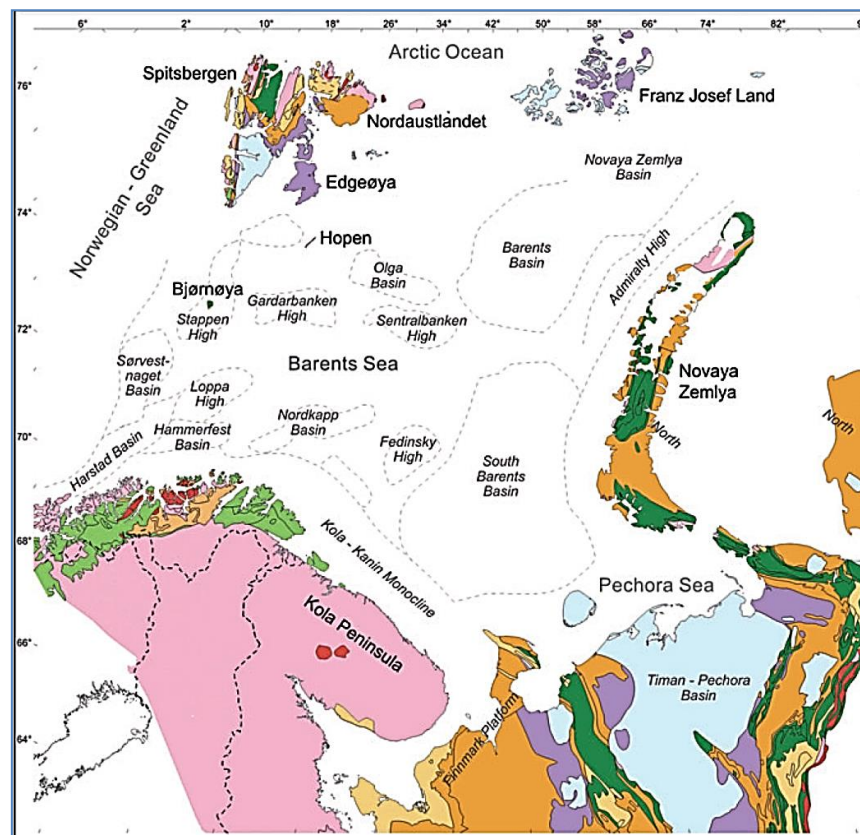
Figure 2.1: Geographical position and bordering land areas of the Barents Sea *(after Worsley, 2008).*

The aim of this chapter is to illustrate the main tectonostratigraphic development of the southwestern Barents Sea, focusing primarily on the Hoop Fault Complex and adjacent areas.

2.2 Regional Tectonic Framework

The Barents Sea encompasses a vast area of geologically complex structures formed by compressional and subsequent extensional events. The eastern province, consisting primarily of two large basins (the Northern and Southern Barents basins) was created principally in the foredeep of the Uralian orogeny (Worsley, 2008; Doré, 1995). These major basins contain significant Triassic deposits, locally 6-8 km thick (Doré, 1995). The creation of the Uralides (Late Palaeozoic to Mesozoic) causes the Barents Sea area to differ from basins in the North Sea and the mid-Norwegian shelf by influences from a younger tectonostratigraphic event (Ryseth, 2014). The western Barents Sea is geologically speaking, more complex, comprising basins, platforms and structural highs formed mainly by intermittent rifting episodes (Worsley, 2008). The Hoop Fault Complex is located between $72^{°}$ 50'N, $21^{°}$ 50'E and $74^{°}$ 26'E and is thus situated in the southwestern region of the Barents Sea (Gabrielsen et al., 1990) (Figure 2.2). Therefore, further detailed discussions will focus on the western Barents Sea not taking into account the tectonostratigraphic development of the eastern Barents Sea.
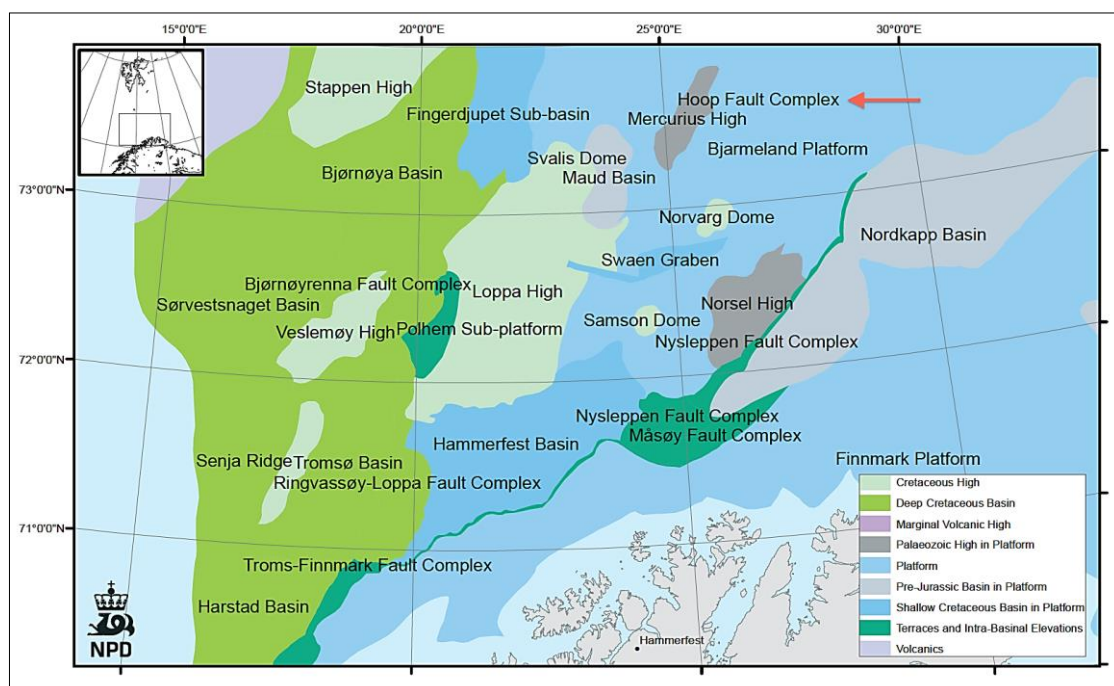
Figure 2.2: Main structural elements of the southwestern Barents Sea. Arrow depicting the Hoop Fault Complex (*modified after NPD, 2016*).

The evolution of the Barents Sea has been interpreted in several previous works (e.g., Worsley, 2008; Doré, 1995; Faleide et al., 1984; Henriksen et al, 2011; Smelror et al., 2009), sub-dividing and classifying the progression of events in a varying manner. However, to grasp the main tectonostratigraphic proceedings taking place from the Caledonian orogeny to present, a consecutive description of the geological time periods will be used herein based on previously listed references.

2.2.1 Tectonic and Stratigraphic Evolution of the Southwestern Barents Sea

Tectonostratigraphic development of the southwestern Barents Sea reflects an interplay between the continuous northward movement of the Eurasian plate resulting in climatic changes, tectonic processes comprising compressional, transpressional and transtentional stresses and finally a varying local and regional sea-level fluctuation (Henriksen et al., 2011).

Starting from the equatorial zone in the Middle Devonian to a paleolatitude of 20˙N in the Carboniferous, 55˙N in the Triassic to its present location in the Artic, climate variations are reflected throughout the stratigraphy (Doré, 1995; Worsley, 2008). Caledonian and Uralide compressional stresses followed by several rift phases are evident in the complex bathymetry resulting in platforms, basins and structural highs and further affecting sediment distribution patterns (Henriksen et al., 2011). Ultimately, local and regional sea-level fluctuations contributed to the substantial sequence stratigraphy seen in present day drill cores (Worsley, 2008).

Ordovician - Devonian

The Caledonian orogeny, caused by the suturing of western Europe and eastern North America/Greenland set the initial framework for impending tectonic events in the western Barents Sea (Figure 2.3.A). The metamorphic rocks created during this orogeny form much of the basement rock observed on mainland Norway and is likely to continue offshore to the Barents Sea, appearing once again on mainland Svalbard (Breivik, 1998). Remnants of this amalgamation of plates can be seen in exposed bedrock on Svalbard, represented by a N-S strike, whereas a NE-SW structural grain trend general dominates the southwestern Barents Sea and Finnmark (Doré, 1995; Smelror et. al., 2009).

Subsequent tectonic events exploited this area of weakened crust, which evolved into early rift basins and ultimately led to the opening of the Norwegian-Greenland Sea (Smelror et. al., 2009; Worsley, 2008).
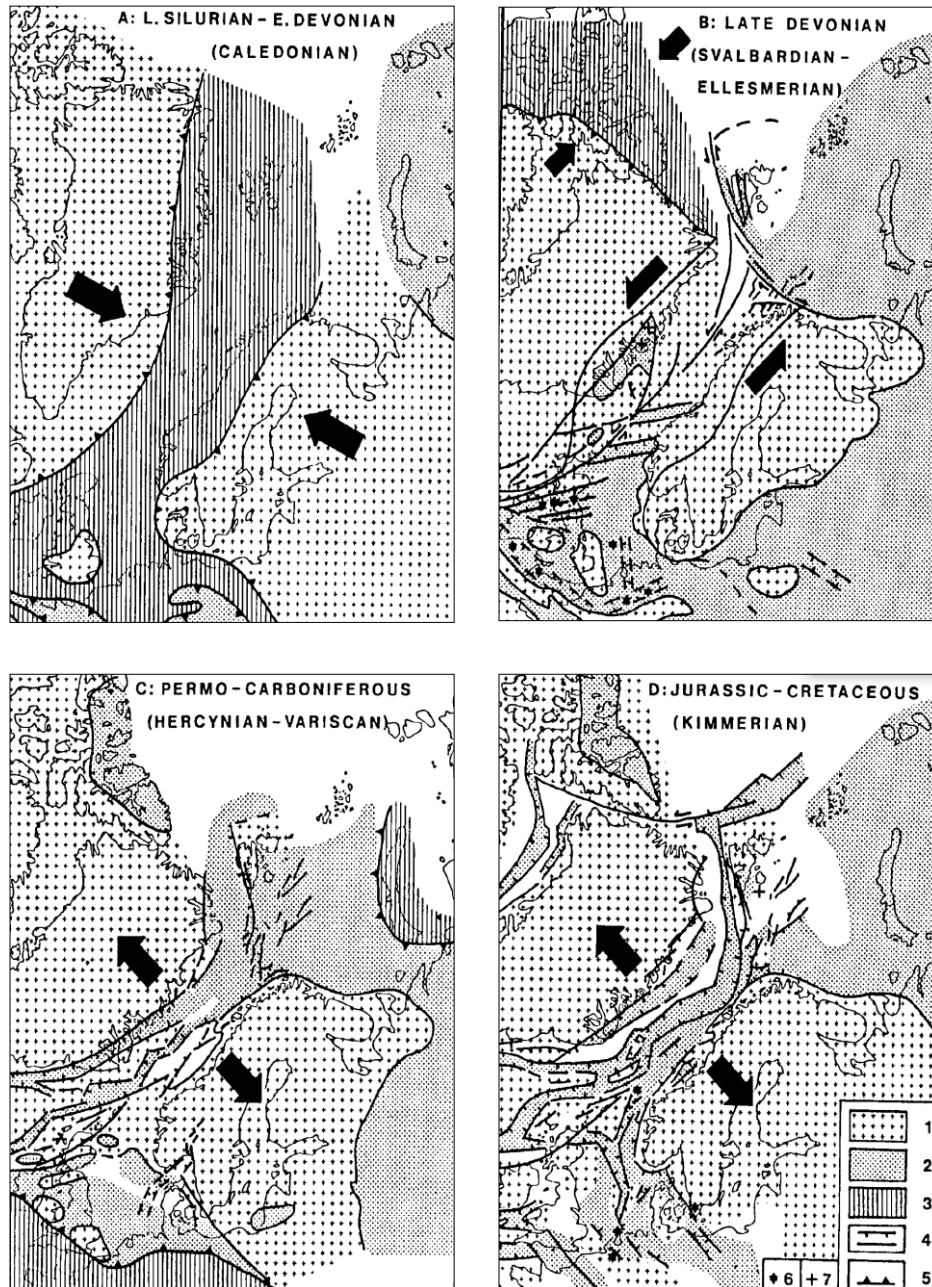
Figure 2.3: Schematic configuration showing the main geodynamic components during the creation of the southwestern Barents Sea *(after Faleide et al., 1984)*. **1. Stable elements (continental cratons and intrabasinal highs); 2. Sedimentary basins; 3. Active foldbelts; 4. Normal- and wrench fault; 5. Deformation front of active foldbelts; 6. Intrusions; 7. Volcanics.**

The collapse of the Caledonian orogeny (Early to Middle Devonian) is marked by intense erosion of the hinterland, distributing sediments in an easterly direction across the Barents Shelf (Gabrielsen, 1984; Henriksen et al., 2011). Extensional collapse of the Caledonian orogeny represents the onset of early rift basins and local half-grabens developing along previously mentioned Caledonian structural features (Figure 2.3.B) (Breivik, 1998; Smelror et. al., 2009; Worsley, 2008).

Carboniferous

Rifting continued throughout the Carboniferous forming a fan-shaped array of half-grabens and highs with geometries trending NE-SW (Figure 2.3.C) (Glørstad-Clark et al., 2010). These structural developments persistently follow zones of basement weaknesses corresponding with Caledonian trends (Henriksen et al., 2011). Two main rift phases are interpreted by Gudlaugsson et al. (1998), the initial one occurring during Middle Carboniferous and affecting the entire southwestern Barents Shelf and another of lesser magnitude taking place throughout the Permian to Early Triassic. This main rift pulse is associated with the formation of several prominent sedimentary basins seen in the southwestern Barents Sea today, namely Tromsø, Bjørnøya, Nordkapp, Fingerdjupet, Maud and possibly Hammerfest (Henriksen et al., 2011).

Middle Carboniferous also marks the onset of the continental collision between Baltica and the West Siberian Craton, affecting a widespread area. This collision started in the south and propagated northwards, reaching the eastern Barents Sea by Late Carboniferous to Early Permian (Smelror et al., 2009).

Three lithostratigraphic groups (Billefjorden, Gipsdalen and Bjarmeland) are defined from the Carboniferous to Mid-Permian depicting different depositional regimes, limited by abrupt changes in tectonic, climatic and sea-level factors (Worsley, 2008) (Figure 2.6).

The western Barents Shelf generally portrays a tropical humid climate during Late Devonian-Early Carboniferous, shifting to sub-tropical and arid by Late Carboniferous (Henriksen et al., 2011). The overall depositional environment noted from the Billefjorden Group (Early Carboniferous-Middle Carboniferous) is of fluvial and lacustrine origin, depositing continental sandstones, mudstones and coal into the newly formed basins (Worsley, 2008). Following the change in climate and paralleled with a transgression from the west, a widespread change in depositional environments is seen from the siliciclastic Billefjorden Group to carbonates and evaporites in the Gipsdalen Group (Henriksen et al., 2011; Smelror et al., 2009).

Permian

The second rift phase affecting the Barents Sea (Norwegian-Greenland rift system) commenced in the Permian and continued through to the Triassic (Smelror et al., 2009; Glørstad-Clark et al., 2010). According to Gudlaugsson et al. (1998) this rift phase affected a N-S structural trend as opposed to the previously mentioned Carboniferous NE-SW trending rift phase.

Deposition of evaporites is thought to have lasted into the Early Permian and accumulated vast thicknesses in several basins, 4-5km in the Nordkapp Basin, 2-2,5km in the Maud Basin close to the Hoop Fault Complex and a minimum of 2km in the Ottar Basin (Gudlaugsson et al., 1998). However, it is believed that the continuous development of the Urals as well as the closure of seaway connections to the Tethys caused a major shift in the depositional environment. By Late Permian the climate had changed from sub-tropical and arid to temperate, consequently followed by a change in the depositional environment (Henriksen et al., 2011). This is seen in the Bjarmeland and Tempelfjorden Groups (Figure 2.6), changing from previously carbonate-dominated successions and giving rise to marine mudstone and spiculitic chert deposition within basins, and interbedded sandstone and limestone on local highs (Worsley, 2008).

Triassic

The Barents Sea was located at approximately 50ºN to 55ºN during the Triassic and endured a warm and humid climate. Tectonically this time period represents general quiescence in the southwestern Barents Sea. However, regional subsidence and vast sediment accumulations are characteristic features of the Late Permian-Early Triassic periods (Henriksen et al., 2011; Glørstad-Clark et al., 2010). This widespread subsidence is seen throughout the Barents Sea and may be associated with the on-going subduction and subsequent orogeny of the Urals, consequently forming the large North and South Barents Sea Basins in a back-arc spreading setting (Breivik, 1998). The stratigraphic sequences of the Triassic (Sassendalen and partly Kapp Toscana Groups) are seen as thick sandstone dominated successions deposited during several regional regressive-transgressive cycles (Henriksen et al., 2011).

Figure 2.4 shows an interpreted palaeogeographic setting from the
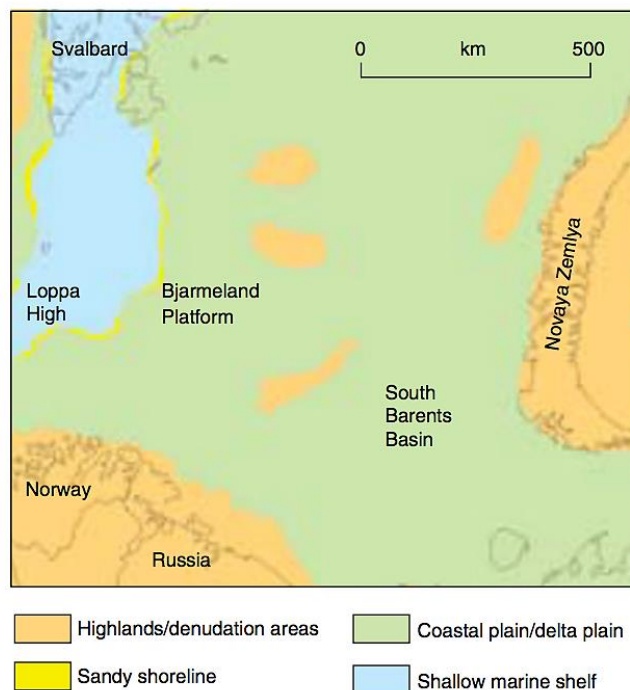

Figure 2.4: Palaeogeographic setting in the southwestern Barents Sea during the Late Triassic *(modified after Henriksen et al., 2011 in Ryseth, 2014).*

Late Triassic, emphasizing the extensive coastal/delta plain environment that is believed to have extended from Novaya Zemlaya and Timan Pechora towards a marine seaway located between the western Barents shelf and the Greenland landmass (Ryseth, 2014). Sediment provenances are interpreted to originate primarily from the Baltic shield with a successive increase of sediment input from the Uralian orogeny in the east, essentially reversing sedimentation patterns (Smelror et al., 2009; Worsley, 2008; Ryseth, 2014).

A large prograding deltaic system initiated in the Middle Triassic developing towards the north-west and giving rise to more proximal sandstone deposits (Worsley, 2008). These thick sandstone deposits are of interest for hydrocarbon exploration. Reservoir quality has been proven to increase vertically throughout the Triassic sandstones due to extensive diagenetic alterations affecting the more deeply buried successions. Parts of these successive sand deposits (belonging to the Kobbe Formation) have recently been discovered to be hydrocarbon bearing (Worsley, 2008). The sequence stratigraphic units of the Late Triassic will be further elaborated in section 2.2.3 (Realgrunnen Subgroup) as this includes the Fruholmen Formation.

Jurassic

The Triassic to Jurassic boundary is associated with a more humid climate, which can be related to continuous north-directed plate-tectonic drift in addition to the initial break-up of Pangea (Doré, 1995; Worsley, 2008; Bergan & Knarud, 1993). This fragmentation of continents caused widespread release of CO_2 to the atmosphere and oceans and may have had extensive effects on the climate (Ryseth, 2014).

The Late Triassic-Middle Jurassic time period is one of great importance from a reservoir standpoint and encompasses four formations within the Realgrunnen subgroup (Henriksen et al. 2011) (Figure 2.7). A decrease in previously mentioned subsidence was accompanied by a reduction in sedimentation rates, however still reflecting similar provenance areas resulting in what is today known as the Fruholmen Formation (Worsley, 2008).

A shift in provenance is believed to have taken place during the Early Jurassic leading to a change in mineralogical composition seen in the mature sandstones of the Stø Formation (Pozer Bue & Andresen, 2002). The mineralogical difference between Fruholmen and Stø Formations is of great interest due to the potential disparities in reservoir quality it may produce and will be discussed further in this study. During the Early Jurassic (Hettangian-Pliensbachian) large areas of the Barents Shelf were exposed to erosion and a

prominent hiatus in the sequence stratigraphy exists (Figure 2.7). This non-depositional environment was followed by a transgression in the Late Jurassic causing an extensive marine shelf to prevail over most of the Barents Shelf. This is depicted by a dominance of organic rich shale and mudstone deposits (Smelror et al., 2009) seen in the Hekkingen Formation, which is moreover an important source rock in the Barents Sea (Worsley, 2008).

Rifting in the Atlantic progressed northwards mainly affecting the southwestern province causing rotated fault blocks to form. These rotated fault blocks have furthermore proven to act as oil traps in places (Smelror et al. 2009). The rifting events seen through the Middle Jurassic to Early Tertiary generally formed large, deep-seated normal faults and rift basins such as Bjørnøya, Tromsø and Harstad, and are furthermore precursory to subsequent seafloor spreading (Smelror et al. 2009; Faleide et al., 1984; Glørstad-Clark et al., 2010) (Figure 2.3.D).

Cretaceous

The rift system dominating the southwestern Barents Sea during the Jurassic period terminated in the Early Cretaceous, laying the structural foundation of present day basins and highs. Thick successions of shale are seen within basins (such as Tromsø and Sørvestsnaget basins) and are related to continuous subsidence within the western margins of the Barents Sea (Henriksen et al., 2011) (Figure 2.6). Ultimate seafloor spreading initiated during the Early Eocene and is signified by a prevailing dextral shear movement between Greenland and the Barents Sea (Breivik, 1998).

Cenozoic

Shearing along the ocean-continent boundary (Senja Fracture Zone) along with sustained northward propagation of ocean-floor spreading characterises the on-going tectonism during the Cenozoic. By Oligocene a passive margin had developed as a consequence of incessant sea-floor spreading (Henriksen et al., 2011).

Late Pliocene marks the onset of large-scale glaciation manifested by a major unconformity between Mesozoic-Cenozoic strata and subsequent glacial deposits (Smelror et al. 2009) (Figure 2.6). Intermittent glacial driven subsidence and subsequent isostatic rebound resulted in severe uplift and erosion of sediments in the Barents Sea and on mainland Norway. This vast accumulation of eroded sediments was re-deposited as clastic wedges along the western margin of the Barents Shelf (Faleide et al., 2015). Estimated exhumation maps of the Southwestern Barents shelf have been published by Baig et al. (2016) and are shown in Figure 2.5.
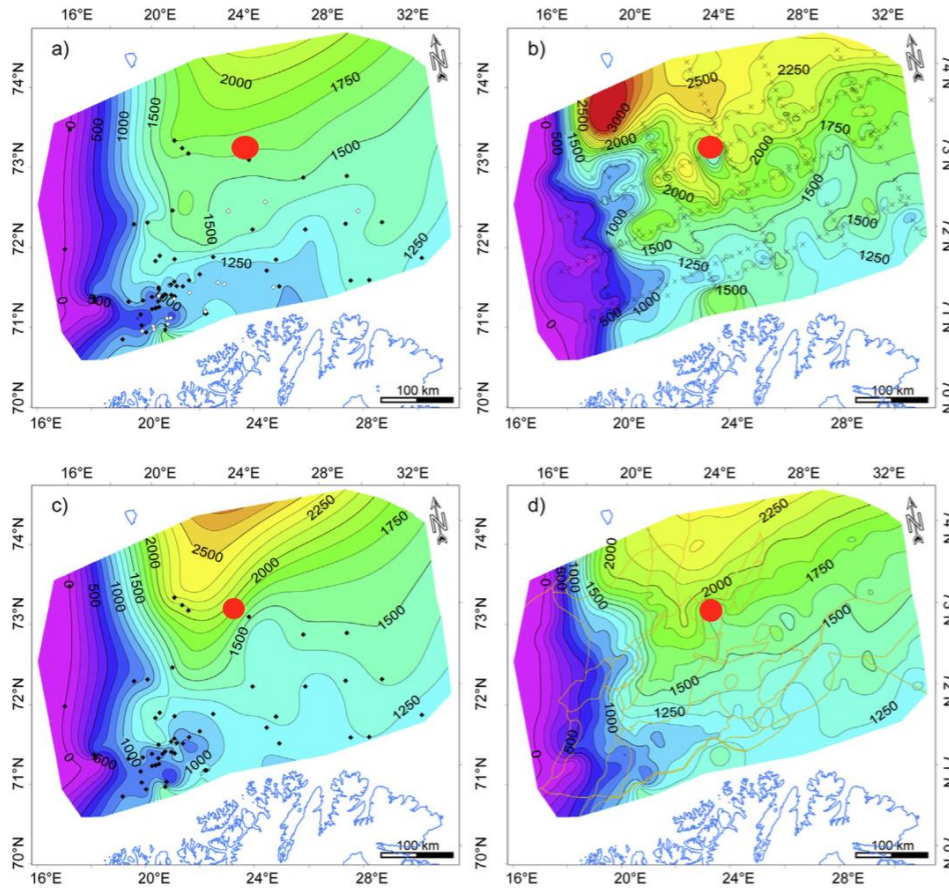
Figure 2.5 Estimated exhumation maps from a) sonic logs, b) shot gathers, c) vitrinite reflectance and d) average net exhumation from the three data sets *(modified after Baig et al., 2016).* **Approximate positions of Hanssen (7324/7-2) and Wisting Central (7324/8-1) are marked by red circles (73º29'N, 24º14'E and 73º27'N, 24º24'E respectively).**

2.3 Study Area

A growing interest in the Hoop Fault Complex has transpired due to six wells being drilled within recent years, two of which contained light oil and two gas discoveries. What differentiates these discoveries from previously drilled wells in the southwestern Barents Sea is the remarkably shallow depth in which they are located. Normal prospect depths commonly appear around 2-4km below the seafloor, which may cause uncertainties to transpire when interpreting seismic data. The recently discovered reservoirs found in Jurassic sandstones within the Hoop Fault Complex are typically less than 1000m below the seafloor. The effect of this shallow play increases the interest for further oil and gas exploration in the area as it enables companies to reduce their risk when investing due to more reliable data (Kjølhamar, 2015).
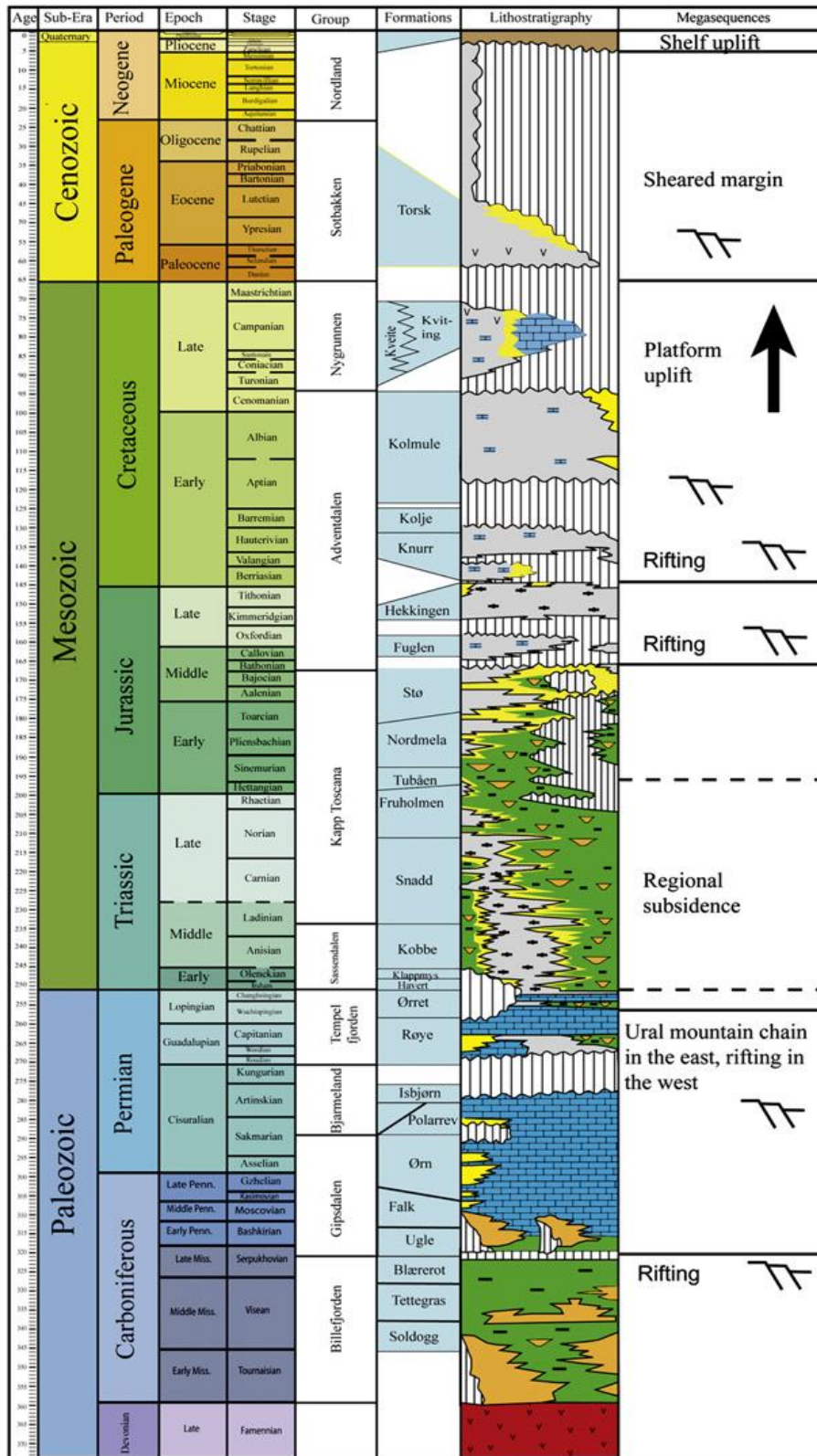
Figure 2.6: Schematic diagram of the lithostratigraphy and associated mega sequences of the western Barents Sea *(modified after Glørstad-Clark et al., 2010).*

2.3.1 Hoop Fault Complex

Geographically, the Hoop Fault Complex is located between $72^{°}$ 50'N, $21^{°}$ 50'E and $74^{°}$ 26'E and cuts across the Loppa High and the Bjarmeland Platform, separating the Maud

Basin from the Mercurius High (Gabrielsen et al., 1990; Fitriyanto, 2011) (Figure 2.2). Furthermore, the area is divided into three segments: a northern, central and southern part. The northern segment is characterised by normal faults cutting the Bjarmeland Platform, the central area is related to the development of the Maud Basin and the Svalis Dome whereas the southern part relates to a narrow graben on the Loppa High (Gabrielsen et al., 1990).

According to Gabrielsen et al. (1990), the Hoop Fault Complex is interpreted as an old zone of weakness, meaning that tectonic events exploited the already weakened crust. The fault complex follows a NE-SW trending lineament, which thus coincides with the structural grain of the Caledonian orogeny (within the southwestern Barents Sea) (Gabrielsen et al., 1990; Smelror et al., 2009). Structurally, the Hoop Fault area developed through multiple phases of extension (Mid Triassic – Late Jurassic) forming a complex network of normal faults (Gabrielsen et al., 1990; Gabrielsen et al., 2016). Studies published by Kjølhamar (2015), show that an interplay between ductile and brittle faulting created the offsets seen in seismic data today. According to new experimental studies conducted by Gabrielsen et al (2016), the style of faulting seen in the Hoop Fault Complex is dependent on the heterogeneity of strata therein, caused by mechanically stronger and respectively weaker layers. Evaporite sequences are prime candidates for weak interlayers within stratigraphic sequences and may form detachment horizons that mechanically decouple and influence the geometry and growth of faults.

Generically, when interpreting multistage extensional fault systems, a systematic increase in accumulated heave is seen with depth, due to older stratigraphic sequences having experienced greater momentum. However, when mechanically weaker layers are present, these are able to accommodate and relieve strain that would otherwise have caused offset. This results in an unsystematic faulting system and difficulties transpire when attempting to calculate accumulated heave in the faulted area. For further information and study results regarding multistage extensional rifting within heterogenetic layers see Gabrielsen et al. (2016).

The recent hydrocarbon discoveries within the Hoop Fault Complex are located within the Realgrunnen subgroup, ranging from Late Triassic–Middle Jurassic and will be further elaborated in the following section.

Figure 2.7: Lithostratigraphy of the Triassic, Jurassic and Cretaceous Formations in the Hoop Fault Complex and adjacent Bjarmeland Platform. Note that Tubåen and Nordmela are partially or completely absent in the Hoop Fault Complex *(after OMV Norge AS, 2016.)*

2.3.2 Realgrunnen Subgroup

The Realgrunnen subgroup consists of four formations: Fruholmen, Tubåen, Nordmela and Stø (Figure 2.7) spanning from Early Norian to Late Bajocian. The Late Triassic succession within the Hoop Fault Complex is interpreted by Kjølhamar (2015) to consist of large-scale deltaic deposits followed by channelized coastal plain deposits, both of which have good reservoir potentials. Triassic sandstone successions across e.g. the Bjarmeland Platform typically contain abundant plagioclase feldspars derived from the Uralides (Mørk, 1999). The Jurassic succession consists of sandstone thicknesses of up to 70m in places and is typically quartz-rich and depleted in feldspars (Bergan & Knarud, 1993). These successions are of main interest for further exploration due to the previously mentioned light oil discovery and will be further explained successively using interpretations from reference cores in the Hammerfest basin published by NPD (2014), Ryseth (2014) and Berglund et al. (1986).

Fruholmen Formation

The onset of Fruholmen Formation is interpreted as a major marine incursion taking place on a regional scale in the Barents Sea (Henriksen et al., 2011). Fruholmen Formation (Early Norian to Rhaetian) depicts a general coarsening upwards trend, comprised of dark mudrocks and interbedded sandstones, and subsequently overlain by coal-bearing heterolithic deposits (Ryseth, 2014; NPD, 2014). The boundary with underlying Snadd Formation is interpreted as a major Early Norian transgression seen as organic marine shale deposits (Henriksen et al., 2011). The marine shales successively pass into coastal and

fluvial dominated sandstone (NPD, 2014). The upper coal-bearing stratum is related to flood plain deposits (Ryseth, 2014). According to further interpretations by NPD (2014) these successions represent a fluviodeltaic progradation with a depocentre to the south.

Tubåen Formation

Tubåen Formation is absent in both Hanssen (7324/7-2) and Wisting Central (7324/8-1) wells signifying a prominent hiatus. With reference to the Hammerfest basin, Tubåen Formation (Late Rhaetian to Sinemurian) consists of sandstones with subordinate mudrocks and thin coal layers (Ryseth, 2014; NPD, 2014). Generally speaking, the formation can be separated into a lower and upper sand-rich unit with a more shale-rich interval in between (NPD, 2014). The sand-rich units are interpreted as fluvial deltaic origin, representing a variety of fluvial and distributary channel types (Ryseth, 2014). The shales reflect a more distal marine environment in the northwest while the coal layers are interpreted as protected backbarrier lagoonal deposits to the southeast (NPD, 2014). Tubåen Formation represents a significant change in fluvial style across the Barents Sea in contrast to underlying units, comprising a higher degree of sandstone successions and less interbedded fine-grained deposits (Ryseth, 2014).

Fruholmen and Tubåen Formations together represent significant delta progradation and widespread delta plains dominating from the Late Triassic through Early Jurassic. The Hettangian to Sinemurian stages are presumed to represent maximum regression (Ryseth, 2014).

Nordmela Formation

Nordmela Formation is interpreted to represent an approximately 4m interval in Hanssen (7324/7-2) (Pers. Com. Reidar Müller) and is consequently logged thereafter in this study. Wisting Central (7324/8-1) however is questionably lacking Nordmela Formation entirely, representing a larger hiatus between Fruholmen and Stø Formations.

According to NPD (2014), "Nordmela Formation (Sinemurian-Late Pliensbachian) consists of interbedded siltstones, sandstones, shale and mudstones with minor coals". The varied succession is interpreted as being deposited within a tidal flat to flood-plain environment. Stratigraphic studies conducted in the Hammerfest Basin and described by NPD (2014) show that Tubåen and Nordmela Formations both illustrate a west-southwest thickening wedge (Figure 2.8). The hiatus observed in Wisting (7324/8-1) and partly in Hanssen (7324/7-2) (Tubåen and Nordmela Formations) represents millions of years of

missing data whereby a vast change in mineral composition and depositional environment is expectedly seen in subsequent deposits of Stø Formation.

Stø Formation

Stø Formation (Late Pliensbachian to Bajocian) consists mainly of mineralogically mature, well-sorted sandstones, deposited in a prograding coastal regime (NPD, 2014). Wave processes have played an important role in producing the textural maturity that is seen throughout the sand deposits. A general fining-upwards trend can be seen throughout the upper portion of Stø with an increasing frequency of interbedded mudstones and bioturbation (Berglund et al., 1986). Fine-grained intervals are thought to represent regional transgressive pulses in the Late Toarcian and Late Aalenian. In accordance with the previous two formations, Stø thickens westward (NPD, 2014) (Figure 2.8).
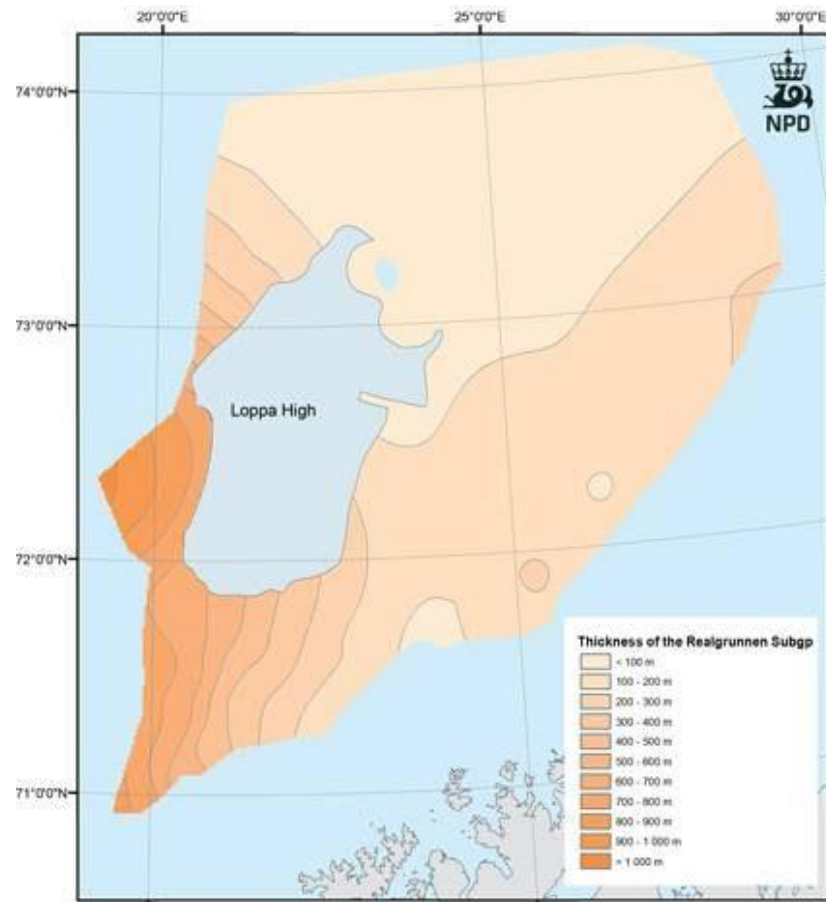
Figure 2.8: Sediments of the Realgrunnen Subgroup characteristically showing west-southwest thickening (after NPD, 2014

3. Theoretical Background

3.1 The Petroleum System

A petroleum system is defined by Magoon & Dow (1994) as: "A natural system that encompasses a pod of active source rock and all related oil and gas and includes all the essential elements and processes needed for oil and gas accumulations to exist". These essential elements are further listed as; source rock, reservoir rock, seal rock (cap rock), and overburden rock. The necessary processes involved are; trap formation, the generation-migration-accumulation of petroleum and preservation time, all of which must be placed in a spatial and timely order. This systems chart event will be briefly explained so as to show the complex history and necessary elements involved when analysing a petroleum system (Magoon & Dow, 1994).

The first four events (source rock, reservoir rock, cap rock and overburden rock) describe the depositional environments based on stratigraphic studies. The two following events (trap formation and generation-migration-accumulation) compile the time during which a petroleum system process takes place. Ultimately, preservation time is the time in which hydrocarbons within a petroleum system are preserved, modified or destroyed (Magoon & Dow, 1994).

When evaluating potential petroleum systems all elements of the chart are of fundamental importance, and a diverse field of expertise is necessary. To further understand how reservoir quality is assessed, this chapter intends to describe the processes and repercussions from deposition (textural properties and mineralogical composition) to diagenesis (near surface and burial).

3.1.1 Reservoir Rocks

Porosity and permeability are two of the controlling factors when determining the quality of a sandstone reservoir. In order for petroleum accumulations to form, pores are essential in a reservoir enabling storage of hydrocarbons, whereas permeability (interconnectivity of pores) permits secondary migration (Tissot & Welte, 1984). Besides being important aspects for hydrocarbon capacity and migration, porosity and permeability are also imperative for chemical reactions to take place. Subsurface chemical reactions require water, without which, diagenesis would effectively cease (Blatt, Tracy & Owens, 2006; Worden & Burley, 2003).

These determining factors are dependent on primary composition, grain size and sorting (depositional environment), climate and early diagenetic processes (Bjørlykke & Jahren, 2015; Blatt, Tracy & Owens, 2006). Pore diameters are also of critical importance, if these are smaller than a definitive minimum size, capillary forces will be too high to overcome and fluid flow will be negligible. Thereby, a relationship between porosity and permeability can be established, illustrating that fine-grained sandstones are typically less permeable than medium to coarse grained sandstones (Blatt, Tracy & Owens, 2006).

Sandstones commonly consist of sedimentary particles ranging between 0.05 and 0.25mm in diameter, which results in average pore radii of 20 and 200µm respectively (Tissot & Welte, 1984). Reservoir porosities commonly vary between 5 to 30% and can be summarized in terms of permeability (in millidarcy) and quality as depicted in Table 3.1. Initial depositional porosity of sand is estimated between 40-45%, permitting high permeability. However, due to compaction and potential cementation succeeding deposition, permeability decreases significantly (Blatt, Tracy & Owens, 2006).

Table 3.1: Reservoir quality characterised in terms of porosity and permeability *(after Tissot & Welte, 1984).*

POROSITY %	APPRAISAL	PERMEABILITY IN MILLIDARCY
0 – 5	Negligible	-
5 – 10	Poor	-
10 – 15	Fair	1.0 – 10
15 – 20	Good	10 – 100
20 – 25	Very Good	100 – 1000

To summarize the main characteristics of a reservoir, Bjørlykke (2015) lists four principle features:

1. The spatial extent of a reservoir (controlled principally by depositional environments).
2. The average porosity, pore size and pore geometry.
3. The permeability, detecting fluid conduits or possible fluid barriers.
4. The constituent mineralogy and wettability of pores.

3.2 Sediment Provenance and Depositional Environment

Sandstones can be classified using a three-dimensional ternary diagram, indicating provenance and depositional environment. As described by Bjørlykke & Jahren (2015), this classification system is based on: "The relationship between the relative quantity of sand-sized grains, the composition of the sand grains, and the clay and silt content (matrix)".

According to Dott (1964) the composition of sandstone is subdivided into arkoses, lithic sandstones and quartz arenites depending on the percentage of constituent minerals (Figure 3.1). Quartz arenites consist primarily of quartz (containing less than 5% feldspar or lithic fragments) and place at the top of the ternary diagram. These are typically mature sandstones that have been reworked, causing essentially all unstable minerals to break down and weather as well as clay particles to wash out. Sandstones containing more than 25% feldspar are classified as arkoses and commonly originate from granites and gneisses. In contrast to quartz arenites, arkoses are typically not exposed to severe weathering, preserving the constituent feldspar grains. To retain a high degree of feldspar, rapid erosion and short sediment transport distances are required which can in turn indicate what type of palaeoclimate and depositional setting the sandstone was exposed to. However, feldspars are chemically unstable during early burial if exposed to a high flux of meteoric water. Mineral alteration transpires by leaching of feldspathic grains and precipitation of e.g. pore-filling kaolinite (Bjørlykke & Jahren, 2015). Lithic arenites contain rock fragments and are typically derived from very fine-grained sedimentary rocks or basalts and intrusive igneous rocks (Bjørlykke & Jahren, 2015).

Clay is a constituent element of most sandstones and can either be deposited along with framework grains (allogenic) or, can precipitate as a consequence of mineral alteration (authigenic) (Nichols, 2009).
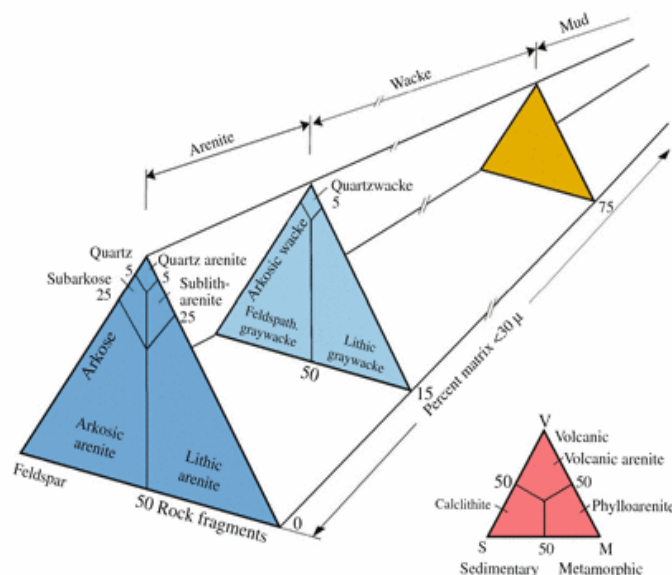
Figure 3.1: Three-dimensional ternary diagram presenting the sandstone classification system according to Dott, (1964) *(after Bjørlykke & Jahren, 2015).*

Authigenic clays are seen as pore linings, pore fillings, pseudomorphous replacements or fracture fillings (Wilson & Pittman, 1977), however these are post-depositional and do not influence initial sandstone classification. In terms of sandstone classification, the percentage of allogenic clay particles is of interest as this governs whether it is classified as an arenite, wacke or mudstone (Figure 3.1). Clays also have important effects on diagenesis in terms of forming easily compressible grains, cements and pore clogging crystals (Ali et al., 2010).

Allogenic clay can be deposited in different ways depending on source and depositional environment which consequently form e.g. dispersed matrix, lamina, sand-sized floccules, sand- to cobble-sized mud or shale clasts (Figure 3.2). Bioturbation and subsequent infiltration are consequential secondary forms of clay deposition (Wilson & Pittman, 1977). Infiltrated particles are carried by downward or laterally migrating pore waters and naturally accumulate in pore spaces. The accumulation of clay particles can form tangential grain-coating and pore-bridging fabrics. Any type of clay can occur as a detrital component, however typically chlorite, illite, smectite and mixed-layer clays are observed as grain-coatings (Ali et al., 2010). Clays deposited as grain-coatings can become an important parameter during further diagenesis, as these can retard or inhibit quartz cementation.

By determining the constituent mineral composition of sandstones it is possible to infer provenance, palaeoclimate and tectonic stability during deposition. It is therefore a vital first step in understanding a reservoir, as these initial factors will further determine the effects of diagenetic processes (Bjørlykke & Jahren, 2015).

Figure 3.2: Different types of allogenic clay deposits found in sandstones *(modified after Wilson & Pittman, 1977 in Ali et al., 2010).*

Quartz

Quartz is stable at Earth's surface and is highly resistant to chemical weathering, effectively making it the commonest mineral found in sandstones. Over long transport distances, quartz grains become abraded and rounded but remain intact due to the lack of cleavage and high degree of hardness. These characteristi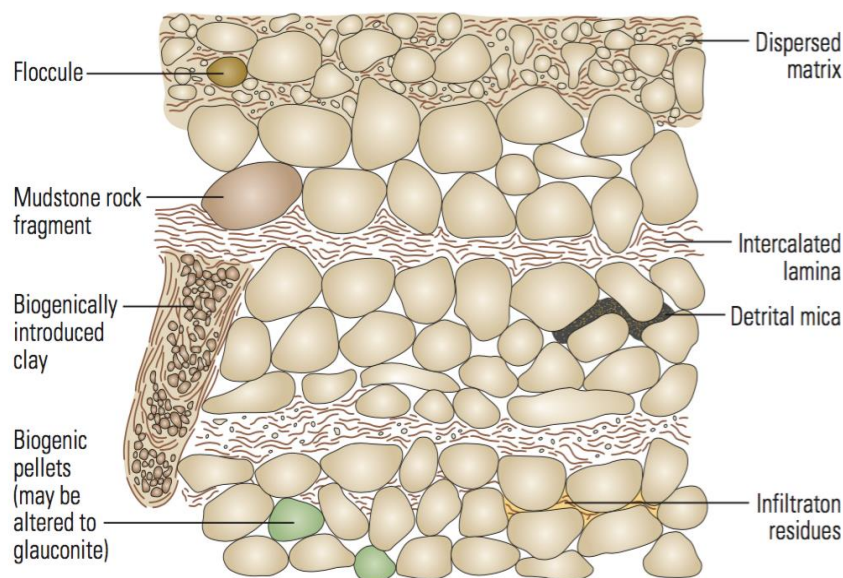c features make it an important mineral when determining maturity of the sandstone in question (Nichols, 2009). When analysed under the microscope, two subdivisions are made separating monocrystalline and polycrystalline grains. Monocrystalline grains are considered as a single quartz crystal whereas polycrystalline grains are composed of two or more crystals. The internal structure of polycrystalline grains can be helpful when attempting to distinguish igneous from metamorphic origin. Igneous and metamorphic rocks are brought to the surface by tectonic uplift during which they are commonly plastically deformed. The effect of deformation is seen in thin section as undulatory extinction, meaning that crystals do not extinguish as a single unit (Blatt, Tracy & Owens, 2006). Medium- to coarse-grained monocrystalline quartz grains are principally derived from granitoid plutonic rocks whereas finer monocrystalline grains have a variety of sources. The origin of these finer grains are listed by Blatt, Tracy & Owens (2006) as: (1) release from fine-grained metamorphic rocks such as slates, phyllites and fine-grained schists; (2) breakage and chipping of larger quartz grains of any provenance and (3) disaggregation of polycrystalline quartz grains during soil-forming processes. The reason behind this particular subdivision is that it can give some indication of maturity. Monocrystalline quartz grains are more durable in a sedimentary environment, and are thus indicative of a more mature sandstone (Blatt, 1992).

When 95% of a thin section is point counted as quartz the classification 'quartz arenite' is made. However, if intermediate percentages of feldspars or lithic fragments exist then the terms 'subarkosic arenite' or 'sublithic arenite' are implemented (Nichols, 2009).

Feldspars

Feldspars are also a good indicator of sandstone maturity, however are less durable in a sedimentary environment than quartz. Feldspars can be subdivided into three categories and are further listed by Blatt, Tracy & Owens, (2006) as:

- Potassic feldspars: orthoclase, microcline and sanidine
- Plagioclases: albite through anorthite
- Microperthite: an intergrowth of sodic feldspar and potassic feldspar

Feldspars are highly prone to surface weathering but are also altered subsequent to burial and thereby affected by early diagenesis. Consequently, feldspars are not reliable indicators of climate although when an abundance of unaltered feldspars are encountered inferences can be made that sufficient meteoric water has not been readily available to cause chemical alteration (Blatt, Tracy & Owens, 2006).

Feldspars are found in nearly all types of igneous and metamorphic rocks. Tectonic settings and climate have a large impact on the percentage and type of feldspars found in sandstones. When uplift, erosion and burial are rapid, a larger proportion of feldspars are preserved in sandstones. In contrast, when eroded material is exposed to long periods of high kinetic energy produced by e.g. waves and currents, most feldspar grains are removed by means of persistent abrasion (Blatt, Tracy & Owens, 2006).

The principal type of feldspar (k-feldspar or plagioclase) found in sandstone is also highly dependent on the tectonic setting in which the sandstone is formed. Plagioclases (albite through anorthite) are commonly more dominant around convergent plate margins where erosion and burial are rapid (Figure 3.3.B). Potassium feldspars (orthoclase and microcline) on the other hand are typically more abundant in rifted intracratonic settings (Blatt, Tracy & Owens, 2006) (Figure 3.3.A). If feldspars are exposed to significant meteoric water flushing during early diagenesis, mineral alteration takes place forming e.g. kaolinite (Bjørlykke & Jahren, 2015) leaving feldspars leached and difficult to identify during microscopic analysis (Figure 3.3.C). This process will be further discussed in section 3.3.1 (Early chemical reactions).
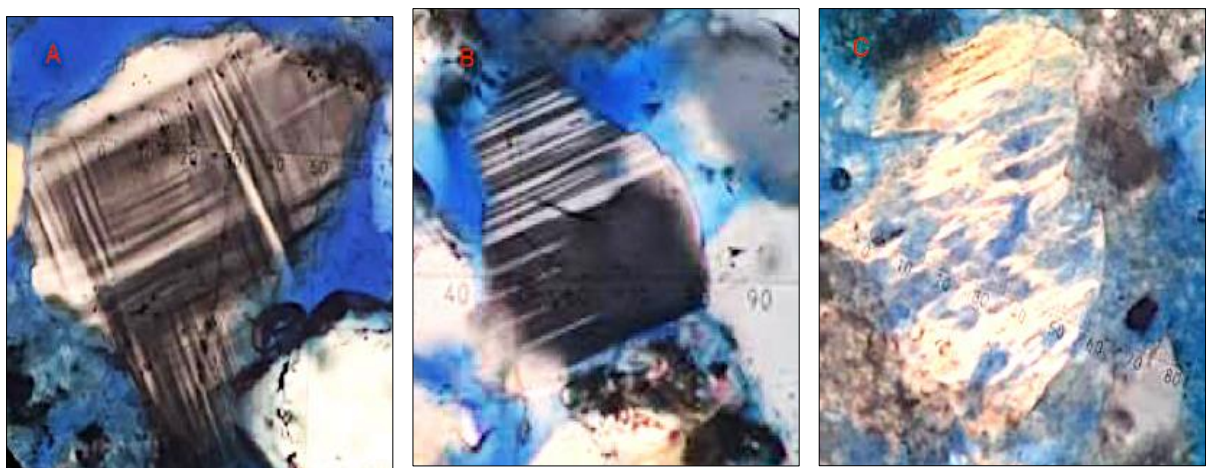

Figure 3.3: Photomicrographs of different types of feldspars found in well 7324/8-1. (A) Microcline showing grid twinning. (B) Plagioclase showing characteristic albite twinning (C) Altered feldspar showing partial grain dissolution *(Photo: Clark, 2017).*

Lithic fragments

Lithic fragments are pieces of polymineralic rock that are helpful indicators of whether the provenance rock was of igneous or metamorphic origin (Blatt, Tracy & Owens, 2006). The types of grains found in sandstones are dependent on a number of factors. Areal extent and relief of the provenance rock are two geographical features that will determine the abundance. When the areal extent of a rock is prominent there is a better chance of finding lithic fragments downstream. A high relief is equally important as this accentuates erosional rates. Chemical and mechanical durability in addition to crystal sizes in fragments will further determine the susceptibility to destruction (Blatt, Tracy & Owens, 2006).

Accessory minerals

Accessory minerals comprise all detrital minerals with the exceptions of quartz and feldspars. This in turn means that any mineral found in igneous or metamorphic rocks can be found in sandstones. The abundance is again dependent on specific factors such as, the prevalence of minerals, weathering rate and specific gravity. Specific gravity causes accessory minerals to become segregated during transport. Table 3.2 shows a few of the commonest accessory minerals and their source (Blatt, Tracy & Owens, 2006).

Detrital micas are typically found in fine-grained sandstones of metamorphic origin. This is mainly due to aluminium deficiency in granitoid rocks, i.e. most of the potassium is utilized to form potassium feldspars during crystallization (Blatt, Tracy & Owens, 2006).

Table 3.2: Source rocks of principle accessory minerals found in sandstones *(modified after Blatt, Tracy & Owens, 2006).*

Igneous Rocks	Metamorphic Rocks	Indeterminate
Augite	Andalusite	Hornblende
Chromite	Epidote	Magnetite
Ilmenite	Garnet	Tourmanline
Topaz	Kyanite	Zircon
	Rutile	

3.3 Diagenesis

Diagenesis is a dynamic compilation of processes, which take place post-deposition but prior to metamorphism (200-250°C) (Bjørlykke & Jahren, 2015; Worden & Burley, 2003). Diagenetic processes continually evolve and drive sediments towards a stable state (equilibrium). The controlling factors are temperature, pressure and chemistry, which are subsequently modified by burial and uplift of a basin (Worden & Burley, 2003).

Sediments are commonly deposited as heterolithic assemblages, containing minerals, dead organic matter and living organisms. Such contemporaneous mixtures are not in equilibrium and therefore not stable with their ambient surrounding. Through diagenetic processes the sediments within the system are exposed to oxygen and meteoric fluids (during early burial) in addition to effective stress and increased temperature (during deeper burial), all of which force the system towards equilibrium (Tissot & Welte, 1984; Bjørlykke & Jahren, 2015). To further understand the diagenetic processes, a three-fold sub-division between early chemical reactions, mechanical compaction and chemical compaction is distinguished and will be subsequently explained in the following sections.

3.3.1 Early chemical reactions

Chemical reactions are driven by thermodynamics whereby minerals strive to reach equilibrium. Early chemical reactions take place in an open system meaning that sediments are able to react with the atmosphere or water, resulting in the creation or removal of solid-state sediments (Bjørlykke & Jahren, 2015).

The general reaction that transpires during early burial is referred to as subsurface weathering (Bjørlykke, 1998):

Rock (feldspar, mica) + water = clay + cations.
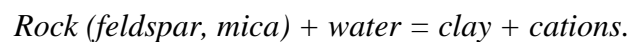
Feldspar and mica are examples of minerals that undergo alteration as a result of weathering and early diagenetic processes, forming hydrous clay minerals such as kaolinite (Bjørlykke, 1998). These reactions transpire either by meteoric fluid flushing or diffusion at very shallow burial depth.

Meteoric water is initially undersaturated with respect to all minerals and consequently not in equilibrium with its surroundings. As water infiltrates through the sediments, it is capable of dissolving unstable minerals such as carbonates, feldspar and mica (Bjørlykke & Jahren, 2015). The effect of meteoric water is principally governed by the water flux which is able to infiltrate deep into sedimentary basins assuming a high flux. The water flux is further dependent on climate, topography, water table, aquifers and aquitards, typically presenting a higher flux within marginal settings and shallow parts of a basin (Bjørlykke, 1998).

The principal weathering reaction occurring at shallow depth (low temperatures) due to meteoric flushing is the dissolution of feldspar and mica and precipitation of kaolinite (Eq. 1 and Eq. 2 respectively). Kaolinite is part of the kaolin-serpentine clay mineral series and tends to form stacked pseudohexagonal plates in a vermicular arrangement (Worden &

Morad, 2003). For reactions to proceed, low K^+/H^+ ratios are necessary in addition to residual products (Na^+, K^+ and silica) being removed from the system, or reactions will subsequently terminate (Bjørlykke & Jahren, 2015).

Equation 1.
$$2K(Na)AlSi_3O_8 + 2H^+ + 9H_2O = Al_2Si_2O_5(OH)_4 + 4H_4SiO_4 + 2K^+(2Na^+)$$
K-feldspar   *Water*   *Kaolinite*   *Silicic acid*   *Dissolved ions*

Equation 2.
$$2KAl_3Si_3O_{10}(OH)_2 + 2H^+ + 3H_2O = 3Al_2Si_2O_5(OH)_4 + 2K^+$$
Muscovite   *Water*   *Kaolinite*   *Dissolved K^+*
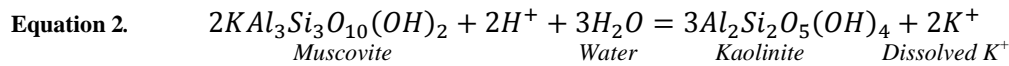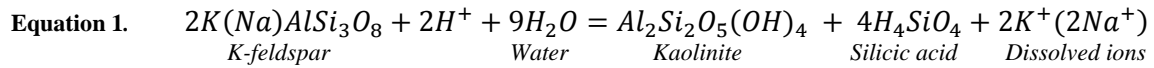
The rate at which these reactions occur is therefore dependent on the flux of undersaturated meteoric water (with regard to feldspar and mica) flowing into a system and furthermore removing the resultant products, keeping the water from reaching equilibrium with the mineral phases present (Bjørlykke, 1998). According to Bjørlykke (1998), the flux of water has to be significant (10^3-$10^4 m^3/m^2$) to dissolve adequate amounts of feldspar and mica in order to precipitate a small percentage of kaolinite. Therefore, the degree of feldspar and mica dissolution is a good indicator of the intensity of meteoric flushing. Figure 3.4 summarizes the main chemical reactions transpiring during early burial.

Low sedimentation rates may expose sediments to extensive leaching as sediments remain within reach of meteoric water for an extended period of time, whereas high sedimentation rates quickly bury sediments beyond the limits of meteoric flushing (Bjørlykke & Jahren, 2015).

With regard to reservoir quality, dissolution of minerals creates secondary pore spaces, but the subsequent precipitation of kaolinite and mechanical compaction of sediments results in little net gain of porosity. The observed consequences are minor increases in porosity but simultaneously reducing the permeability, causing oil-saturation in kaolinite-rich sandstones to decline (Bjørlykke & Jahren, 2015).

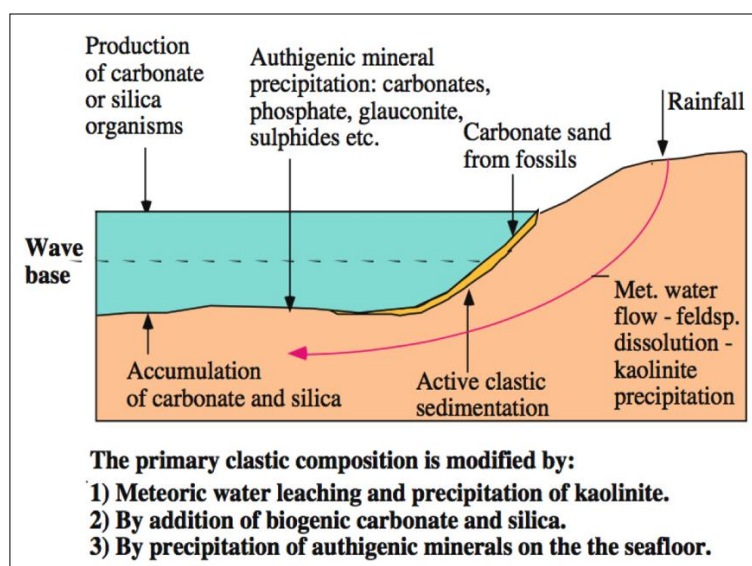Kinetics determines the rate at which reactions take place; e.g. kaolinite is able to

Figure 3.4: Diagenetic processes in shallow marine environments showing the effects of meteoric flushing *(after Bjørlykke & Jahren, 2015).*

precipitate at low temperatures, whereas quartz requires significantly higher temperatures to nucleate. Therefore, the silica ($4H_4SiO_4$) that is released from feldspar dissolution is not able to precipitate during early burial and has to be removed along with potassium in order for kaolinite to remain stable. If silica is not removed (e.g. stagnant pore water) and concentration levels become adequately high in pore water, smectite becomes the dominant product of feldspar and mica dissolution (Bjørlykke & Jahren, 2015).

Diffusion is limited to approximately one meter below the seabed, which entails that a majority of mineral altering reactions take place within shallow burial depths (Bjørlykke & Jahren, 2015). The redox-boundary represents an important feature within sediments as this defines the limit of free oxygen. Oxygen is supplied to the subsurface by diffusion but is quickly consumed by the oxidation (decay) of organic matter. This boundary is commonly found 1-20cm below the seafloor and characterises the transformation from oxidising to reducing conditions (Bjørlykke & Jahren, 2015). Oxidation of minerals such as iron and manganese are rare in marine environments as sufficient amounts of reducing organic matter are in place. Iron can however be transported to the surface in its reduced state and thereby precipitate on the seafloor as iron oxide due to its reduced solubility in the oxidised state. Iron can also precipitate as iron sulphides or iron carbonate (siderite) below the redox boundary. At sufficient depth, free oxygen becomes depleted and the dominating reactions are governed by sulphate-reducing bacteria which produces sulphides such as pyrite (Bjørlykke & Jahren, 2015).

Bioturbation can significantly impact the redox-boundary and furthermore change the textural composition of sediments following deposition. The consequences of bioturbation with regard to reservoir quality can be both beneficial and detrimental. Burrowing organisms destroy primary lamination, which effectively exposes sediments to further oxidation and reduces porosity and permeability by mixing clay and clean sand (Bjørlykke & Jahren, 2015). However, burrowing organisms can also be beneficial for reservoir quality through their activity. The faecal material that is produced by these organisms may consequently turn into smectite-rich clays and chlorite grain coatings, which can be of significance for preserving porosity during diagenesis (Bjørlykke & Jahren, 2015).

The composition of marine organisms is an additional implication that may further affect reservoir quality. Aragonite will dissolve at shallow burial depths and is the principle source for calcite cementation. Calcite cement is precipitated in pore spaces, reducing the permeability in both sandstones and mudstones (Bjørlykke & Jahren, 2015).

3.3.2 Mechanical compaction

Mechanical compaction is a result of increased burial and typically includes grain rearrangement, deformation of ductile components, dissolution and brittle fracturing (Worden & Burley, 2003). The main impact of mechanical compaction in terms of reservoir quality is porosity loss. Well-sorted, clean sandstones are empirically proven to have initial porosities ranging between 40-45% (Bjørlykke & Jahren, 2015; Blatt, 1992), whereas mud typically exhibits porosities as high as 60% (Blatt, 1992). Relatively low pressures quickly reduce the initial high porosity in mud. Clay minerals are characteristically ductile and can therefore be compacted tightly at low pressures causing interstital water to be squeezed out (Blatt, 1992). Sandstone compaction is further dependent on sorting, grain angularity and grain size. Porosity values will typically be reduced to 25 ± 5% in clean, well-sorted sandstone. Conversely, many sandstones contain substantial amounts of ductile grains and matrix which are able to bend around the more ridged quartz and feldspar grains to fill pore spaces in addition to reducing friction between rigid grains resulting in further compaction. In such cases porosity can be reduced from its initial 40-45% to almost zero. Compaction is consequently dependent on four factors: clay content, percentage of ductile grains, textural parameters (e.g. sorting), and burial depth (effective stress) (Blatt, 1992).

In order to calculate the effects of mechanical compaction it is important to know which mineral compositions are included in the lithological column (as these may vary horizontally and vertically) and which fluids fill the pore spaces (oil, water or gas). According to Bjørlykke, Høeg & Mondol (2015) the vertical stress (σ_v) exerted on a layer of sediment is produced by the overburden weight of sediments as well as the weight of pore fluids and can be written as:

$$\text{Equation 3.} \quad \sigma_v = \rho_v g h$$

where ρ_v is the average sediment bulk density (solids + fluids) of the overlying sequence, h is the sediment thickness and g is the acceleration of gravity.

The effective vertical stress (σ_v') further governs mechanical compaction of sediments and is described by Bjørlykke, Høeg & Mondol (2015) as the difference between the vertical total stress (σ_v) and the pore pressure (u):

$$\text{Equation 4.} \quad \sigma'_v = \sigma_v - u$$

The effective vertical stress is transmitted through grain contacts and opposed by fluid pressure (Figure 3.5). When calculating compaction, it is generally assumed that pressure (MPa) increases by 10MPa km^{-1} in normally pressured rocks. Overpressure opposes the
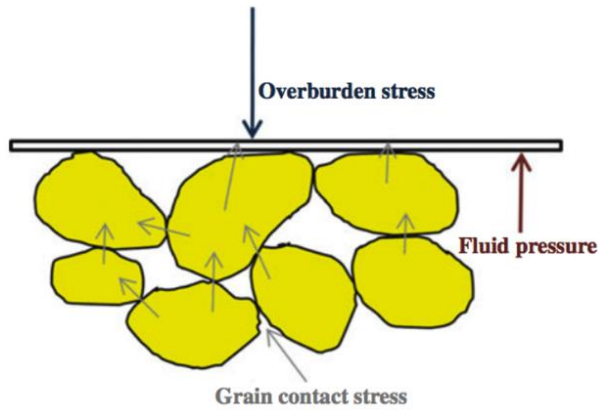
Figure 3.5: The effective vertical stress is determined by the difference between overburden stress and the opposing fluid pressure which is transmitted through grain contacts *(after Bjørlykke, Høeg & Mondol, 2015).*

effective stress and will thereby preserve porosity and inhibit further mechanical compaction (Bjørlykke & Jahren, 2015).

As sediments are buried to a depth of 2-3km, equivalent to 20-30MPa, porosity will be reduced to 35-25% (Bjørlykke & Jahren, 2015). Compaction is however as previously mentioned also dependent on textural parameters such as grain size, sorting and maturity. I.e. coarse-grained sands experience a higher stress per grain

contact as opposed to finer sands causing a higher degree of grain crushing (Figure 3.6). Comparably, immature sands generally have irregular surfaces and therefore a smaller contact area, again causing higher effective stress (Bjørlykke & Jahren, 2015). Sorting affects compaction by means of ability to reorganize and deform plastically. Sandstones consisting primarily of rigid grains (e.g. quartz and feldspar) are less able to reorganize, leading to a close packed geometry and a theoretical porosity value of approximately 26% subsequent to mechanical compaction (Worden & Burley, 2003).
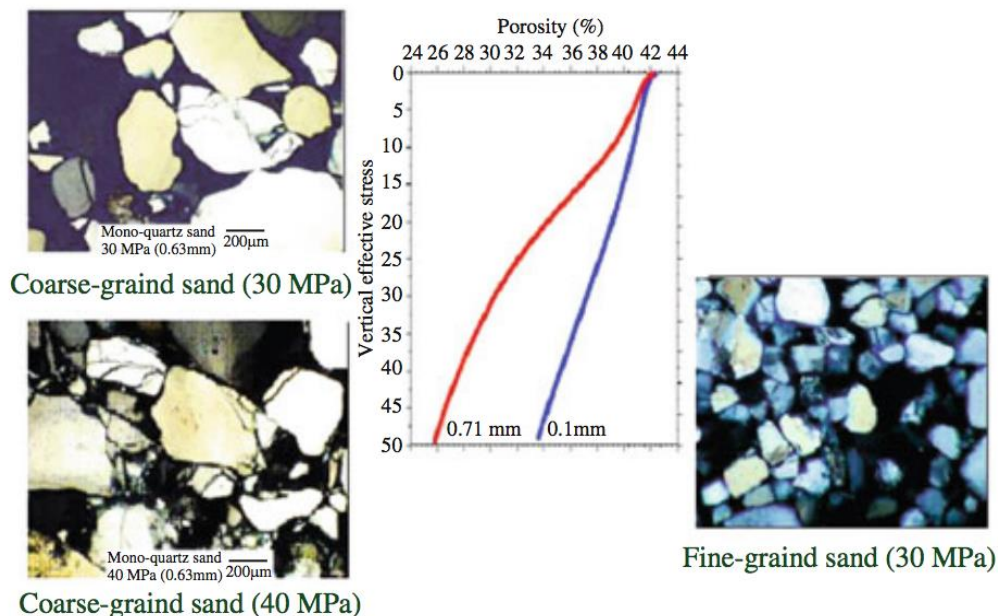
Figure 3.6: Empirically determined curves showing that coarse-grained sand compacts more readily than well-sorted, fine-grained sand *(after Bjørlykke & Jahren, 2015).*

In heterolithic sandstones, containing an abundance of ductile grains or matrix, porosity loss is more severe and can lead to negligible porosities. This is caused by plastic deformation, meaning that ductile grains become extruded between more rigid grains (Worden & Burley, 2003) (Figure 3.7).

The intergranular volume (IGV) of sediments is determined by the proximity of framework grains and is governed by mechanical and chemical compaction. Intergranular volume is defined by Paxton et al. (2002) as: "The sum of intergranular pore space, intergranular cement, and depositional matrix (depositional silt- and clay-size particles that fill the space between framework grains)". A study conducted by Houseknecht (1987) further analyzes the effects of compactional processes

Figure 3.7: Three-fold schematic cartoon of compaction processes. (a) depositional fabric showing typically high porosity, (b) mechanical compaction depicting grain repacking and fracturing, (c) repercussions subsequent to mechanical and chemical compaction *(after Worden & Burley, 2003).*

and cementation with regard to original depositional porosity and estimated intergranular volume. Intergranular volume is affected by three separate diagenetic parameters: mechanical compaction, chemical compaction and cementation. Mechanical compaction is produced by lithostatic stress and typically results in the reduction of bulk volume by reorientation and repacking of competent grains. Chemical reactions are driven by thermodynamics and thereby cause mineral alteration, resulting in a reduction of intergranular volume. Mineral dissolution of framework grains is induced at points of contact, which causes a closer packing of framework grains. Cementation reduces intergranular porosity by precipitation of authigenic minerals such as calcite (Houseknecht, 1987).

Once burial reaches a depth of approximately 2km corresponding to temperature ranges between 70-80°C (within a normal geothermal gradient), chemical compaction successively takes over and reduces porosity further (Bjørlykke & Jahren, 2015; Worden & Burley, 2003). In summary, mechanical compaction is a combined function of burial depth, lithology and fluid pressure (Figure 3.9).

3.3.3 Chemical compaction

Intermediate burial (2,0-3,5 km; 50-120°C)

Increasing burial depth equates to an increase in ambient temperature, which results in further changes in mineral stability (Worden & Burley, 2003). Quartz cementation is initiated at roughly 70°C and increases exponentially with temperature (Figure 3.8), marking an important boundary between the cessation of mechanical compaction and beginning of chemical compaction. Two to four percent quartz cement is sufficient to stabilize grain framework and effectively shut down mechanical compaction (Bjørlykke & Jahren, 2015).

Pressure dissolution transpires as a consequence of both temperature and pressure and increases the surface area of grain-grain contacts, effectively distributing the load over a greater area. Grain contacts thereby evolve from point contacts through straight-elongate to concave-convex and ultimately become sutured (Worden & Burley, 2003). Quartz dissolution is enhanced if mica or clay minerals are situated between grains contacts. The presence of thin clay-rich laminae between framework grains can produce stylolites and form as a consequence of pressure dissolution. The dissolved silica is transported away from grain contacts or stylolites by diffusion to grain surfaces where quartz cement is able to nucleate (Bjørlykke & Jahren, 2015).
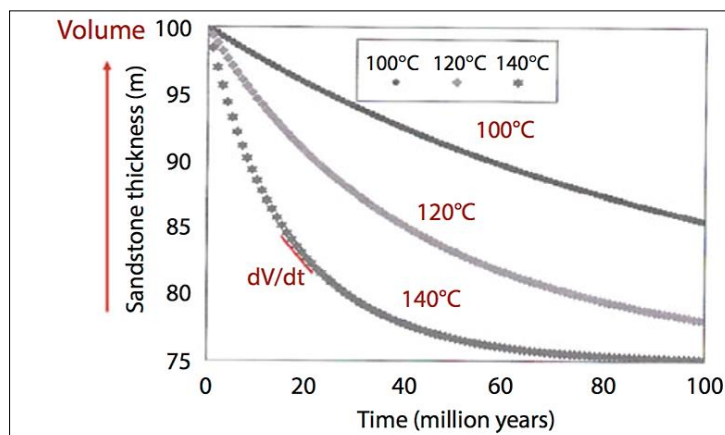
Figure 3.8: Quartz cementation and chemical compaction as a function of time and temperature *(after Walderhaug et al., 2001 in Bjørlykke, 2015).* **The rate of quartz cementation decreases successively due to diminishing surface area available for quartz nucleation.**

Quartz cementation is not simply a function of temperature but also depends on the grain surfaces available for quartz precipitation. Pore lining elements can form by clay coatings or substances such as petroleum or bitumin on the surface of framework grains (Wilson & Pittman, 1977; Bjørlykke & Jahren, 2015).

Clay linings commonly constitute chlorite which is derived from precursory deposits such as smectite-rich clays. An important consequence of pore linings is the inhibition of quartz nucleation, which in turn can preserve porosity during burial (Bjørlykke & Jahren, 2015). Due to the possible constraint of quartz cementation, mechanical compaction may proceed down to 4-5km burial depth causing extensive grain crushing (Chuhan et al., 2002). The fractured grains in turn generate fresh surfaces whereby quartz nucleation is able to commence (Bjørlykke & Jahren, 2015).

The distinction between quartz grains interlocked by pressure solution and quartz grains welded together by cementation can be difficult when using a microscope. A more accurate distinction can be made using cathodoluminescence petrography. This method is based on the formation temperature of quartz and the response to electron bombardment. Detrital grains (formed at temperatures exceeding 300°C) will luminesce whereas secondary quartz cement (formed at temperatures below 150°C) will not (Blatt, 1992).

Authigenic illite can form at the expense of smectite or kaolinite and has detrimental effects on the permeability of a reservoir. In order for kaolinite to react to form illite, a source of potassium is required (K-feld) (Eq. 6), however low kinetic precipitation rates are observed below 120°C. Smectite also requires a source of potassium and becomes thermodynamically unstable at 70-100°C, successively forming illite via mixed-layered minerals (Eq. 5). Illite generally tends to occur as flakes, filaments or hair-like crystals (Bjørlykke, 1998).

Equation 5.   *Smectite + K+ = Illite + Silica (via mixed-layer minerals)*

Equation 6. $KAlSi_3O_8 + Al_2Si_2O_5(OH)_4 = KAl_3Si_3O_{10}(OH)_2 + 2SiO_2 + H_2O)$
K-feldspar   Kaolinite   Illite   Silica   Water
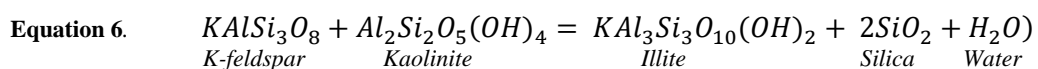
If however k-feldspars are not readily available, the necessary potassium for illitisation is not obtainable and reactions will not proceed. Once temperatures exceed 90°C kaolinite is generally no longer stable and starts to recrystallize into dickite. Kaolinite and dickite are two polymorphs within the kaolin group (Vangdal et al., 2014). Dickite has the same chemical composition as kaolinite but appears as slightly thicker rhombic crystals (Bjørlykke & Jahren, 2015; Worden & Morad, 2003). Studies have been conducted by Vangdal et al. (2014) in order to determine whether the transformation of kaolinite to dickite can be used as a geothermometer. Analysed samples cover large parts of the Norwegian Continental Shelf and show that two threshold temperatures can be presumed. The first threshold temperature found is at 90°C in which both kaolinite and dickite were observed in

samples, representing initial transformation. The second threshold temperature found is at 100°C, representing the lowest temperature at which solely dickite was observed. These temperatures can therefore be used as rough guidelines as to what minimum temperature sediments have been exposed to.

An additional effect of intermediate burial (3km) is the albitisation of feldspars. This process encompasses the replacement of K-feldspar or plagioclase by albite, which becomes the more stable mineral at ambient pressure and temperature. Albitisation has no immediate effect on reservoir quality but is a noteworthy chemical consequence caused by intermediate burial (Bjørlykke & Jahren, 2015).

Deep burial (>3.5-4km; >120°C)

As long as the ambient temperature remains above approximately 70°C, quartz cementation will proceed given available surface area until nearly all porosity is lost. This process will continue whether sediments are progressively being buried or subsequently uplifted (Bjørlykke & Jahren, 2015) (Figure 3.9). In order to predict reservoir quality, it is vital to understand the initial sediment composition (textural and mineralogical) as well as the dynamics of diagenesis. Figure 3.9 summarises the main diagenetic processes transpiring through various burial depths and subsequent uplift (Bjørlykke & Jahren, 2015).

Typically, well-sorted, clean sandstones (without clay coatings) will preserve porosity to about 3.5-4km but subsequently be exposed to rapid quartz cementation. In contrast, a sandstone with moderate amounts of clay content or pore lining clays will be highly subjected to porosity loss during mechanical compaction, but may preserve porosity at greater depth due to inhibited quartz cementation (Bjørlykke & Jahren, 2015).
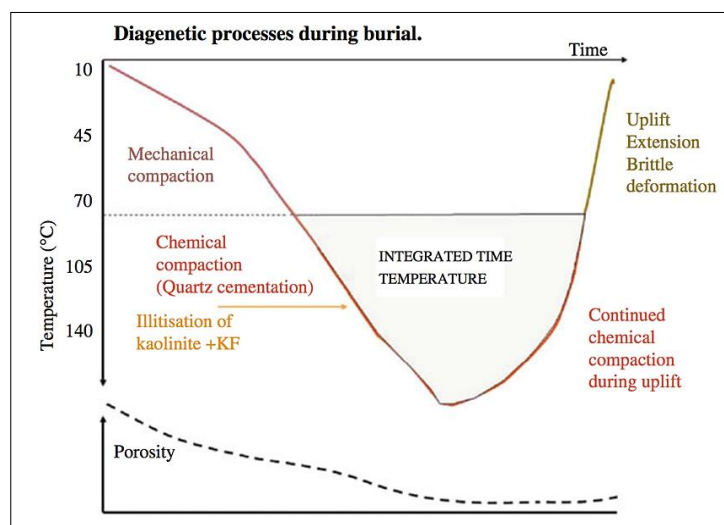
Figure 3.9: Summary of the diagenetic processes transpiring as a function of time and temperature *(after Bjørlykke & Jahren, 2015).*

4. Methods and Data

4.1 Introduction

The aim of this thesis is to identify the reservoir potential in Fruholmen and Stø Formations in two separate wells located within the Hoop Fault area. The methods used to conduct such analyses are based on petrographic and petrophysical data, provided largely by OMV Norge AS.

4.1.1 Data

Hanssen (7324/7-2) concluded a core log totalling 72m and Wisting Central (7324/8-1) slightly shorter at 48m. Twenty samples from each core respectively were further selected in order to aid further work. The interval of samples was obtained by visual assessment with the assistance of Lina Hedvig Line (UiO, PhD). These samples are chosen with emphasis on reservoir sandstones within Fruholmen and Stø Formations.

Wisting Central (7324/8-1) was the northernmost hydrocarbon-bearing discovery made in 2013. The well is located approximately 310km north of Hammerfest (Fig. 5.1) and was the first of several exploration wells to be drilled in this area. According to NPD Fact Pages (2016), the well was drilled to a vertical depth of 930mD [m RKB] with a water depth approximating 398m. Drilling was conducted with the main purpose of proving the presence of hydrocarbons in Middle to Lower Jurassic reservoir rocks of the Upper Realgrunnen Subgroup. Results attested these prospects showing a 50-60m oil column, generating further interest in the reservoir potential of the Hoop High area (OMV Norge AS, 2014).

Hanssen (7324/7-2) is located 7km northwest of Wisting Central (7324/8-1) and was discovered in 2014. Drilling terminated in the Snadd Formation (Middle Triassic) at a vertical depth of 1,730mD [m RKB] and water depth of 417.5m (NPD, 2016). The objective of drilling was once more to prove the incidence of hydrocarbons in the Late Triassic to Middle Jurassic Formations (Fruholmen, Nordmela and Stø) with subsidiary interests in Middle to Late Triassic rocks (Snadd Formation). An oil column totalling 20-25m was confirmed in the Stø Formation (OMV Norge AS, 2014).

4.1.2 Methods

Initial logging procedures and core sampling were conducted at Weatherford Laboratories AS, Stavanger with the assistance of Lina Hedvig Line (PhD, UIO) and Jens Jahren (Professor, UIO) during the Autumn of 2016. For optimal quantitative and qualitative purposes, logging was conducted at a scale of 1:50 and later digitalized and condensed using

Adobe Illustrator. Sedimentological logs alongside core photos were used when interpreting and describing facies and depositional environments. Grain size was determined using Wentworth (1922) grain size classification chart.

Core samples were marked throughout and subsequently extracted by technicians at Weatherfords Laboratories AS. The forty samples provided by OMV Norge AS were consequently used to explore the reservoir potential by conducting X-ray diffraction (XRD) analysis, optical microscopy analysis, scanning electron microscopy (SEM) and cathodoluminescence (CL). These laboratory techniques provide a quantitative mineralogical and textural description.

4.2 Petrographic Analyses

Laboratory work has been carried out at the University of Oslo under the guidance and help of PhD students Beyene Girma Haile and Lina Hedvig Line.

Petrographic analyses are based on determining qualitative and quantitative mineralogical data of samples. Bulk X-ray diffraction analysis is a primary method in which to identify and quantify the mineral compilation of each sample. Optical microscopy is used to further identify e.g. grain framework, matrix, porosity and degree of weathering in each selected sample. Ultimately, scanning electron microscopy and cathodoluminescence produces high-resolution precision of previously mentioned factors and were conducted under the supervision of Berit Løken Berg (UIO).

4.2.1 X-ray Diffraction (XRD)

X-ray diffraction (XRD) analysis is a primary method in which to identify and quantify the mineral compilation of each prepared sample. The unique inter-atomic spacing of individual crystalline minerals produces a characteristic X-ray diffraction pattern, which can further be matched against a vast database (Flohr, 2000).

Table 4.1: Selection of common minerals found in sandstones along with characteristic d-spacings (values are noted in Ångström).

Mineral	d-spacing (Å)	Mineral	d-spacing (Å)
Quartz	4.26	Calcite	3.03
Plagioclase	3.19	Kaolinite	7.0 / 3.58
K-feldspar	3.24	Illite	10.0
Muscovite	10.01	Chlorite	7.0 / 3.54
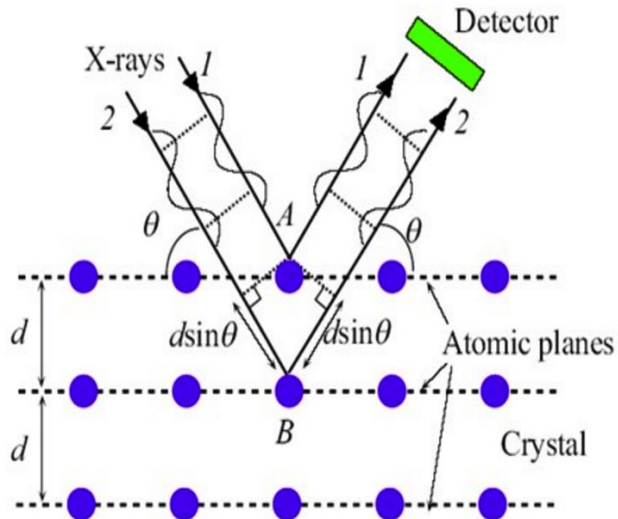
Figure 4.1: Depicts a schematic illustration of how XRD analysis is conducted and resulting peaks are produced *(after Klein & Philpotts, 2013).*

The diffraction pattern generated by the X-ray beam measures the distances between the planes of the atoms and is expressed by Bragg's Law:

Equation 7. $\quad n\lambda = 2dsin\theta$

which, according to Klein and Philpotts (2013): "Relates the interplaner (atomic) spacing (*d*) inside a crystalline material to a diffraction angle (θ) as a function of the wavelength (λ) of the X-rays used; n is an integer such as 1, 2, or 3. The letter d is a symbolic representation of all possible distances between differently oriented crystallographic (planer) directions inside a crystalline substance" (Figure 4.1).

The diffractogram obtained from the XRD scan represents a unique 'fingerprint' of the mineral or minerals that are present in each sample. The 'fingerprint' is then interpreted and identified using standard reference patterns (Flohr, 2000). Profex software is used to facilitate identification and quantify the abundance of individual mineral phases.

Sample preparation

A grain size of approximately 2μm is required for bulk X-ray diffraction analysis to be conducted. To obtain this grain size from the consolidated samples, two consecutive steps are essential. The initial procedure is mortaring the rock sample into a fine powder whereby further micronization (using a McCrone micronizer) is carried out to ensure a grain size of 2μm. Micronization is conducted using 3g of sample material and 9ml of ethanol. This is placed in a sealed container along with 48 pieces of agate and liquidized for 12min. The liquidized material is subsequently dried in an oven (≈50°C) overnight. The final step is to place the dried material into a sample holder ensuring a flat upper surface. For a more detailed step-by-step procedure guide see Dutrow & Clark (2016).

The sample holder is subsequently placed into the XRD-apparatus, which is pre-programmed to desired parameters. The pre-programming comprises the starting angle of incident light and the duration of analysis. The longer the duration of analysis, the more accurate the results become.

Limitations

Most laboratory testing endures some margin of human error. When conducting XRD-analysis a potential source of error can be encountered during sample preparation. When placing the micronized and dried material onto sample holders, it is vital that the material isn't smeared or compacted to the point by which a preferred orientation of grains is attained. When a preferred orientation is encountered, diffractogram readings become misleading and quantitative accuracy of mineral composition is reduced.

Additional limitations that can arise when conducting XRD-analysis are related to pre-programming of the apparatus (e.g. misalignment) and software limitations.

4.2.2 Scanning Electron Microscopy (SEM) and Cathodoluminescence (CL)

The scanning electron microscope (SEM) is a high-resolution instrument that is capable of identifying fine-grained sediments such as pore-filling clays. The technical definition by which the SEM is able to collect such high-resolution data is provided by Swapp (2017): "The scanning electron microscope (SEM) uses a focused beam of high-energy electrons to generate a variety of signals at the surface of solid specimens". The retrieved signals are able to provide a wide range of information such as: external morphology (texture), chemical composition and crystalline structure.

Cathodoluminescence (CL) is used to differentiate between detrital quartz grains and quartz cement. CL is defined by Henry (2016) as: "The emission of photons of characteristic wavelengths from a material that is under high-energy bombardment".

Analyses were carried out at the University of Oslo using a JEOL JSM-6460LV scanning electron microscope with a LINK INCA Energy 300 (EDS). Backscatter electron imaging (BEI) in addition to secondary electron imaging (SEI) are used to provide sample data.

Sample preparation

SEM allows for two possible methods of data viewing which subsequently require different sample preparation. Samples can be viewed using thin sections, providing a 2D image of the analysed sample, or samples can be analysed utilizing core stubs enabling a 3D image. Samples have to be coated in a conductive coating in order to reduce excess charge from the electron beam. When analysing thin-sections the coating of choice is carbon, which is preferentially used when elemental analyses are conducted. When conducting high-resolution electron imaging, as is the case when core stubs are utilized, gold is the preferable coating (Swapp, 2017).

4.2.3 Optical Microscopy

Thirty-eight thin-sections were prepared for optical microscopic analyses, however only 30 of these could be point counted. These were observed using a *Nikon Optiphot-Pol* petrographic microscope equipped with a Swift point counter and mounted camera. The remaining 8 samples contained significant amounts of clay-sized particles restricting the ability to differentiate between individual minerals.

All studied samples were analysed under plane polarized light (PPL) as well as cross-polarized light (XPL). These two features facilitate the identification of minerals by enhancing optical properties such as relief, colour, opacity, pleochroism, angle of extinction and twinning of crystals (Nichols, 2009).

Sample preparation

Samples were prepared at the University of Oslo by Salahalladin Akhavan of the pro-technical department. The two excluded samples are mud dominated and would not be sufficient for thin section analysis.

Thin sections are 30μm cuts of rock that are mounted onto 2.5 x 4.5cm glass slides. Prior to mounting, the rock samples are impregnated with blue epoxy to increase visual assessment of features such as porosity that would otherwise be difficult to observe.

Oil saturated sandstone necessitate washing preceding further preparation. This is carried out by solvent separation using Dichloromethane (DCM+MeOH) with a volume ratio of 93:7. The sample is left to soak for approximately 24 hours whereby most of the attainable oil is removed from the sandstone (Figure 4.2).

Figure 4.2: Oil saturated samples soaking in solvent *(Photo: University of Oslo, 2017).*

Point count analysis

Mineralogical features studied through optical microscopy are e.g. detrital grains, cement, matrix and porosity. These are statistically counted using a mounted point counter. Four hundred point counts are conducted per sample, which is considered representative for the entire thin section in question. Visual assessment is made when identifying minerals and

can many times be compared with textbook examples, e.g. 'Atlas of Sedimentary Rocks', (Adams et al., 1984).

When conducting a point-count it is imperative that systematic and consistent measures are established from the start and maintained throughout all samples. The point counter allows 12 categories to be distinguished; however these were manually subdivided and can be found in Table 10.4 and Table 10.5. Subdivisions are duly noted in order to gain further statistical data enabling more accurate interpretations. The main subdivided units are quartz (mono- versus polycrystalline quartz) and feldspars (k-feldspar, plagioclase and altered/unidentifiable feldspars).

The results of each point counted sample are subsequently plotted in a ternary diagram, distinguishing between the percentage of quartz, feldspar and rock fragments. The nomenclature used in this thesis is based on the Pettijohn et al. (1987) classification scheme.

Limitations

Mineral identification is highly dependent on the level of expertise and experience of the interpreter. As the degree of alteration increases, the ability to identify specific minerals, clay and matrix becomes progressively more difficult.

Additional limitations are due to technical sources of error such as thickness of thin sections, scratched glass surfaces and artificial porosity. Artificial porosity is encountered during sample preparation and occurs if the samples are not adequately glued onto the slides. Minerals may become stripped leaving a vacancy, which is in turn interpreted as pore space. The samples that were treated with solvent are potential candidates for showing artificial porosity. If oil remained within the samples, it may inhibit the effects of the glue and thereby cause an overestimated porosity count.

4.2.4 Textural Properties

Textural properties observed and measured in each point counted sample are listed as follows; grain size, sorting, shape, grain contacts, grain preservation, porosity and intergranular volume (IGV).

Intergranular volume

Intergranular volume is measured by point counting samples and implementing accumulated data (expressed as a percentage of each thin-section) into the following equation defined by Paxton et al. (2002):

$$\text{Equation 8.} \quad IGV = Pore\ space + Cement + Depositional\ matrix$$

When interpreting the degree of porosity loss induced by compactional processes and cementation, two separate equations can be utilized (Eq. 9 & 10) and represented in a diagram designed by Houseknecht (1987) (Figure 4.3). It is empirically documented that most moderate- to well-sorted sands contain approximately 40% porosity at the depositional surface and is therefore used as a starting point for subsequent calculations. The vertical axis represents the percentage lost due to compaction and is estimated using Equation 9. The horizontal axis represents the percentage of porosity lost due to cementation and is calculated using Equation 10. It is further assumed that porosity loss is independent of grain size but will vary according to grain sorting (Houseknecht, 1987) whereby grain-supported samples are further utilized. However, grain-supported, moderate- to moderately-well sorted samples containing variable amounts of matrix (silt- to clay-sized particles) are point counted. Discrepancies are noted between intergranular volume definitions by Houseknecht (1987) and Paxton et al. (2002). Houseknecht (1987) does not include depositional matrix in intergranular volume estimations whereby the diagram used herein will lead to intergranular porosities being overstated.

Matrix is substantially important when estimating porosity loss due to mechanical compaction. Fine-grained particles (matrix) aid mechanical compaction in terms of reducing friction between framework grains in addition to deforming in a ductile manner, subsequently filling available pore space. Therefore, depositional matrix will be included in intergranular volume estimations which further require its removal from final intergranular porosity calculations.

Following equations are provided by Houseknecht (1987) and slightly modified (shown in red) to comply with this study in order to represent the porosity loss due to compactional processes and cementation.

Percentage of original porosity destroyed by compaction:

$$\textbf{Equation 9.} \ = \frac{40 - (V_{cement} + V_{porosity} + V_{matrix})}{40} \ x \ 100$$

Percentage of original porosity destroyed by cementation:

$$\textbf{Equation 10.} \ = \frac{cement}{40} \ x \ 100$$

A third equation representing intergranular porosity is further noted but can also be estimated directly from the figure (Houseknecht, 1987):

$$\textbf{Equation 11.} \ \ Intergranular \ porosity = intergranular \ volume - cement$$

As previously stated depositional matrix will be included in initial intergranular volume equations and subsequently deducted from intergranular porosity estimations according to Paxton et al. (2002):

Equation 12. $Intergranular\ porosity = intergranular\ volume - (cement + depositional\ matrix)$

The serrated line in Figure 4.3 separates which pore reducing process has been predominant. If samples place in the upper right area, cementation has been the dominant process whereas if samples place in the lower left area, compactional processes are the predominant cause of porosity loss (Houseknecht, 1987). This diagram will be used accordingly in addition to further intergranular porosity calculations
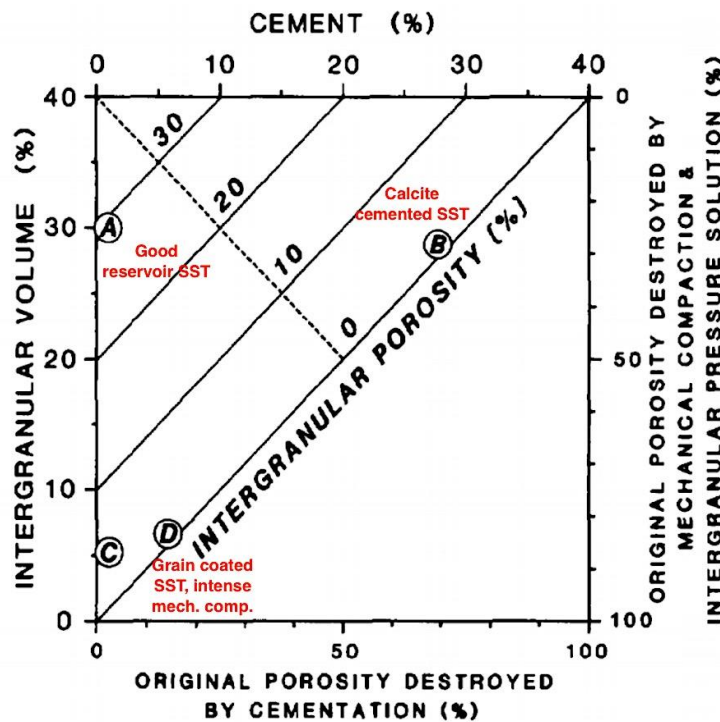
Figure 4.3: Diagram illustrating porosity loss as a function of mechanical and chemical compaction. A, B, C and D are examples of end-member sandstones *(modified after Houseknecht, 1987)..*

Grain size

In order to determine the average grain size of each sample, 100 randomly selected grains are measured and compared. These measurements are attained using an optical microscope, camera and supplementary photographic software. Measurements are carried out along the longest axis of each selected grain, exported to excel and converted to a Phi-scale (Eq. 13) in accordance with Wentworth grain size classification (Figure 4.4). The

equation used to convert the measured grains from millimetres to Phi is logarithmic to the base of two. The phi scale is calculated using the following equation:

$$\text{Equation 13.} \quad \phi = -log_2 d$$

Phi (Φ) is the desired measurement used in Wentworth classification scheme where d is the measured value in millimetres. The negative symbol is used due to most grains being less than 1mm in size, resulting in positive Φ-*values.*

Millimeters (mm)	Micrometers (μm)	Phi (φ)	Wentworth size class	
4096		-12.0	Boulder	Gravel
256		-8.0		Gravel
64		-6.0	Cobble	Gravel
4		-2.0	Pebble	Gravel
			Granule	Gravel
2.00		-1.0		
1.00		0.0	Very coarse sand	Sand
1/2 0.50	500	1.0	Coarse sand	Sand
1/4 0.25	250	2.0	Medium sand	Sand
1/8 0.125	125	3.0	Fine sand	Sand
1/16 0.0625	63	4.0	Very fine sand	Sand
1/32 0.031	31	5.0	Coarse silt	Silt
1/64 0.0156	15.6	6.0	Medium silt	Silt
1/128 0.0078	7.8	7.0	Fine silt	Silt
1/256 0.0039	3.9	8.0	Very fine silt	Silt
0.00006	0.06	14.0	Clay	Mud

Figure 4.4: Grain size classification scheme according to Wentworth (1922).

Grain sorting

The standard deviation of all measured grains can further be calculated (Eq. 14) and represented in a cumulative curve or used in conjunction with classification systems (Table 4.2). A cumulative curve indicates the percentage of various grain sizes in addition to sorting. A steep curve (indicating that most grains fall into one class of the Wentworth scale) represents good sorting, subsequently resulting in a less steep curve being interpreted as poorly sorted (Nichols, 2009). Visual comparators (Figure 4.5) are provided by Compton (1962) in order to aid interpretations.

Different types of depositional modes and transport distances will highly effect grain sorting. For example, fluvial transported sediments can be carried as either bedload or in suspension where grain size will be dependent on the energy of the river. Typically, fluvial sequences will be represented by a positively skewed cumulative curve (Bjørlykke, 2015).

A negatively skewed curve on the other hand is typical of beach sand deposits. Wave energy washes grains of varying sizes onto the beach whereby coarser grains (typically medium to coarse sand) settle onto the beach while finer sediments such as fine sand, silt and clay are carried back out to sea. These sediments tend to settle at depths where wave energy is decreased. Subsequent perturbation due to storms can disturb and mix fine-grained sediments with coarser material, thus giving a negatively skewed cumulative curve (Bjørlykke, 2015).

$$\text{Equation 14.} \quad Standard\ Deviation = \frac{\Phi_{84} - \Phi_{16}}{4} + \frac{\Phi_{95} - \Phi_5}{6.6}$$

Table 4.2: Sorting classification scheme corresponding to standard deviation measurements *(Folk, 1974).)*

STANDARD DEVIATION (FOLK, 1974)	Φ-VALUE
Very well sorted	< 0.35
Well sorted	0.35 – 0.50
Moderately well sorted	0.50 – 0.71
Moderately sorted	0.71 – 1.00
Poorly sorted	1.00 – 2.00
Very poorly sorted	2.00 – 4.00
Extremely poorly sorted	> 4.00
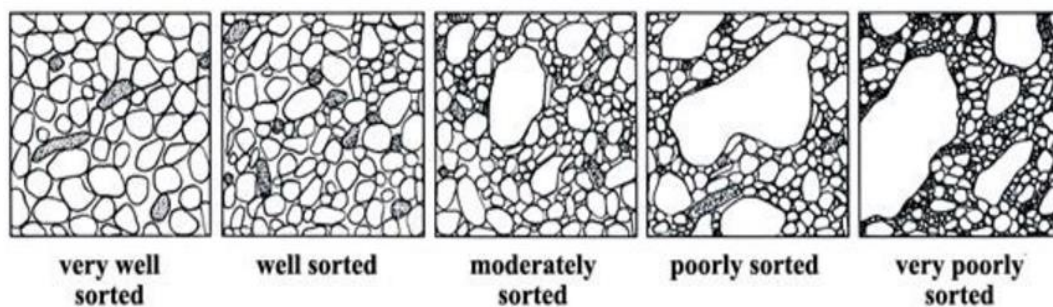
Figure 4.5: Visual comparators illustrating grain sorting *(after Compton, 1962).*

Limitations

These curves have to be used in conjunction with other means of interpretation as grain size can change during diagenetic processes causing a misinterpretation of depositional environments. Feldspars and mica grains may alter into clay minerals such as kaolinite, which would skew the curve towards a higher fine-grained sediment composition and would not be representative of depositional conditions (Bjørlykke, 2015). Grains may also be

crushed during mechanical compaction, once again skewing the cumulative curve towards a higher fraction of fine-grained sediment composition.

Grain shape

Grain shape is determined by the fracture properties of the host rock and the mode of transport it endures (Nichols, 2009). These parameters are assessed using Powers (1953) as visual guidelines (Figure 4.6). Grain shapes can be subdivided into several categories depending on method of interpretation. In this thesis two subdivisions are used for further analysis:

1. Roundness: a measure of how smooth or angular the surface of an individual mineral grain is.

2. Sphericity: an interpretation of how much a grain deviates from a sphere
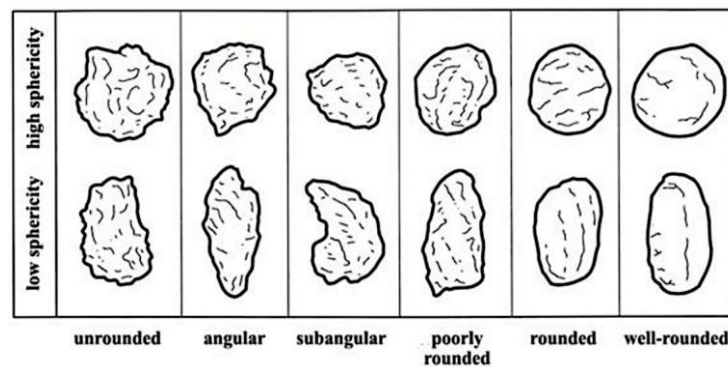
Figure 4.6: Visual comparators used when interpreting sphericity and roundness of grains *(after Powers, 1953).*

Grain contacts

As sediments are exposed to mechanical compaction, reorientation and repacking of grains will reduce the bulk volume and thereby decrease the intergranular volume. Subsequently, compaction assumes by pressure dissolution, effectively redistributing the accumulating load over a greater area. Grain contacts thereby evolve from point contacts through straight-elongate to concave-convex and ultimately become sutured (Worden & Burley, 2003). Figure 4.7 illustrates grain contacts commonly encountered when observed through thin-sections (Santin et al., 2009).
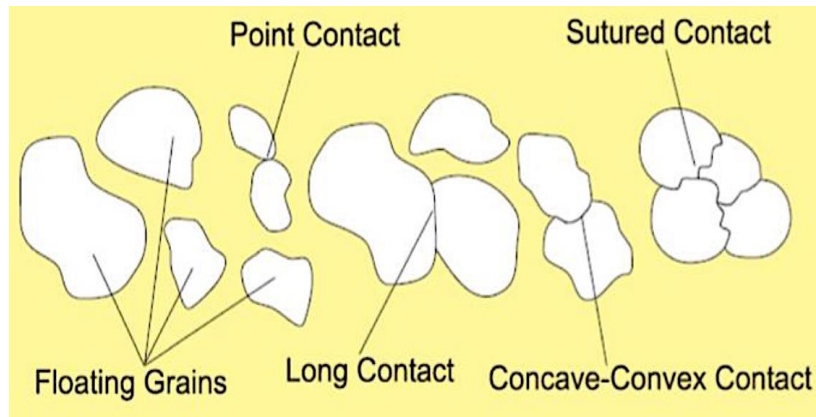
Figure 4.7: Visual guide used when assessing grain contacts in thin-sections *(after Santin et al., 2009)*.

4.3 Petrophysical Analyses

Petrophysical analyses are conducted in order to estimate sediments burial depth and subsequent uplift. This is conducted using well log data from both studied wells and is furthermore compared to previously published data by Baig et al. (2016). Well-log data utilized in this thesis are gamma-, sonic-, bulk density- and neutron logs.

During burial sediments undergo a number of changes caused by mechanical compaction and chemical reactions. Mechanical compaction, induced by increasing effective stress will reduce bulk volume by means of porosity loss, consequentially leading to higher rock density. Chemical compaction on the other hand is instigated by increasing temperature and triggers mineralogical changes, driving mineral assemblages towards higher thermodynamic stability (Bjørlykke & Jahren, 2015). Quartz cementation is initiated at approximately 70°C and typically represents the transition from mechanical compaction to chemical compaction. This transitional zone can commonly be seen in well-log data due to a sharp increase in P-wave velocity.

4.3.1 Gamma Ray Log

Gamma ray logs are typically used to differentiate between lithologies such as shale and sandstone/carbonate. A gamma ray log measures the total natural gamma radiation that emanates from a rock. The gamma rays are emitted spontaneously by elements such as potassium, thorium and uranium, where potassium is the most abundant. Shales will produce the highest gamma ray readings due to high potassium content while clean sandstones show the lowest readings.

43

The difference in gamma ray values therefore signifies a clear distinction between these two lithologies. Sandstones containing a large percentage of feldspar or mica will increase gamma ray values and the ability to distinguish between lithologies is reduced (Mondol, 2015).

Gamma ray logs can also be used to interpret depositional environments by analysing various shapes produced throughout the log (Figure 4.8). The following interpretations are listed by Mondol (2015):

- Cylinder shapes are interpreted as uniform deposition such as aeolian dunes, tidal sands, fluvial and turbidite channels and proximal deep-sea fan deposits.

-Bell shapes represent fining upward sequences interpreted as tidal sands, alluvial sand, fluvial channels, point bars, lacustrine deposits, deltas, turbidity channels and proximal deep-sea fan deposits.

-Funnel shapes, represent coarsening upward sequences and are interpreted as barrier bars, beach sands and crevasse splays, distributary mouth bars and distal deep-sea fan deposits.

Figure 4.8: Depositional environments represented by various gamma ray log responses *(after Mondol in Bjørlykke, 2015).*

4.3.2 Sonic Log

Sonic logs provide information regarding porosity, and more importantly, whether pores are gas or liquid saturated. This is conducted by measuring how sound waves travel through rocks, and is registered as Δt, the inverse of velocity. The velocity of sound waves will render differently whether it travels through a liquid, gas or a cemented rock. For example, sound waves travelling through water will be slower than sound waves travelling through a highly-cemented rock. The sonic log is therefore important when determining the depth at which quartz cementation is initiated and marks the transitional zone between mechanical compaction and chemical compaction (Mondol, 2015).

In order to convert the inverse of velocity (Δt) into P-wave velocity the following equation is used:

$$\text{Equation 15.} \quad Vp \left(\frac{m}{s}\right) = \frac{1}{\Delta t} \, x \, 304899$$

4.3.3 Density Log

The bulk density log (ρ_{log}) registers the density of solid phases (ρ_{matrix}) as well as fluid density (ρ_{fluid}) and can thereby be computed into porosity-density (φ_D) using the following equation:

$$\text{Equation 16.} \quad \varphi_D = (\rho_{matrix} - \rho_{log}) / (\rho_{matrix} - \rho_{fluid})$$

When using this equation, the appropriate matrix and fluid densities have to be assumed. The following table shows a few commonly used values when estimating the porosity density of a reservoir (Mondol, 2015).

Table 4.3: Common mineral and fluid densities found in reservoirs.

Mineral	Density (g/cm³)	Fluid	Density (g/cm³)
Quartz	2.650	Pore water (brine)	1.025
Calcite	2.710	Oil	0.850
Illite	2.660	-	-
Kaolinite	2.594	-	-

4.3.4 Neutron Log

Neutron logs are a measure of the hydrogen index contained within a well. Hydrogen is largely found in formation water meaning in turn that neutron logs give an estimate of rock porosity. Neutron logs can however lead to both over- and underestimation of porosity and are best used in conjunction with other logs. For example, shales can give unrealistically high neutron readings due to the water bound within these mineral structures. Conversely, when hydrocarbons are present within a formation an underestimation of porosity is presented. This underestimation is caused by gases having fewer hydrogen atoms per unit of volume when compared to water or oil (Mondol, 2015).

4.3.5 Uplift Estimation

In order to estimate the uplift that has transpired through time, the interval transit time (V_p) is plotted on a logarithmic scale against depth on a linear scale. The plotted values are then compared to empirically tested compaction trends of similar lithologies. Diagenetic changes that take place with burial do not change subsequent to uplift and therefore represent the sediments deepest burial. Figure 4.9 contrasts the same stratigraphic interval in

two different wells. The green curve shows an uplift of 750m illustrated by lower interval transit times but occurring at a shallower depth (Mondol, 2015).

4.3.6 Geothermal Gradient

The geothermal gradient (G_g) is calculated in order to estimate the maximum temperature that sediments were exposed prior to exhumation. There are however some uncertainties when estimating the geothermal gradient as this is highly dependent on ambient tectonic settings through time. In tectonically active areas the geothermal gradient may become elevated whereas in rapidly subsiding basins with high sedimentation rates the geothermal gradient is reduced (Figure 4.9). Steep geothermal gradients are produced by rapid uplift (caused by e.g. isostatic rebound and erosion) bringing warmer rocks to the surface (Bjørlykke, 2015). The southwestern Barents Sea is no longer tectonically active meaning that today's geothermal gradient may not be representative of the geothermal gradient that sediments have endured since the Triassic period.

The following equation is used to derive the present geothermal gradient:

$$\textbf{Equation 17.} \quad G_g = \frac{T_{bh} - T_{sf}}{T_{bh} - D_{sf}} x \ 1000$$

where T_{bh} signifies the recorded bottom hole temperature, T_{sf} represents the mean sea floor temperature, T_{bh} is the depth at which temperature was recorded and D_{sf} represents water depth. The recorded bottom hole temperatures may also be somewhat misleading as the drilling mud tends to cool the ambient surrounding during drilling.
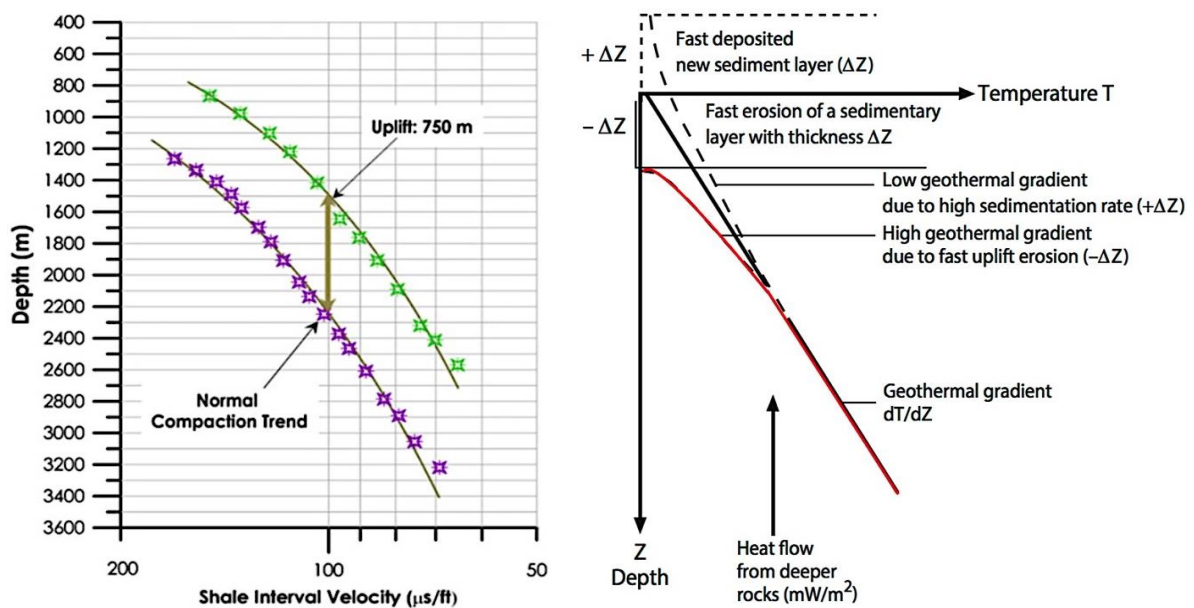

Figure 4.9: (*Left*) **Estimated uplift based on sonic logs and shale compaction data.** (*Right*) **Geothermal gradient as a function of uplift or subsidence** (*after Bjørlykke, 2015*).

5. Results

This chapter intends to illustrate the results from each subsequent method that has previously been described. Results are based on 20 samples throughout Fruholmen Formation in Hanssen (7324/7-2) and 20 samples from Fruholmen and Stø Formations collectively in Wisting Central (7324/8-1). The chapter is principally subdivided into facies whereby sedimentological descriptions and petrographic results from Hanssen and Wisting Central will be conjointly represented. Note that no samples are available from Facies 5, 6, 7 or 8 in Hanssen, whereby a short presentation of the core log will be given at no further detail.

5.1 Sedimentological Description

Facies descriptions and formation boundaries are based on observations made during drill core logging. The use of core photos and references to biostratigraphic subdivisions were provided, with permission by OMV Norge AS, and allowed a more detailed and conceptual stratigraphic model to be proposed in the following discussion.

The studied core intervals through wells 7324/7-2 and 7324/8-1 (Hanssen and Wisting Central, respectively) penetrate Mesozoic reservoirs in the Late Triassic to Early Jurassic Realgrunnen Subgroup consisting of the Fruholmen Formation, Stø Formation, and possibly a condensed to partly eroded Nordmela Formation.

The wells flank the Mercurius High and are located 7km apart within the Hoop Fault Complex (Figure 5.1). The cored interval from both wells is interpreted to represent an overall regressive deltaic-shoreline system recording a complex marginal marine setting that shows evidence of tidal background sedimentation. The sedimentary logs coupled with wireline log data (GR, NPHI, RHOB) (Figure 5.31) all support a coarsening upward − shallowing upward motif capped by a sharp-based fluvial-tidal succession forming the main reservoir in the Stø Formation.

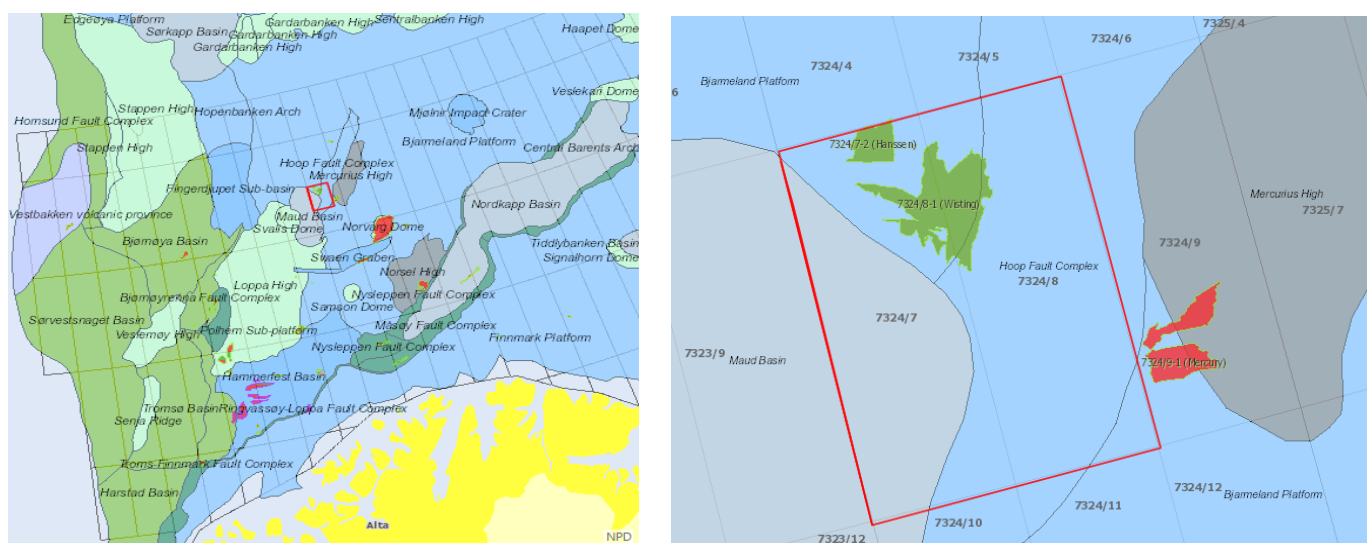**Figure 5.1: Geographic location of Hanssen (7324/7-2) and Wisting Central (7324/8-1) (*modified after NPD Fact Maps, 2016*).**
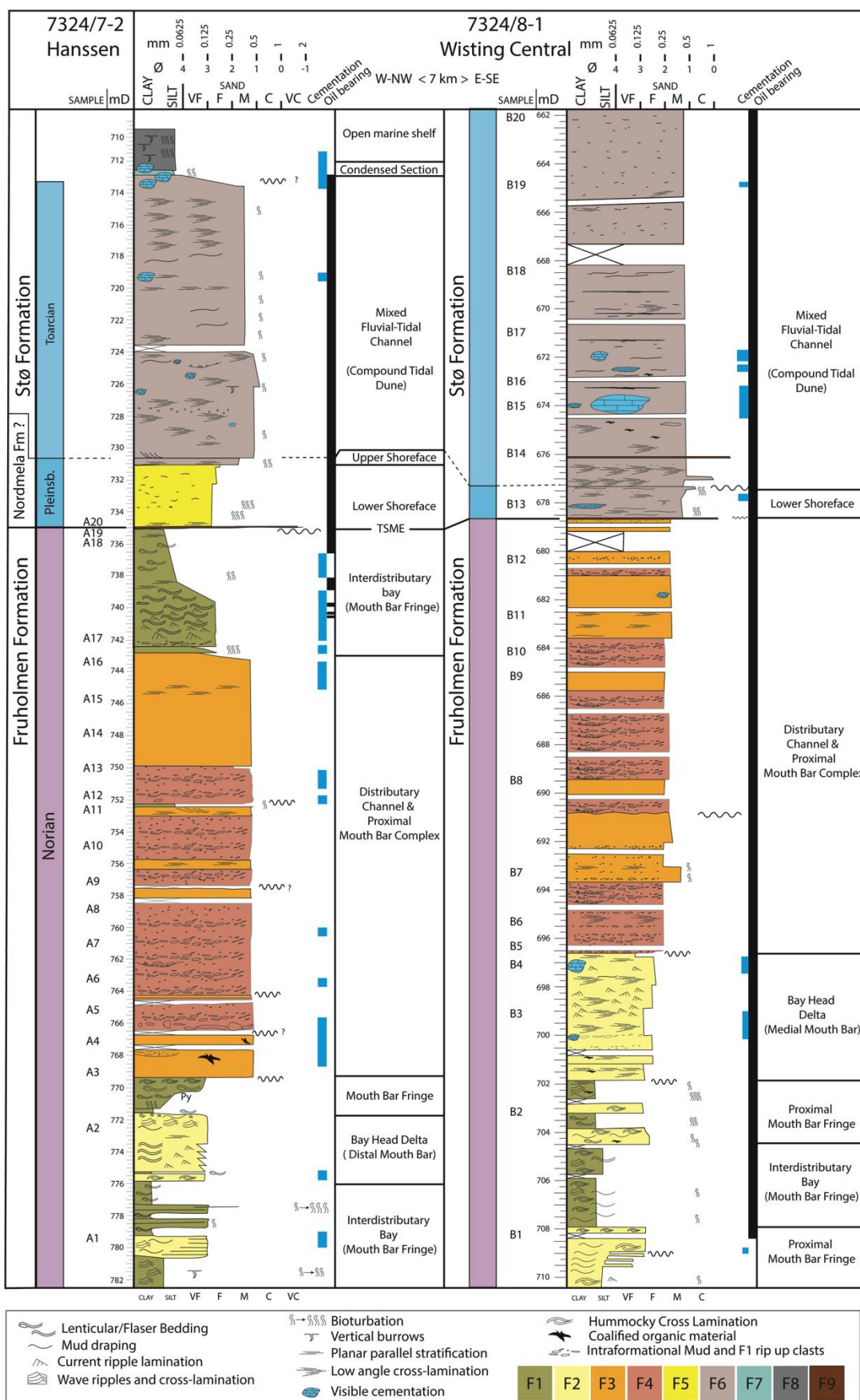
Figure 5.2: Composite sedimentary logs of the Fruholmen-Stø formations in the Wisting Central and Hanssen wells showing the progression of depositional environments associated with a coarsening-upwards/shallowing-upwards trend prior to major flooding above the Stø Formation.

Table 5.1: Outline of facies, facies association and depositional environment interpretation

Facies	Grain size	Description		Bed Thickness	Facies Association	Depositional Environment
F1	Interlaminated mud and sandstone	-Flaser/wavy/lenticular -Sharp-based fining-upwards -Low to moderate bioturbation -Low-diversity of trace fossil assemblages -Bidirectional ripple forms -Convolute bedding -Synerisis cracks -Carbonaceous laminae and mudstone drapes -Low Net to Gross		Varying thickness (centimeter – decimeter)	Mouth Bar Fringe Zone	Interdistributary bay
F2	Fine to very fine grained sand	Combined flow ripple laminations Hummocky cross stratification Low bioturbation Carbonaceous laminae and mudstone drapes Low Net to Gross >> Facies 1		Decimeter (s)	Medial to Distal Mouth Bar	Bay-head delta front
F3	Fine to medium grained sand	-Carbonaceous fragments -Coal clasts -Structureless to massive appearance -Occasional siderite clasts		Meter scale	Proximal Mouth Bar	Distributary mouth bar
F4	Fine to medium grained sand	-Intraformational mud rip-up clasts -Scour and fill structures -Genetically related to F3		Meter(s) scale	Distributary Channel	Distributary channel complex
F5	Fine to very fine sand	-Moderately bioturbated		Decimeter	Shallow Marine	Lower shoreface
F6	Fine to medium grained sand	-Organic material -Bioturbation -Cross-cutting beds -low bioturbation -Mud drapes -Mud rip-up clasts	-Cross-bedding -Planer lamination -Asymmetric ripple lamination -Extra-formational clasts -Concretions	Decimeter to-meter beds	Compound tidal dune	Mixed Fluvial Tidal Channel
F7	Sand-bearing siltstone	-Cemented -Concretions -Glauconitic		20 cm	Depositional hiatus	Condensed section
F8	Mudstone	-Intensely bioturbated -High diversity of trace fossil assemblages		--	Offshore shelf	Open marine
F9	Gravel conglomerate	Sharp and erosional boundary		Centimeter (s)	marine ravinement surface	Transgressive lag deposit

A. Fruholmen Formation - Distributary channel & mouth bar model

Dip-oriented Cross-Section - Single deltaic lobe

Onshore

Offshore

Bar Complex Scale

Cross-sectional View   Plan View

F4   F3   F2   F1

C   Si   Vf   F   M   Grain Size Trend

Proximal Mouth Bar
Main Body

Distributary Channel

Proximal Mouth Bar

Distributary Channel & Axis of Bar Complex

C   Si   Vf   F   Grain Size Trend

"Distal Mouth Bar"
Dominantly
Traction
Deposits

"Very Distal Bar"
Dominantly
Suspension
Deposits

Medial Mouthbar Complex & Proximal Bar Fringe

C   Si   Vf   F   Grain Size Trend

Dominated by suspension deposits

Fringe of Bar Complex

B.

Stø Formation - Compound tidal dune model

i.

Simple dune foresets

mud drape   Master surfaces

ii.

Simple dune foresets

33*

Ebb flow (dominant)   1m

Master surfaces

Figure 5.3: Conceptual models applied to the (A) Fruholmen Formation and (B) Stø Formation. (A) Grain size trends and sedimentary structures for the proximal, medial and distal portions of a channel and mouth bar complex. The Fruholmen Formation formed by progradation and compensational stacking of mouth bar and distributary channel elements *(after Wellner et al., 2005).* **(B.i) Compound cross strata form by the migration of simple dunes down master surfaces that represent the lee face of a larger compound dune** *(after Allen, 1980).* **(B.ii) The internal structure of a migrating compound tidal dune implies a forward accretionary architecture** *(after Olariu et al., 2012)* **Core from both wells indicates a prominent dip orientation of cross-stratified sets in the Stø Formation interpreted as a tidal environment within a marine setting**

The Fruholmen Formation has been interpreted using the application of architectural elements within a conceptual framework to a mouth bar complex of a larger deltaic system (Figure 5.3.A). The process-driven mouth bar model of Wellner et al. (2005) from a fluvial dominated portion of the modern Mississippi River delta is suggested as a useful analogue to the Fruholmen Formation.

A thin succession of (?)Nordmela Formation occurs in both wells forming a transition from Fruholmen to Stø (Figure 5.2). This basal contact is marked by a gravelly lag deposit interpreted as a transgressive lag, which juxtaposes bioturbated shallow marine facies over distributary channel facies of the Fruholmen Formation.

The Stø Formation in the Wisting area is interpreted as a compound-dune complex (after Olariu et al., 2012) influenced by strong tidal currents and minor fluvial incision (Figure 5.3.B).

5.1.1 Facies 1

Successions of Facies 1 (F1) occur solely in the Fruholmen Formation and are 2-3m thick and pervasively heterolithic. F1 shows characteristic tidal signatures of flaser-, wavy-, and lenticular bedding in addition to normally graded decimetre-scale sets of sharp- to erosive-based oscillatory and hummocky wave ripples with faintly laminated siltstone and structureless mudstone drapes (Figure 5.4).

Common primary sedimentary structures observed in F1 are convolute bedding, bi-directional current ripple laminations, and mud draping of ripple foresets. Although predominantly non-bioturbated, several intervals within F1 exhibit syneresis cracks and a low to moderate level of bioturbation in addition to an apparent low diversity of trace fossils assemblages.

Facies Association

The sparsely bioturbated heterolithic deposits and low diversity of trace fossil assemblages may indicate a stressed-environment and/or brackish water conditions, because the diversity and intensity of bioturbation, in addition to the size of traces, decrease proportionally with decreasing salinity (Dashtgard & La Croix, 2015). Deposits in F1 represent a low-energy mouth bar environment with a moderate influence from tides. Processes associated to F1 are interpreted as (1) hyperpycnal flows formed during river-flood events with partial reworking by storm-waves, creating tempestites, and (2) inter-flood tidal background sedimentation that generates a discreet yet subtle cyclic bundling of

sequences. The sparse occurrence of *Planolites*, *Teichichnus* and *fugichnia* are indicative of deposition on tidally influenced sub tidal bars (Gingras et al., 2012).

The depositional environment is suggested as an interdistributary bay with a position receiving mostly suspension deposits from the mouth bar and channel (Wellner et al., 2005) (Figure 5.3.A).

The heterolithic deposits of F1 in 7324/7-2 are more thinly bedded and noticeably finer grained than in 7324/8-1, which may relate to differences in the size of distributary channels on the delta plain between the two areas or proximity to source areas. Both factors would have an impact on the amount and calibre of sediment supplied to the mouth bar fringe zone.

Figure 5.4: Core photographs demonstrating sedimentary structures common to Facies 1 and the mouth bar fringe depositional environment (Scale bar is 10cm). (A) Sharp based, normally-graded tempestite beds containing wave ripple and hummocky cross-lamination, graded siltstones and mudstone drapes. Bioturbation intensity is low (BI 0-1) with *Planolites* (P), *fugichnia* (fu) and *Teichichnus* (Te) (Well 7324/7-2: 781.1-781.8 mD). (B) Heterolithic ´wavy bedding´ with mud drapes (Well 7324/8-1: 707.25-707.65 mD). (C) Convolute bedding and a combination of traction and suspension deposits (Well 7124/7-2: 777.1-778 mD). (D) Convolute bedding within a heterolithic unit containing coal fragments (Well 7324/8-1: 702.2-702.6 mD). (E) Lenticular bedding and a moderate bioturbation intensity (BI=2-3). Possible syneresis cracks (sy) suggest brackish conditions. A low diversity and small size of trace fossils, *Planolites* (P), may indicate opportunistic colonization in a stressed environment (Well 7324/7-2: 776-776.65 mD).

5.1.2 Facies 2

Facies 2 (F2) forms a sharp and erosional boundary above F1 and is associated with an increase in sand content (Figure 5.5.A-B). Sedimentary structures consist of uni-directional current ripples, mud drapes, plane parallel stratification with carbonaceous laminae, similar fining-upwards units to those described in F1, and centimetre to decimetre-thick units of wave- and combined-flow ripples (Figure 5.5.A-E).

Facies Association:

Facies 2 is interpreted as a transition zone between distal (F1) and proximal (F3) environments in an interdistributary bay and mouth bar system. Heterolithic stratification is a common feature in intertidal environments (Davis, 2012). Dalrymple et al., (2015) suggest the mudstone layers draping current-rippled sands accumulate by slow settling from dilute muddy suspensions in a tide-dominated environment. An increase in sandstone bed thickness coupled with the increase in grain size from F1 to F2 is in accordance with the larger scale coarsening-upward progradational trend observed within the Fruholmen Formation. There appears to be a larger proportion of storm reworked hummocky cross-stratified intervals in well 7324/8-1, suggesting a shoreline position more open to the coast when compared to well 7324/7-2. The depositional environments of F2 are interpreted as a proximal fringe to distal mouth bar zone (Figure 5.3.A) of a bay head delta front.
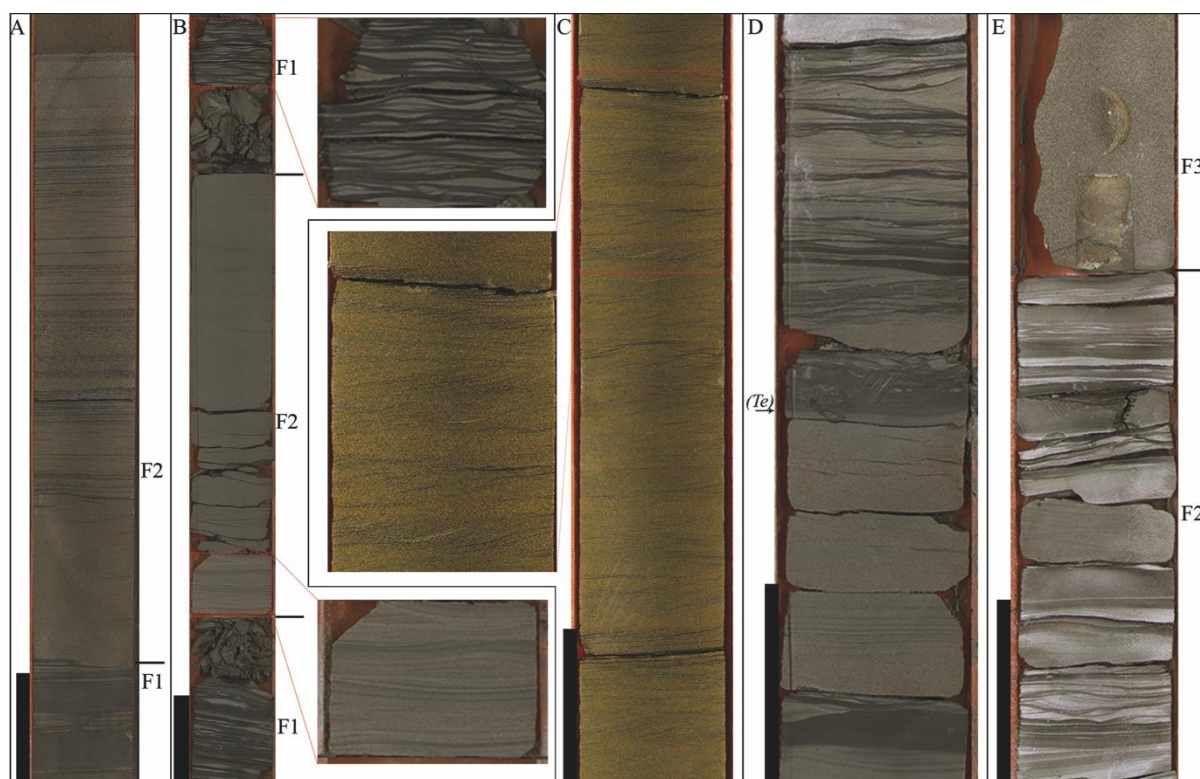
Figure 5.5: Core photographs of characteristic features in Facies 2 (Scale bar is 10cm). F2 is associated with medial to distal mouth bar and fringe environments typical of low energy bay head deltas. (A) Sharp and erosional contact of F2 containing plane parallel stratification with carbonaceous lamina (Well 7324/8-1: 701.25-701.95 mD). (B) Sharp contact of F2 containing hummocky cross stratification and faint mud drapes (LOWER INSET) overlain by lenticular bedding of F1 (UPPER INSET) (Well 7324/7-2: 775.15-776 mD). (C) Unidirectional current ripple laminations with mud draped foresets (flow is from right to left). Few sets climbing at very low angles (UPPER INSET) (Well 7324/8-1: 698.15-698.65 mD) (D) plane parallel and wave ripple laminated sandstone with mud drapes and an isolated occurrence of *Teichichnus (Te)* (Well 7324/7-2: 773-773.4 mD). (E) Sharp transition from F2 to F3. F2 is more heterolithic and overlain by a structureless sandstone unit of F3 (Well 7324/7-2: 769.15-769.6 mD).

5.1.3 Facies 3 and 4

Facies 3 (F3) consists of thick (1-3m) erosively-based structureless, planar or cross stratified sandstones with gravel-sized mud rip up clasts and coal fragments (Figure 5.6A,B,D).

Facies 4 is a predominantly matrix-supported intraformational conglomerate with mud-rip up clasts of F1 ranging from gravel to cobble-sizes (Figure 5.6.B-E). The mudstone clasts are associated with the distal and lower energy interdistributary bay heterolithic deposits of F1.
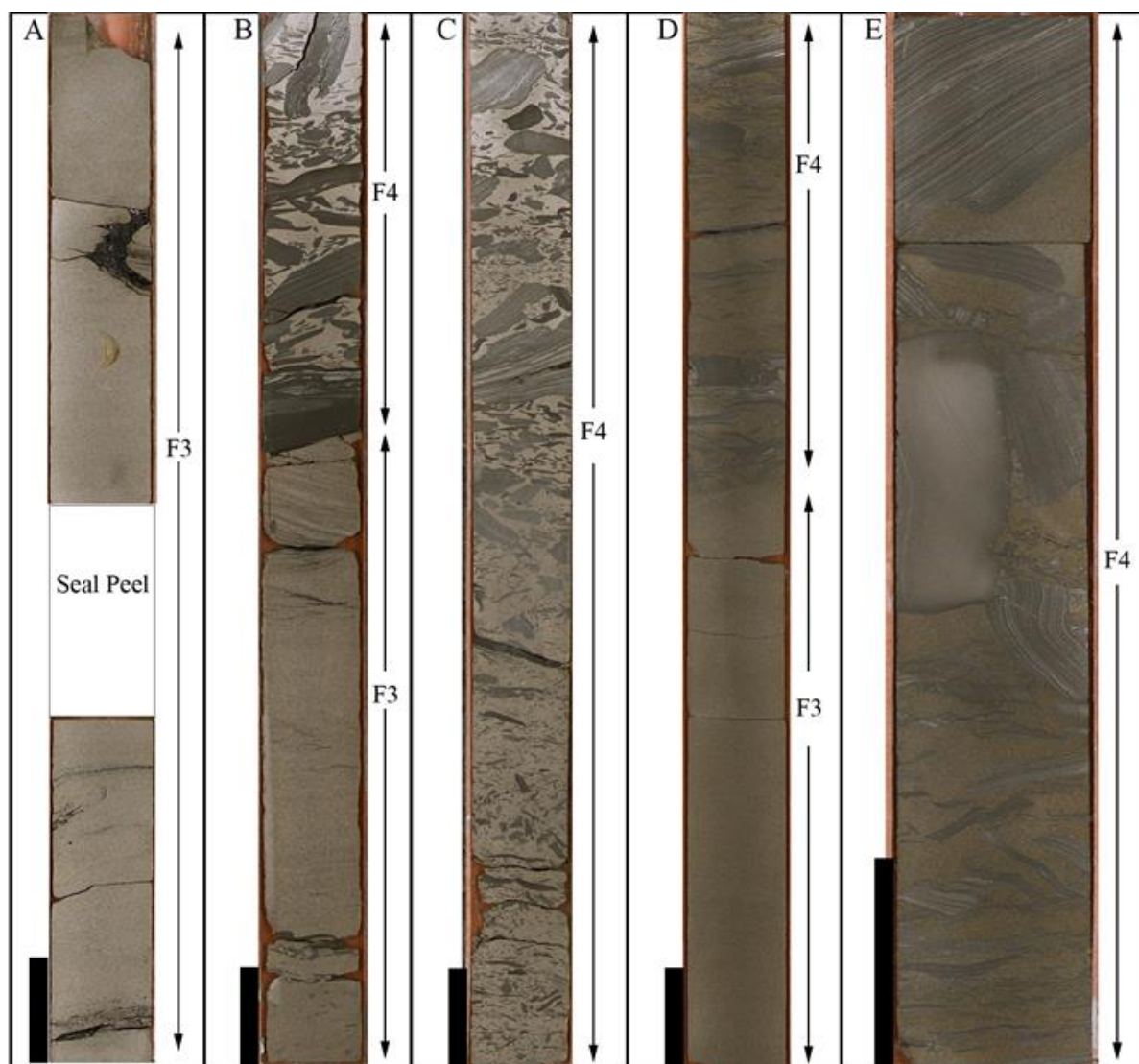
Figure 5.6: Core photographs depicting mouth bar and distributary channel environments of Facies 3 and Facies 4 (Scale bar is 10cm). (A) Structureless sandstone of F3 with faint carbonaceous laminae, mud and coal rip up clasts (Well 7324/7-2: 767-768 mD). (B) Common interbedding of F3 and F4 suggests a dynamic change in flow regime between mouth bar environments of F3 and scour-and-fill of channels in F4 (Well 7324/7-2: 752-753 mD). (C) Distributary channel deposits of F4 show an inverse grading of intraformational F1 mud clasts (Well 7324/7-2: 760-761 mD).(D) Distributary channel of F4 overlying structureless mouth bar deposits of F3 (Well 7324/8-1: 689-690 mD). (E) Intraformational mud rip up clasts resemble heterolithic F1 fringe zone deposits (Well 7324/8-1: 688-689 mD)

Facies Association

The upwards coarsening trend from F1 to F4 developed in both studied wells attests to the progradational trend in the Fruholmen Formation. F3 and F4 demonstrate the higher–energy characteristics of a mouth bar and distributary channel environment. The occurrence of F1 mudstone clasts suggests erosional scouring by distributary channels. In well 7324/7-2, F3/F4 is overlain by a succession of heterolithic interdistributary bay deposits belonging to the mouth bar fringe zone of F1. Frequent avulsion and abandonment of distributary channels could explain this compensational stacking pattern of deltaic lobes and mouth bar elements. The juxtaposition of facies (F3/F4 with F1) and the abundance of intraformational

mudstone clasts most likely formed by autogenic shifting within the larger deltaic system, as opposed to allogenic processes (e.g. Transgressive-Regressive cycles and relative sea-level changes).

5.1.4 Facies 5

F5 is a thoroughly bioturbated sandstone that expresses a slight coarsening upward trend. The relatively thin succession in both wells may be a condensed unit representing the Nordmela Formation. Bioturbation has destroyed most primary sedimentary structures, with exception to a few intervals of wave ripple bedforms and mud drapes (Figure 5.7).

Facies Association

The increased level of bioturbation in this unit marks a distinct change from what has
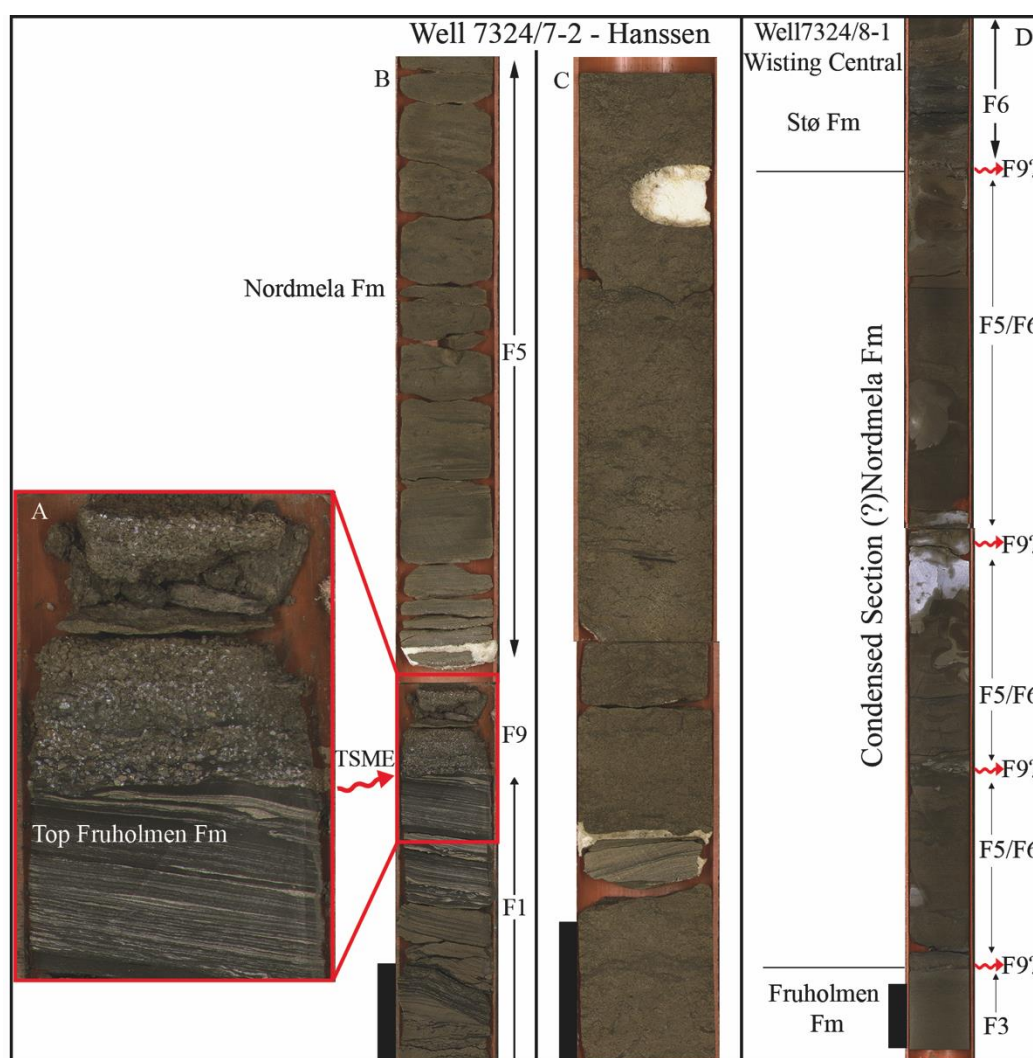
Figure 5.7: Core photographs of F5 showing: (A-B) a transgressive lag (F9) marking the Top Fruholmen Fm and a Transgressive Surface of Marine Erosion (TSME) overlain by a lower shoreface sequence showing a heavily bioturbated texture in the Hanssen Well (7324/7-2: 731.60- 732.30 mD). (D) In the Wisting Central well, the time-equivalent succession overlying the Fruholmen Formation has a very thin lag and highly cemented transitional zone representing a possible condensed section (Well 7324/8-1: 677.20-678.80 mD).

been previously described in the Fruholmen Formation. Facies 5 was deposited above a gravel lag in well 7324/7-2 interpreted as transgressive surface of marine erosion (Figure 5.7.A-B). This contact and juxtaposition of facies has important sequence stratigraphic, lithostratigraphic, and chronostratigraphic implications. The transgressive lag therefore marks the top of the Fruholmen Formation in Well 7324/7-2, also signaling a major flooding event of regional to possibly global significance, and the introduction of a lower shoreface shallow marine environment where a brackish interdistributary bay and fluvial-deltaic system were once located.

5.1.5 Facies 6

Facies 6 (F6) comprises the entire Stø Formation in both studied wells. Primary sedimentary structures observed from core are planar cross-stratification, planar parallel stratification, mud drapes, terrigenous debris, and mud rip-up clasts (Figure 5.8). Intervals

Figure 5.8: Characteristic facies of F6 in the Stø Formation (Scale bar is 10cm). (A) Faint trough cross stratified sandstone with abundant carbonaceous debris and flaser mud rip up-clasts (Well 7324/8-1: 670-670.4 mD). (B) Cross-stratification and tidal bundling capped by fluvial erosion and a thin channel lag (Well 7324/8-1: 676-676.7 mD). (C) Decimetre sets of cross-stratification with mud draped intervals indicating a tidal influence and cyclic bundling. The uppermost section is moderately bioturbated (Well 7324/7-2: 715-716 mD).

appearing more structureless are due to bioturbation. This reworking might enhance the reservoir connectivity by destruction of mud drapes and finer-grained intervals acting as potential barriers to fluid flow.

Facies Association

The Stø Formation displays a markedly different depositional environment than that which is observed in the previously mentioned facies. Aggradational stacking patterns of decimeter to meter scale trough and planar cross-stratified sets are interpreted as a complex of subaqueous dunes formed in large sandflats within a high-energy shallow marine to fluvial-tidal transition zone environment.

Compound tidal dunes formerly called sandwaves have been widely recognized in modern shallow-water tidal environments (Allen, 1980; Olariu et al., 2012). Their development is governed by asymmetrical currents that produce flow separation at the crest of bedforms resulting in avalanching of grains along the lee side of bedforms and occasional preservation of mud drapes and bioturbated zones during stages of decreased flow (Allen, 1980). A consequence of this flow asymmetry is that the internal surfaces within compound dunes (master surfaces down which a simple dune migrates) dip in the same general direction as the dominant current, resulting in a forward-accretionary architecture (Figure 5.3.B) (Olariu et al., 2012).

5.1.6 Facies 7 and 8

Facies 7 and Facies 8 (F7 and F8, respectively), are described only from Well 7324/7-2 above the Stø Formation because only this well extracted core through the top of the reservoir section. These formations are discussed for the sake of completeness in the facies analysis, however there was no sampling and further analysis executed.

F7 is a heavily cemented, glauconite-bearing zone of 20 centimeters above the Stø Formation. F8 is a silty claystone that has been extensively bioturbated, indicative of open marine shelf conditions (Figure 5.9). Regionally important information can be inferred from the juxtaposition of F7 and F8 overlying the Stø Formation and main reservoir unit. With its glauconitic content, and heavy cementation, F7 is suggested to represent a condensed section, depositional hiatus and important time-stratigraphic boundary. The placement of a maximum flooding surface at this interval above the Stø Formation is inferred, as sedimentation resumed in an open marine shelf environment, marking an abrupt change in the regional palaeogeography.
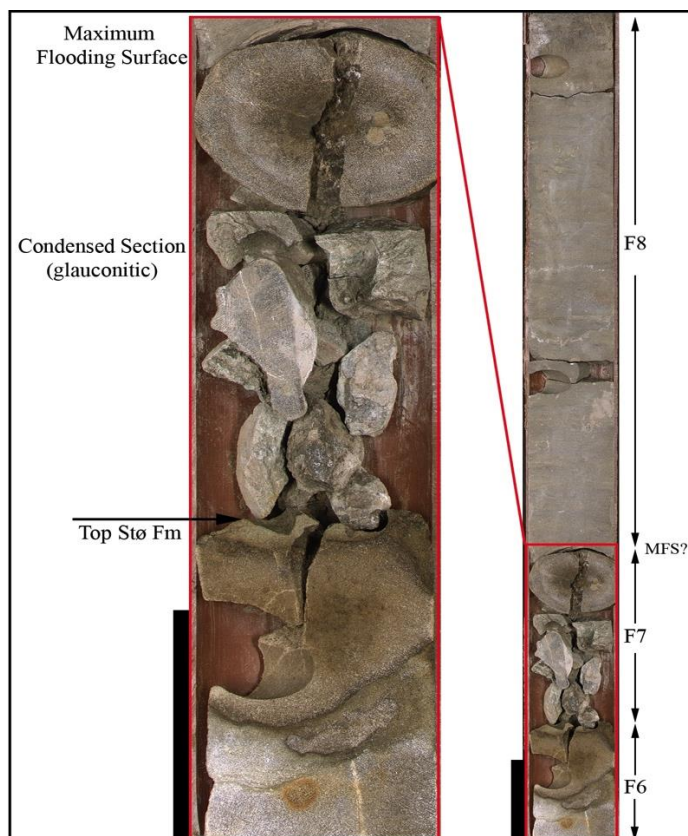
Figure 5.9: Top Stø Formation showing the condensed section of F7 and open marine bioturbated siltstone of F8 (Well 7324/7-2: 712-713 mD).

5.2 Petrographic Analyses

Petrographic results are primarily presented by facies in order to determine whether reservoir quality varies between different depositional environments. Results are typically presented in diagrams with average values for each facies (for individual sample results, see Appendices).

5.2.1 Mineralogy

Constituent framework grains are presented in a ternary diagram, plotted using average point counted results for each analysed facies (Figure 5.10). Quartz, feldspar and lithic fragments are recalculated to represent 100% of each sample and subsequently averaged for each facies.

Facies 1 through 4 plot as sub-arkoses indicating moderate feldspar compositions (average sandstone composition for Facies 1 through 4: $Q_{73.75}$ $F_{22.70}$ $L_{3.56}$). Facies 6 indicates a higher quartz content and minor feldspar constituents, plotting on the boundary between sub-arkose and quartz arenite (average sandstone composition for Facies 6: $Q_{94.09}F_{5.61}L_{0.30}$). All respective facies show negligible amounts of lithic fragments.

Figure 5.10: Sandstone classification of Fruholmen Formation (Facies 1 – 4) and Stø Formation (Facies 6).

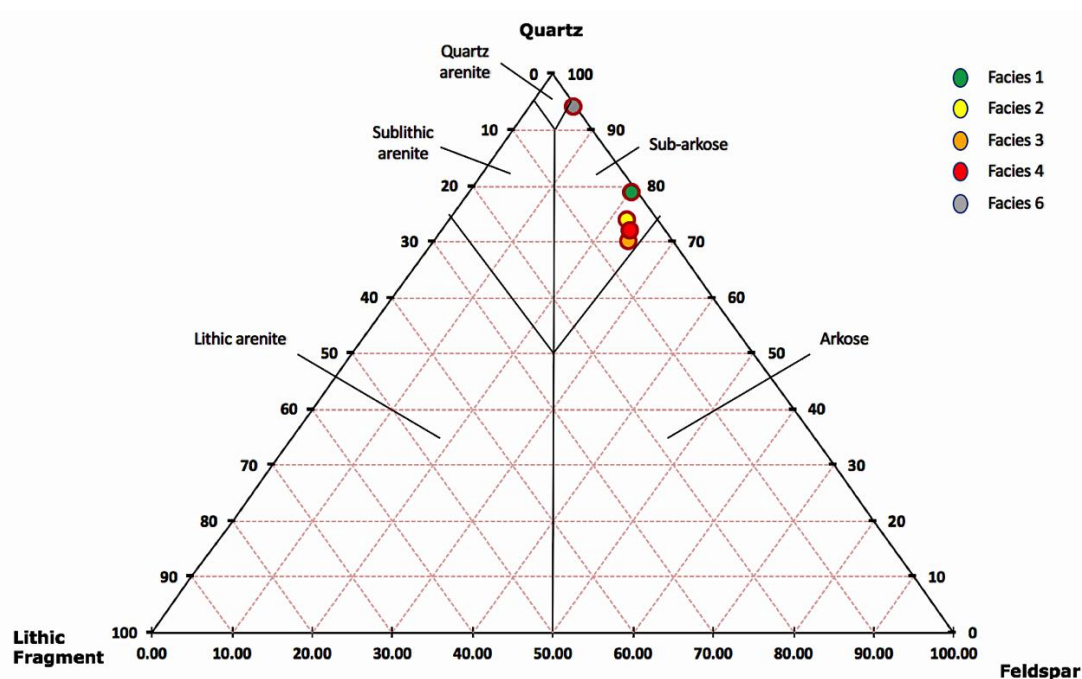Mineral composition of Facies 1, 2, 3, 4, and 6 based on average bulk XRD-results are presented in Figure 5.11. Facies 1 through 4 illustrate similar trends in which quartz represents 50-60%, feldspars (plagioclase, anorthite, albite and microcline) 20-25% and muscovite/illite 6-12%. Smaller quantities (0-8%) of kaolinite, dickite siderite and chlorite are seen throughout each subsequent facies. Calcite cement is seen in moderate quantities throughout, but is most prominent in Facies 2, representing an average of 11%.

Facies 6 illustrates a slightly differing trend whereby quartz clearly dominates mineral composition at 87%. Feldspar and calcite cement represent 7% and 6% respectively whereas kaolinite and pyrite are detected as trace amounts.

Furthermore, point counting is imperative for determining the intergranular volume as well as sub-categorizing minerals such as quartz and feldspar. Similarities in results are seen between detrital grains in bulk XRD-analysis and point counted samples. However, a subsequent distinction is made when point counting mineral grains between mono- and polycrystalline quartz, lithic fragments, matrix (defined as dispersed allogenic clay and feldspars (microcline, plagioclase and altered/unidentifiable feldspars). Quartz cement is also subcategorized but is difficult to estimate with accuracy through microscopic analyses. However, when evident, it is point counted as a separate entity. Porosity is included in each point counted sample, thus results are not directly comparable to bulk XRD-analysis. For individual point count results see Table 10.4 and 10.5 in Appendices.
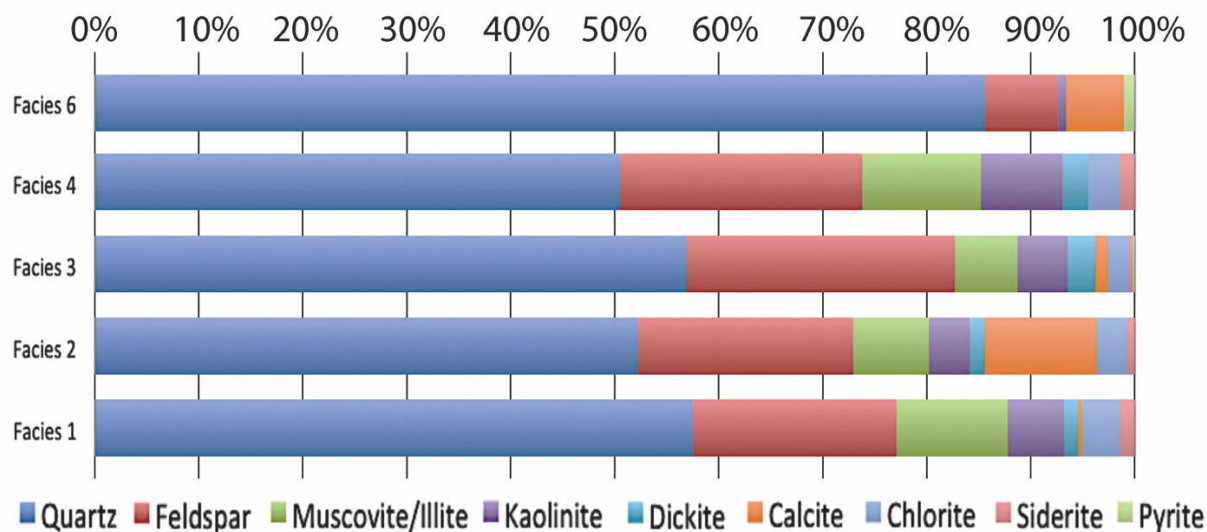
Figure 5.11: Bulk-XRD-results based on average mineral composition within each sampled facies.

5.2.2 Detrital Grains

Quartz

Quartz is the governing mineral seen throughout each subsequent facies. Within Facies 1 through 4, quartz comprises 50-60% of constituent minerals according to XRD- and point counted results respectively. A slight deviation is seen in Facies 6 between average bulk XRD and point counted results. XRD-results display an average of 80-90% quartz content whereas point counted results indicate an average of 60-70%.

All point counted samples show a predominance of monocrystalline quartz with minor percentages (1-10%) polycrystalline quartz (Table 10.4 and Table 10.5)

Feldspar

During point counting, feldspars are sub-categorized as microcline, plagioclase or altered/unidentifiable (Table 10.4 and Table 10.5) All subsequent facies show a large percentage of altered and unidentifiable feldspars meaning that feldspars could not be accurately identified as either microcline or plagioclase through microscopic analyses. However, bulk XRD-results are readily able to differentiate between plagioclase and microcline which is further averaged with regard to each sampled facies. Results show a predominance of plagioclase in all respective facies with constituent percentages ranging from 6 to 19 (Figure 5.12). Minor percentages of microcline are seen in Facies 1 and 6 whereas Facies 2, 3 and 4 comprise average percentages ranging between 6 to 8. Feldspar content decreases considerably in Facies 6 when compared to Facies 1 through 4.
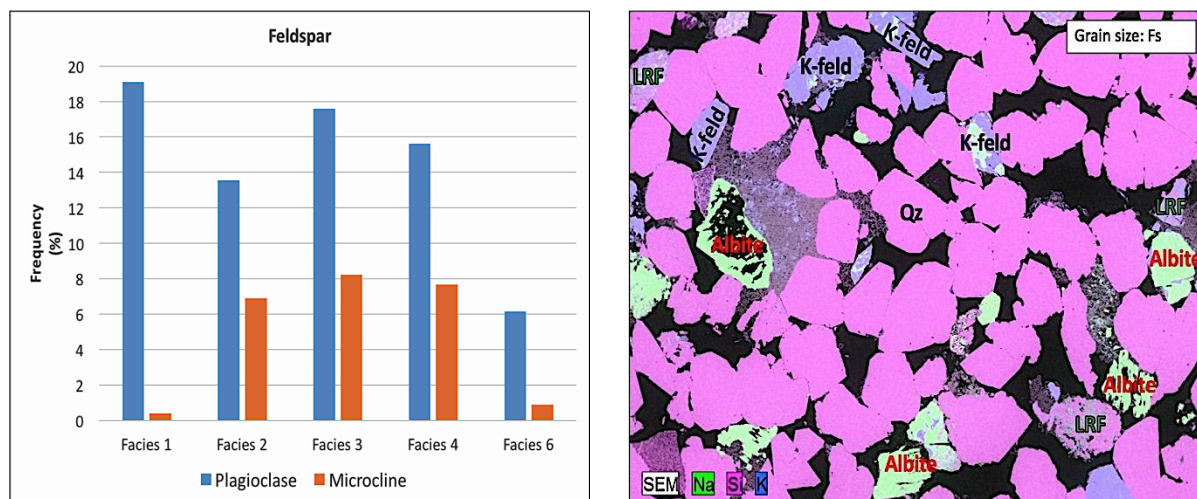
Figure 5.12: (Left) Feldspar distribution according to XRD-results. Plagioclase is seen as the predominant mineral throughout all subsequent facies. (Right) Plagioclase (albite) and microcline (k-feld) seen in Sample A12, Facies 3. SEM image showing relatively even spread of albite and k-feld, an abundance of quartz and negligible amounts of lithic rock fragments.

Lithic fragments

Lithic fragments are identified through point counting (Table 10.4 and Table 10.5), however are difficult to recognize due to high degrees of alteration. No separate sub-divisions of lithic fragments have been established as this would lead to subjective results. Lithic fragments account for a small percentage in Facies 2, 3 and 4 whereas Facies 1 and 6 show negligible proportions.

5.2.3 Authigenic Minerals

Authigenic minerals such as, kaolinite, dickite and illite are difficult to identify through microscopic analysis. Bulk XRD-results give an estimate of which authigenic minerals are found and at which given percentage per sample. To be certain, Scanning Electron Microscopy was carried out on a few selected samples (Table 10.2 and Table 10.3) in order to determine which authigenic minerals are dominant in certain facies. Quartz cement is estimated through point counting, but is more clearly depicted through Cathodoluminescence. Few samples were selected for CL-analysis (Table 10.2 and Table 10.3) and highlight the extent of quartz cementation.

Quartz cement

According to point counted samples, quartz cement is seen to some degree in all subsequent facies (2-10%) (Table 10.4 and Table 10.5). SEM and CL images clearly illustrate quartz cement as both grain overgrowths and fracture infills.
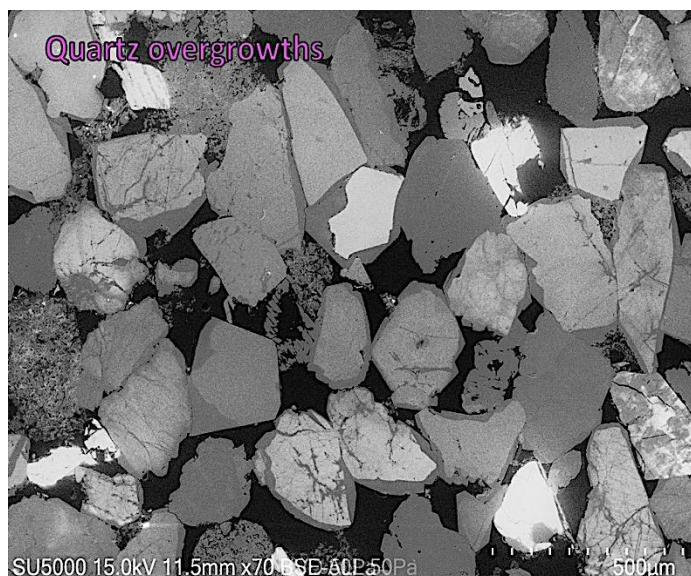
Figure 5.13: Quartz overgrowths seen in two overlapping images taken using SEM and CL. Authigenic quartz is seen lining the original quartz grains as well as filling fractured grains (sample A12, Facies 3).

Figure 5.13 illustrates two overlapping images, the bottom one taken with backscattered light (SEM) and the top one using cathodoluminescence (CL). This illustrates the contours of the original quartz grains as well as the authigenic quartz overgrowths and fracture infills.

Figure 5.14 shows the same image seen through SEM, CL and ultimately the two images overlapped. Figure 5.14.A illustrates what appears as several large, opaque quartz grains (SEM-backscattered light). Figure 5.14.B illuminates the original quartz grains and shows a less prominent shade of grey where quartz overgrowth is detected (CL). Figure 5.14.C ultimately shows the two images overlapped, illustrating the significance of quartz overgrowth. These images demonstrate the difficulty that is encountered when point counting quartz cement through an optical microscope and the possibility of over- or underestimating quartz cement is highly probable.

A   B   C

Figure 5.14:(A) taken using SEM, showing large opaque grains. (B) taken using CL, illuminating original quartz grains as wells as showing less prominent shades of grey illustrating quartz overgrowths. (C) shows both images overlapped, depicting where quartz cement lines the original grains as well as fills fractures (sample A12, Facies 3).

Kaolinite

Kaolinite is mainly determined using bulk XRD-results as it is difficult to ascertain and distinguish from other authigenic minerals through optical microscopic analysis. Kaolinite is seen mainly in Facies 1 through 4 with sample compositions averaging between 3 to 8%. When observed using Scanning Electron Microscopy, kaolinite is commonly seen in

conjunction with altered muscovite or feldspar (Figure 5.16) or as clusters within intergranular pore spaces (Figure 5.15). Kaolinite becomes thermodynamically unstable at temperatures exceeding 90°C and can form either illite or recrystallize to dickite depending on availability of potassium and ambient temperatures. Dickite has the same chemical composition as kaolinite however appears as slightly thicker crystals (different crystal structure). This is difficult to depict using bulk XRD-analysis and for more accurate results would require a clay fraction analysis. SEM images showing pore-filling kaolinite are commonly observed throughout Facies 1 through 4 (Figure 5.15: Left). When zoomed in (Figure 5.15: Right), the cluster of kaolinite illustrates thicker crystals of the same chemical composition alongside finer grains, possibly indicating a thermodynamic transformation of kaolinite into dickite.
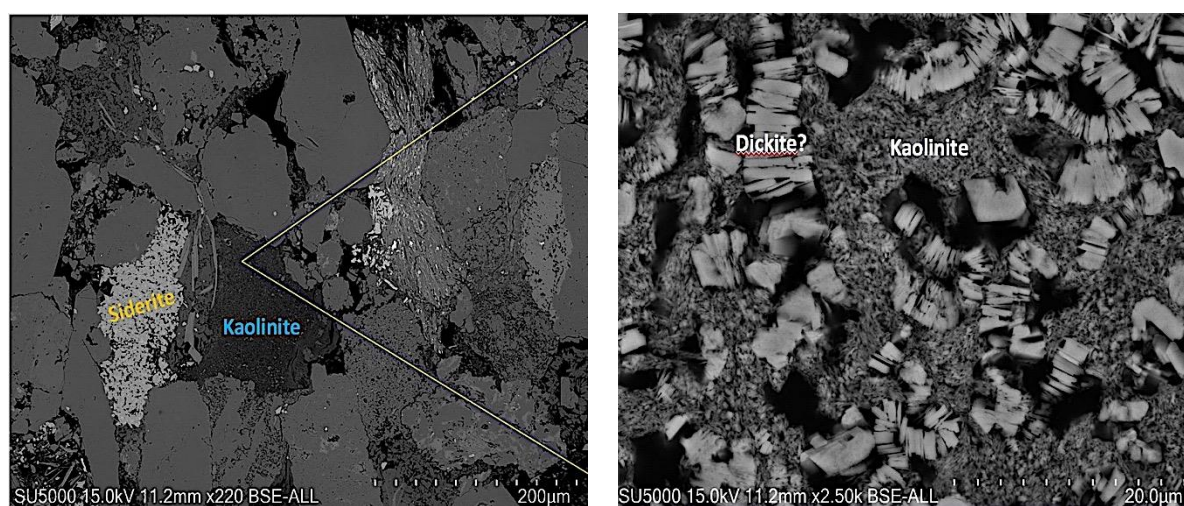
Figure 5.15: (Left) SEM image depicting pore filling kaolinite booklets. (Right) When zoomed in (20μm), thicker structures are observed possibly indicating a thermodynamic change of kaolinite into dickite (sample A17, Facies 4).

A B C
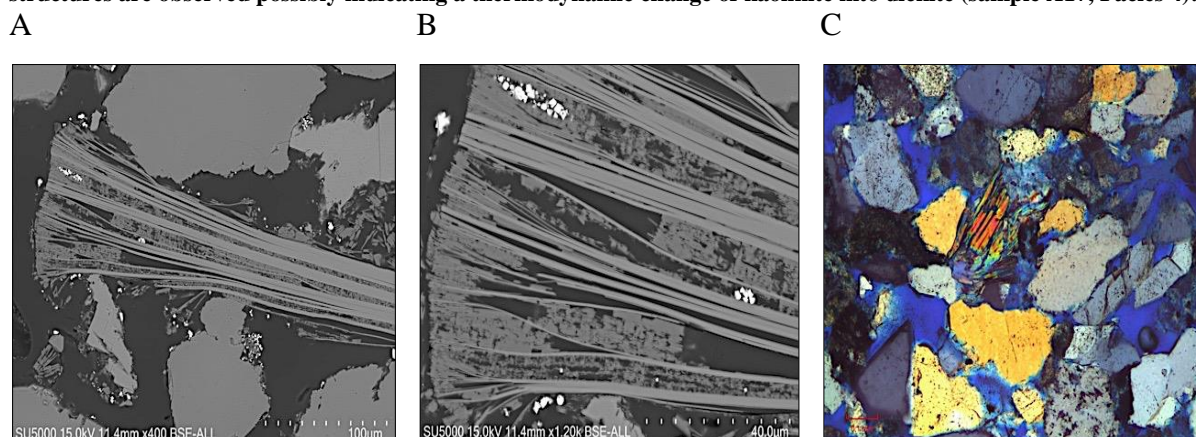
Figure 5.16: (A) SEM image showing booklets of kaolinite replacing the original muscovite grain (sample B14, Facies 6) (B) enlargement of left image (40μm). (C) Optical microscopic image using plane polarized light also showing kaolinite replacing original muscovite grain (sample A17, Facies 4).
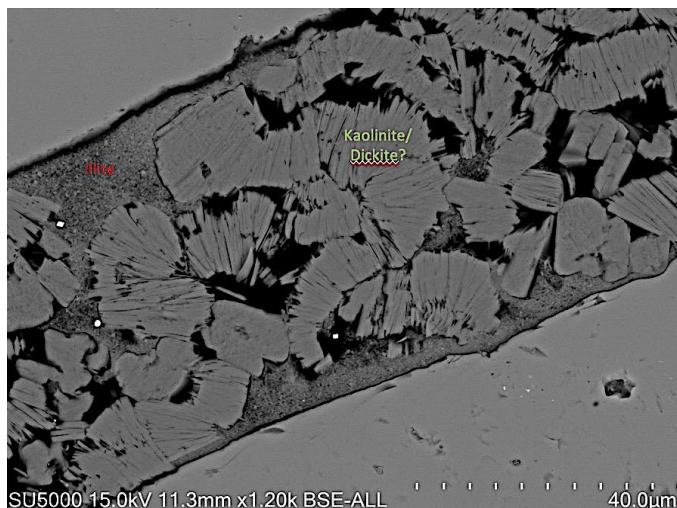
Figure 5.17: Pore filling illite and kaolinite/dickite (sample A17, Facies 4).
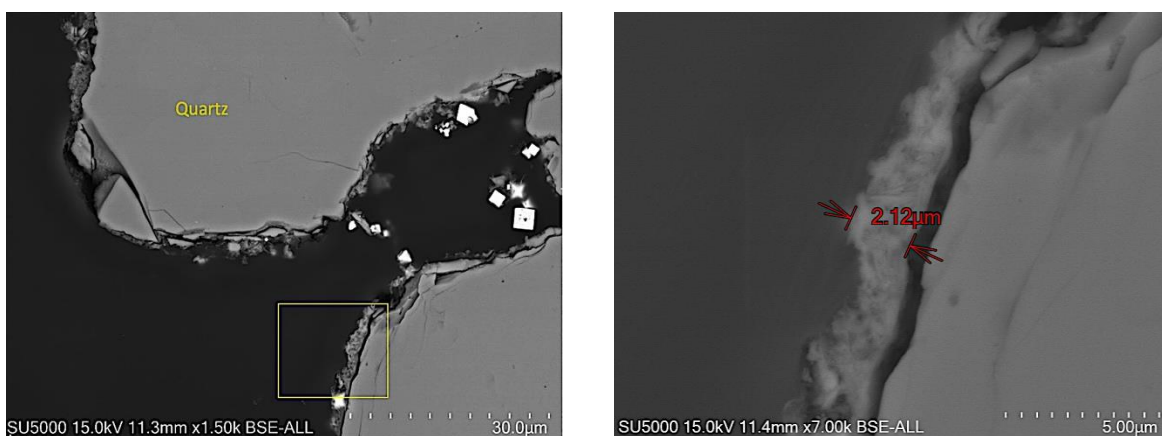
Figure 5.18: (Left) SEM backscattered electron image showing grain lining illite. (Right) enlargement showing illite lining thickness (2.12μm) (sample B14, Facies 6).
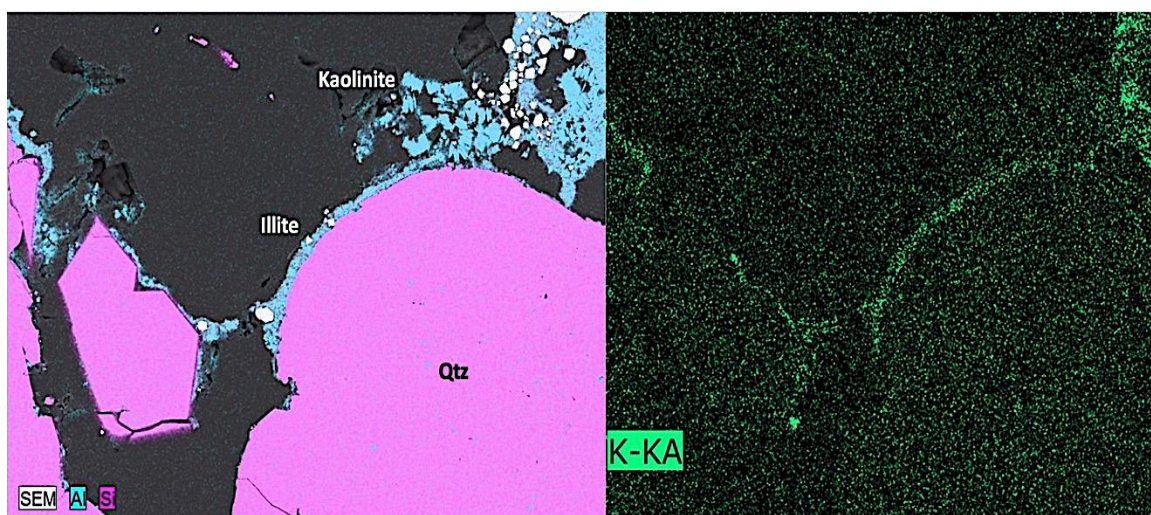
Figure 5.19: (Left) SEM backscattered electron image showing illite partially lining quartz grains. Aluminium content is highlighted in blue and silica content in pink. (Right) Same image but highlighting potassium content, separating kaolinite from illite (Sample B14, Facies 6).

Illite

Bulk XRD-interpretation tools are not able to differentiate muscovite from illite so no determinate percentage is available for illite. Typically, illite is seen as a pore-filling, mineral in conjunction with kaolinite. Small fibrous textures are observed in SEM images possibly pointing to diagenetic alteration and a different precursory mineral. This is characteristically observed in Facies 1 through 4 (Figure 5.17).

Facies 6 however depicts thin coatings of grain lining illite as seen in Figure 5.18 and Figure 5.19. When observed in SEM, illite partially lines quartz grains and does not exhibit the typical fibrous textures of authigenic illite

Calcite cement

Calcite cement is clearly seen in optical microscopy as well as detected in bulk XRD-analysis. Few samples exhibit calcite cement, however when present it predominantly fills available pore space (Figure 5.20). No trend as to where it occurs is observed, Facies 2, 3 and 6 each exhibit one or two sporadically spaced samples which contain calcite cement with values ranging between 10-28%. Facies 1 and 4 however, show negligible quantities (Figure 5.22 and 5.23).
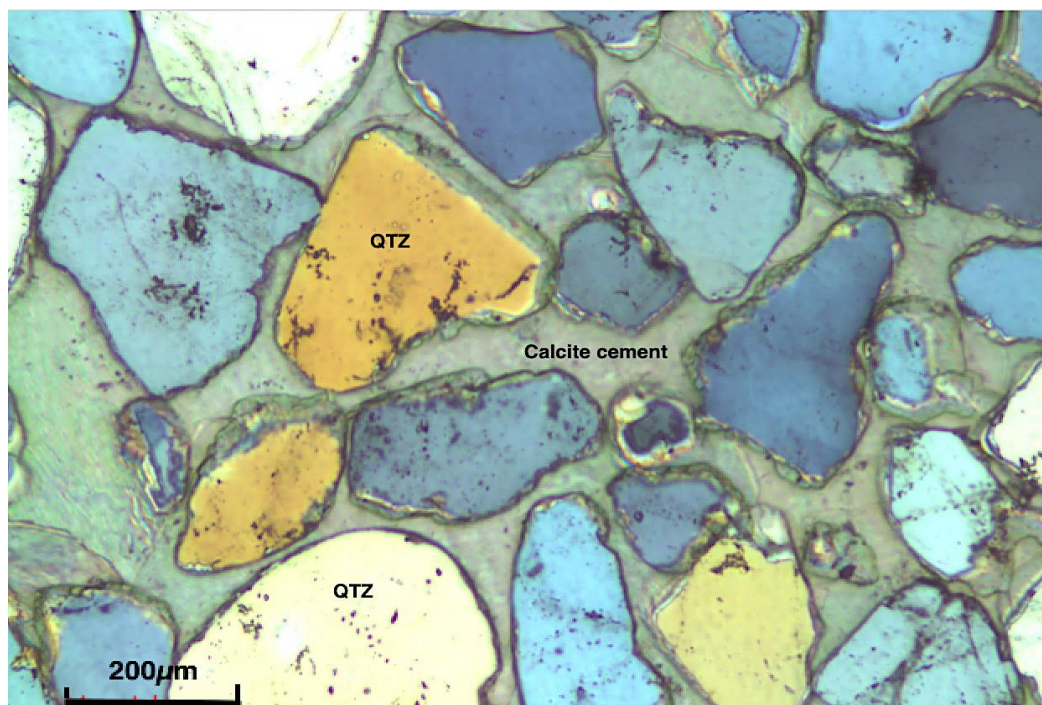
Figure 5.20: Optical microscopic image seen through plane polarized light (sample B16, Facies 6) representing entirely calcite cemented thin section.

Siderite and pyrite

Siderite is detected in trace amounts in Facies 1 through 4 (Figure 5.11). When observed in SEM it often appears in small clusters (Figure 5.21: right). Pyrite is detected in trace amounts in Facies 6, SEM images often show small spherical clusters (Figure 5.21: left).
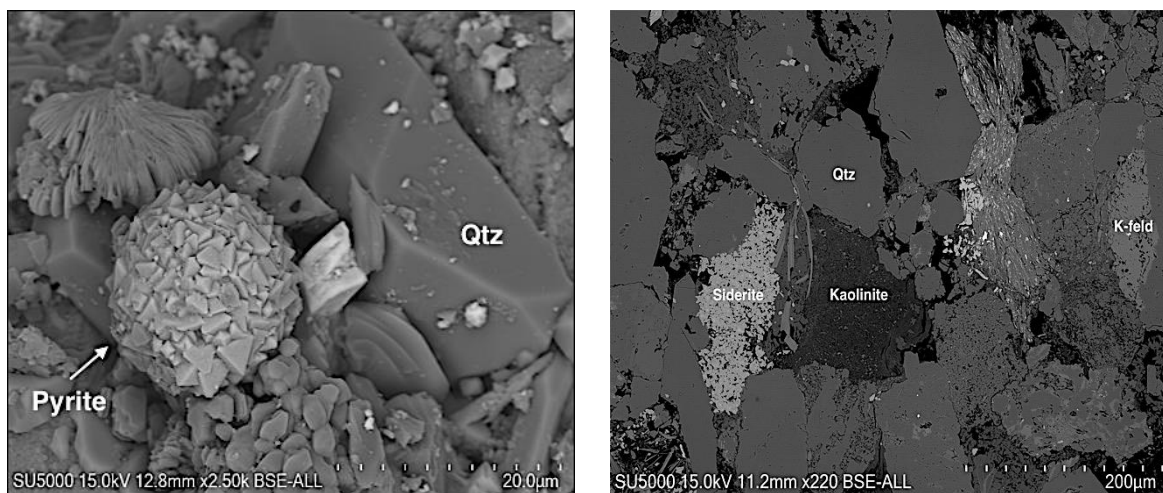
Figure 5.21: (Left) SEM image showing a spherical cluster of pyrite (Sample B14, Facies 6). (Right) Cluster of siderite crystals alongside pore-filling kaolinite (Sample A17, Facies 3).

5.2.4 Intergranular Volume

Intergranular volumes (IGV) are evaluated from point counted samples and are depicted in Figure 5.22 and 5.23. These histograms show the distribution between intergranular pore space, intergranular cements and depositional matrix in both respective wells. Intergranular cements accounted for are calcite and quartz in addition to authigenic pore filling minerals such as chlorite and kaolinite. Intergranular volumes throughout Fruholmen Formation in both wells range from 21% to 36%, representing an average of 27.61%. Stø Formation shows the same range in intergranular volumes (21-36%) however illustrating a slightly lower average of 26.60%. Calcite cemented samples throughout both formations represent the highest intergranular volumes (A16, B3, B4 and B16). Matrix predominates intergranular volumes in Fruholmen Formation representing an average of 10,03% of analysed samples and decreases markedly to an average of 1.16% in Stø Formation (Wisting Central). The majority of matrix observed in Facies 1 through 4 when point counted, is classified as dispersed allogenic clay or intercalated lamina as exemplified in Figure 5.24. Chlorite, quartz cement and kaolinite are notably smaller in volume throughout both formations.

Porosity varies between 0.25 to 16% in Fruholmen Formation in which the lowest porosity values are replaced mainly by high calcite cement or matrix. A prominent increase

in porosity is seen in Stø Formation with values ranging between 12% to 23% (disregarding B16 which is calcite cemented, showing 0.25% porosity).
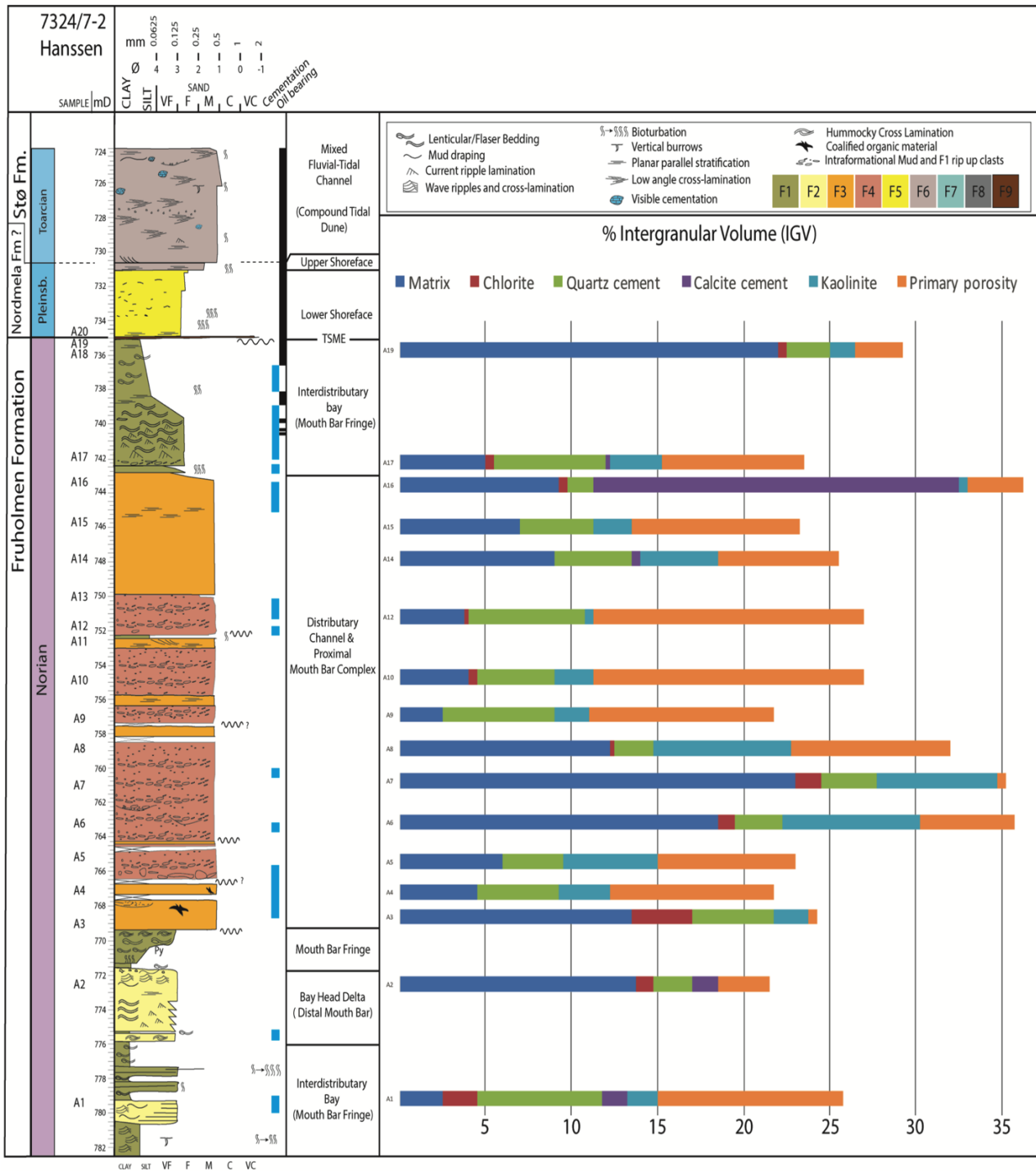
Figure 5.22: Intergranular volumes for analysed samples in Hanssen (7324/7-2). Fruholmen Formation depicting an IGV range of 21 to 36 percent.
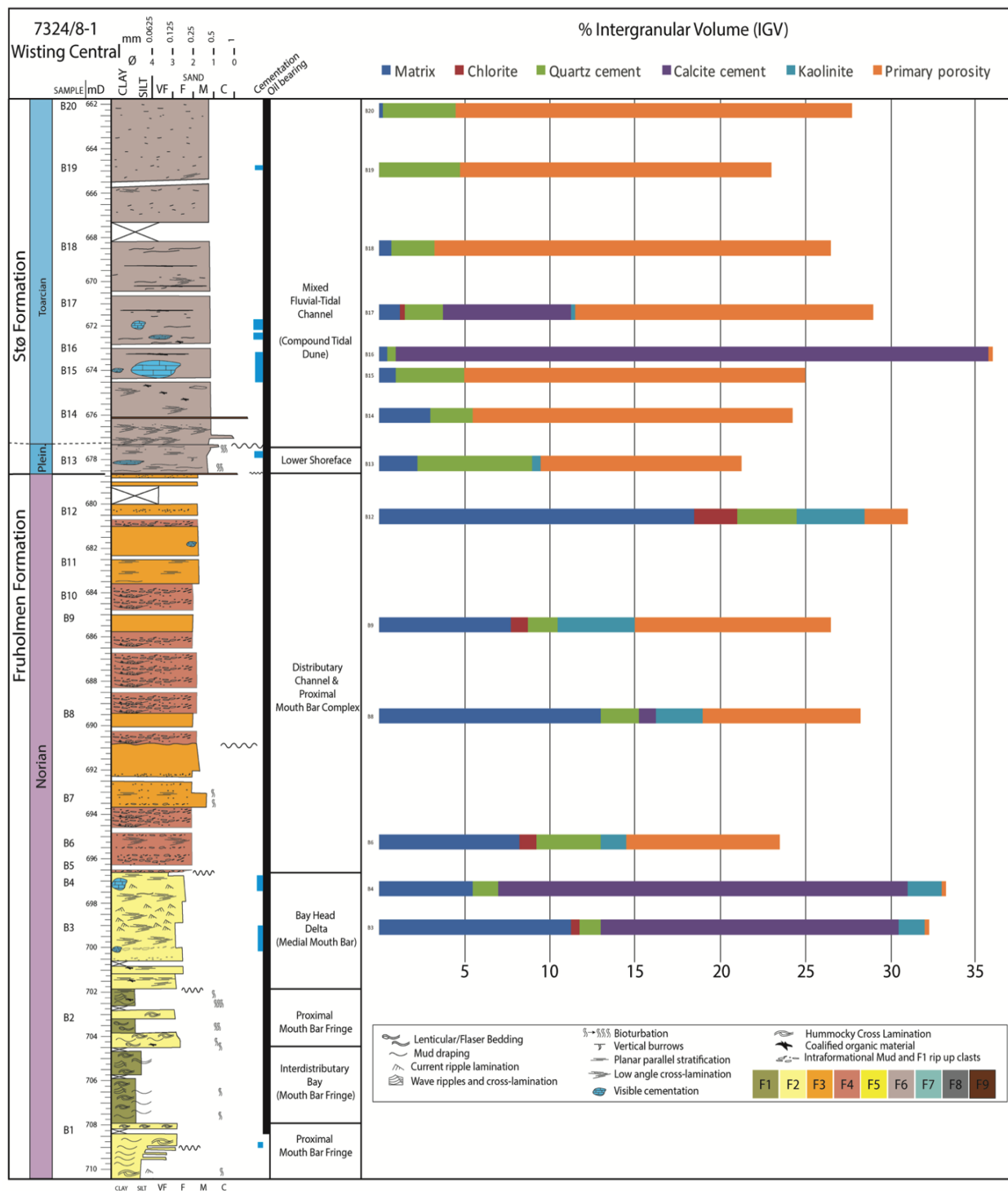
Figure 5.23: Intergranular volumes for analysed samples in Wisting Central (7324/8-1). Fruholmen Formation depicting an IGV range of 26 to 33 percent. Stø Formation illustrating an IGV range of 21 to 36 percent.
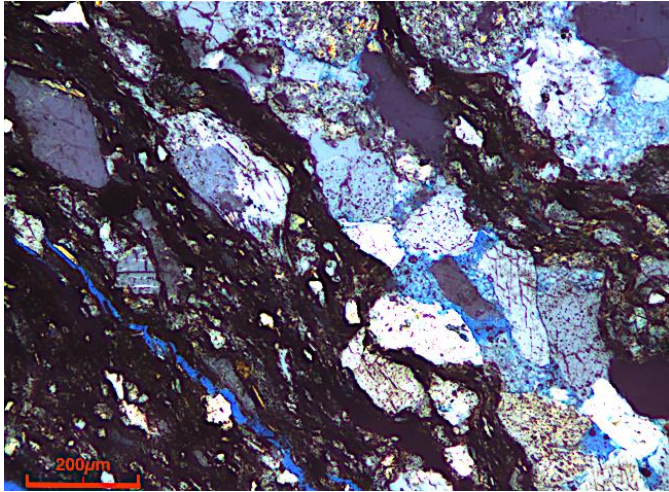
Figure 5.24: Optical microscopic image using plane polarized light showing dispersed allogenic clay and intercalated lamina (Sample A7, Facies 4).

The intergranular volume is the resultant parameter of compactional processes and cementation. When implemented into equations by Houseknecht (1987) and Paxton et al. (2002) and plotted into a diagram the effect of each subsequent process can be estimated. The compactional study conducted by Houseknecht (1987) showed sandstones of moderate- to well-sorting, yet illustrated no preferred distribution when plotted on the diagram. Therefore, all facies regardless of sorting (varying from moderate- to moderately-well) will be further used to assess cementation and compactional processes.
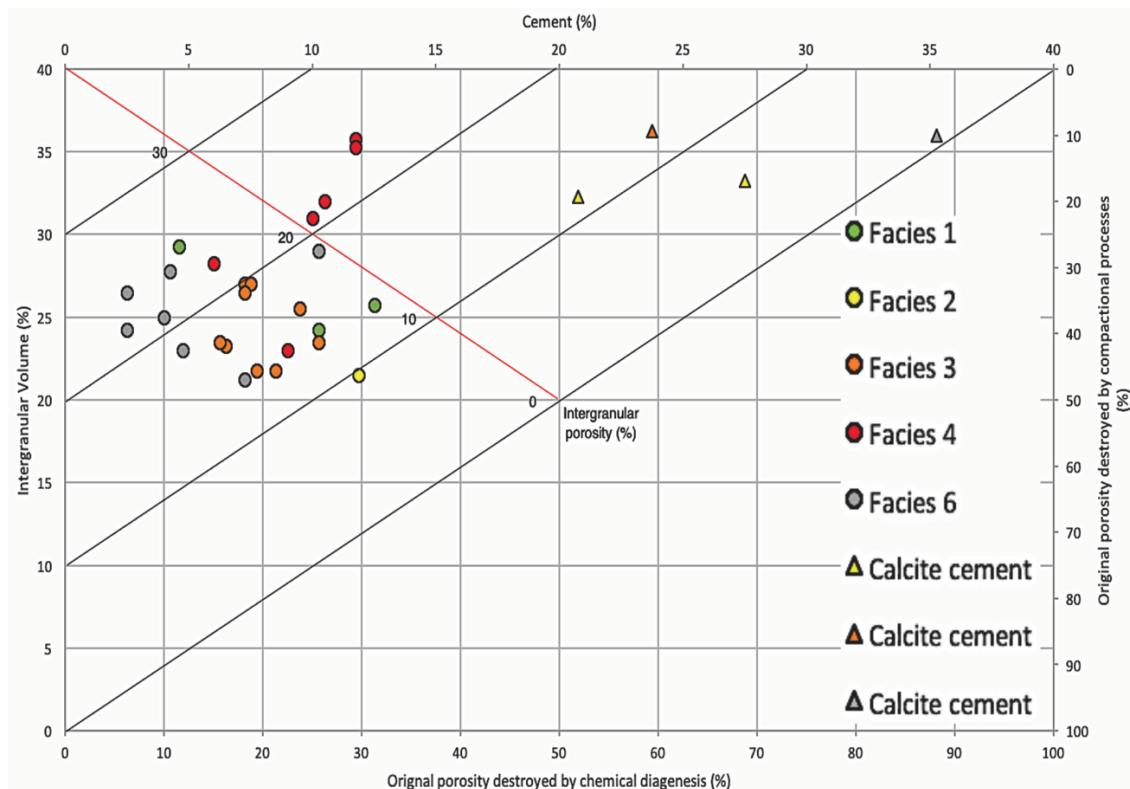
Figure 5.25: Intergranular volume vs. cement data showing compactional processes being the predominant cause of porosity loss. Circles represent moderate- to moderately well-sorted samples. Triangles represent fully or partially calcite cemented samples.

A majority of samples plot within the lower left side of the red line, indicating that the dominant pore reducing mechanism is compactional (Figure 5.25). Facies 4 shows a distinctly different trend, plotting predominantly on the upper right side of the diagram. The intergranular volumes of Facies 4 contain comparatively high percentages of depositional matrix which possibly renders this method obsolete. Houseknecht (1987) states that calculations should be based on grain-supported thin-sections, and furthermore does not include matrix when determining intergranular volume. The point counted samples of Facies 4 are grain supported however the suggestively high intergranular volumes are largely due to high matrix content. Matrix is a pore-filling component and is therefore included in all intergranular volume estimates.

The remaining samples plotting on the upper right side of the red line (triangles) illustrate cementation being the predominant pore reducing element. Average estimates for compactional processes and cementation are given in Table 5.2, differentiating between non-calcite cemented samples and predominantly calcite cemented samples. Intergranular porosity values equated by Houseknecht (1987) are represented in the diagram but further modified according to Paxton et al (2002) (Eq. 12).

Table 5.2: Average intergranular volume and porosity resulting from compactional processes and cementation.

Facies	Avg. porosity loss due to:		Avg. Intergranular Volume	Avg. Intergranular Porosity	
	Compaction	Cementation		(Houseknecht, 1987)	(Paxton et al., 2002)
1	33.96%	22.71%	26.42%	17.33%	4.67%
2	46.25%	11.88%	21.50%	16.75%	3.00%
3	38.95%	19.65%	24.42%	16.56%	10.81%
4	22.81%	24.58%	30.88%	21.04%	5.83%
6	36.88%	12.50%	25.25%	20.25%	19.04%
Calcite Cemented	12.50%	68.85%	35.00%	7.46%	1.42%

5.2.5 Porosity and Permeability

Porosity and permeability are also evaluated using core plug data provided by Petrobank (Figure 5.26). Values are selected within as close proximity as possible to samples utilzed in this thesis in order to get representative and comparitive results.

Both Hanssen (7324/7-2) and Wisting Central (7324/8-1) show relatively scattered results with regard to cut off values stipulated by Tissot & Welte (1984). Hanssen provides a number of samples from Facies 3 and 4 showing very good horizontal porosity in addition to good horizontal permeability. However, Facies 3 and 4 also show values ranging from fair
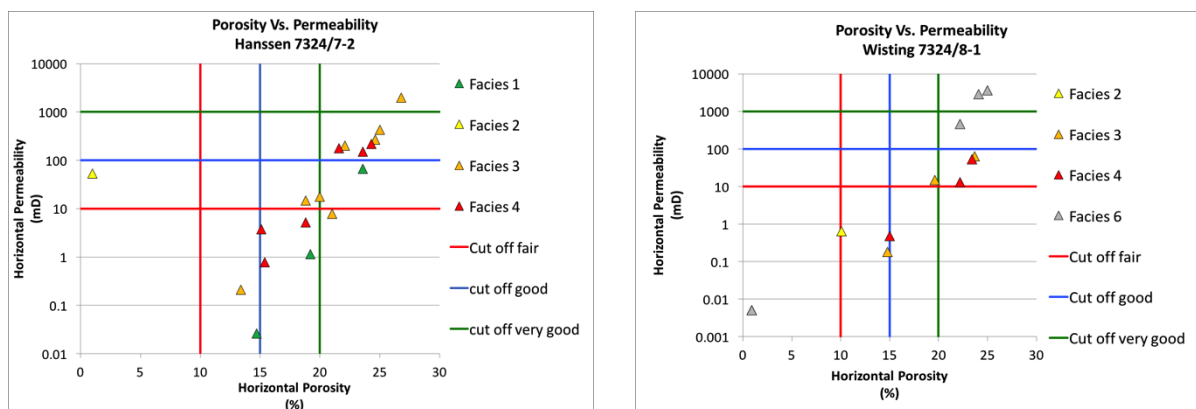
Figure 5.26: Horizontal porosity and permeability distribution in both respective well. Scattered results with no general trends are seen between facies in Fruholmen Formation. Facies 6 (Wisting Central) illustrates 'very good' horizontal porosity and 'good' to 'very good' horizontal permeability with the exception of one outlying sample. Cut off values are stipulated by Tissot & Welte (1984).

to good horizontal porosity in addition to horizontal permeability values falling below the fair horizontal cutt-off line, thus leading to no observable trend between individual facies.

Generally, porosity values are illustratively higher than permeability values. Samples illustrating poor permeability typically comprise relatively higher matrix and/or calcite cement.

Similar scattered results are seen in Wisting Central. Several tested samples from Petrobank show 'no measurable data', meaning not all samples could be processed and graphed. With regard to available sample data, Facies 6 is duly noted as exhibiting very good horizontal porosity and good to very good horizontal permeability. These results can be related back to the intergranular volume in which Stø Formation shows good porosity, small amounts of authigenic minerals and negligible matrix.

5.2.6 Grain Size and Sorting

Cumulative grain size distribution plots for Facies 1, 2, 3, 4 and 6 are presented in Figure 5.27. The inclination of each curve represents the degree to which each sample is sorted. However, in order to show clear, objective results, histograms illustrating the standard deviation and sorting according to Folk (1974) are additionally presented. Generally, each facies plots as moderate to moderately well sorted, fine- to very fine sand with the exception of a few outlying values
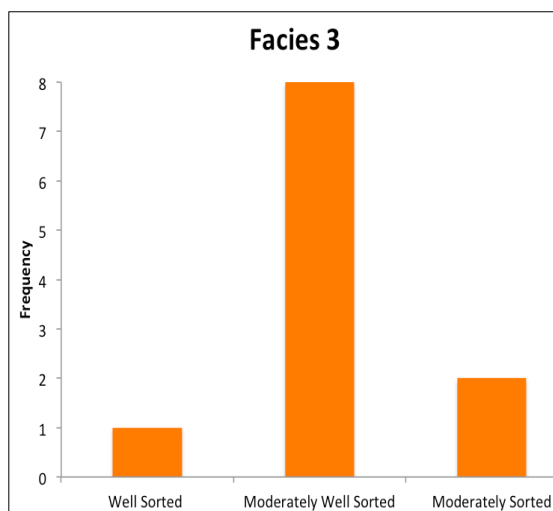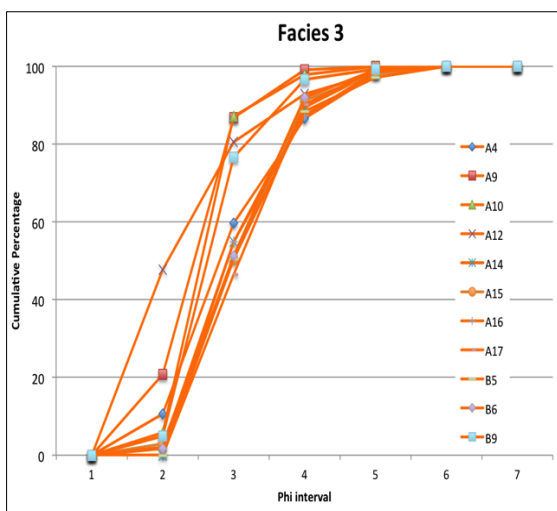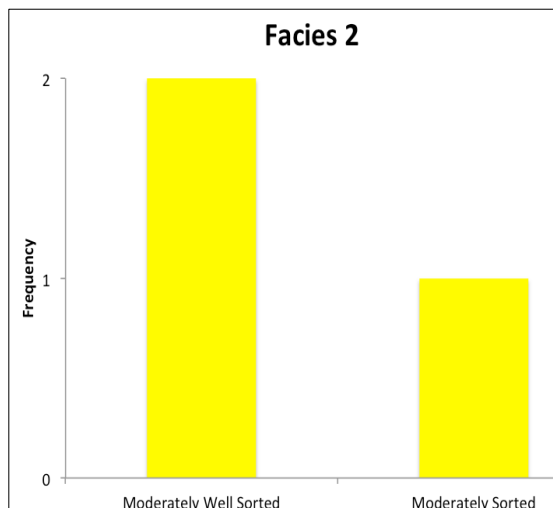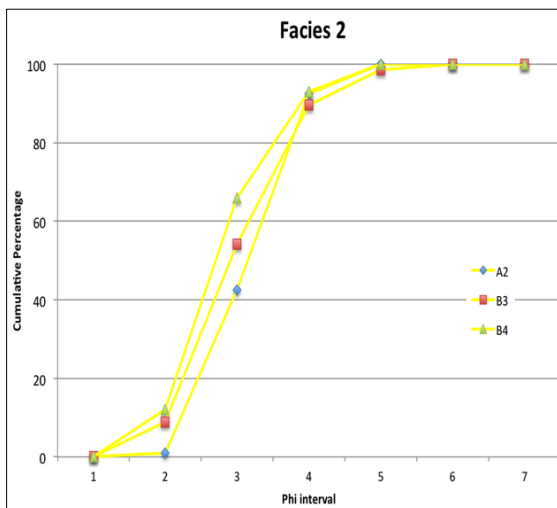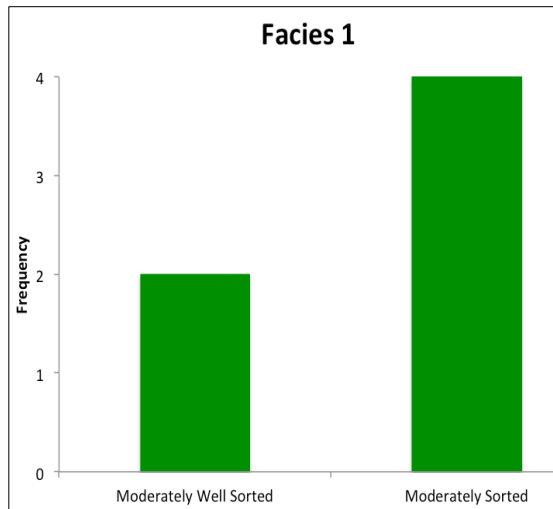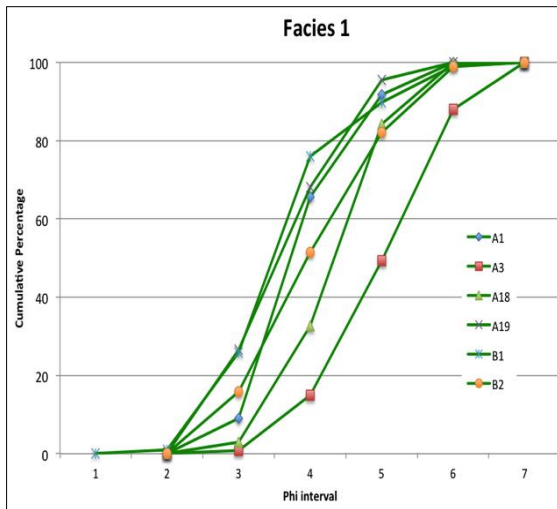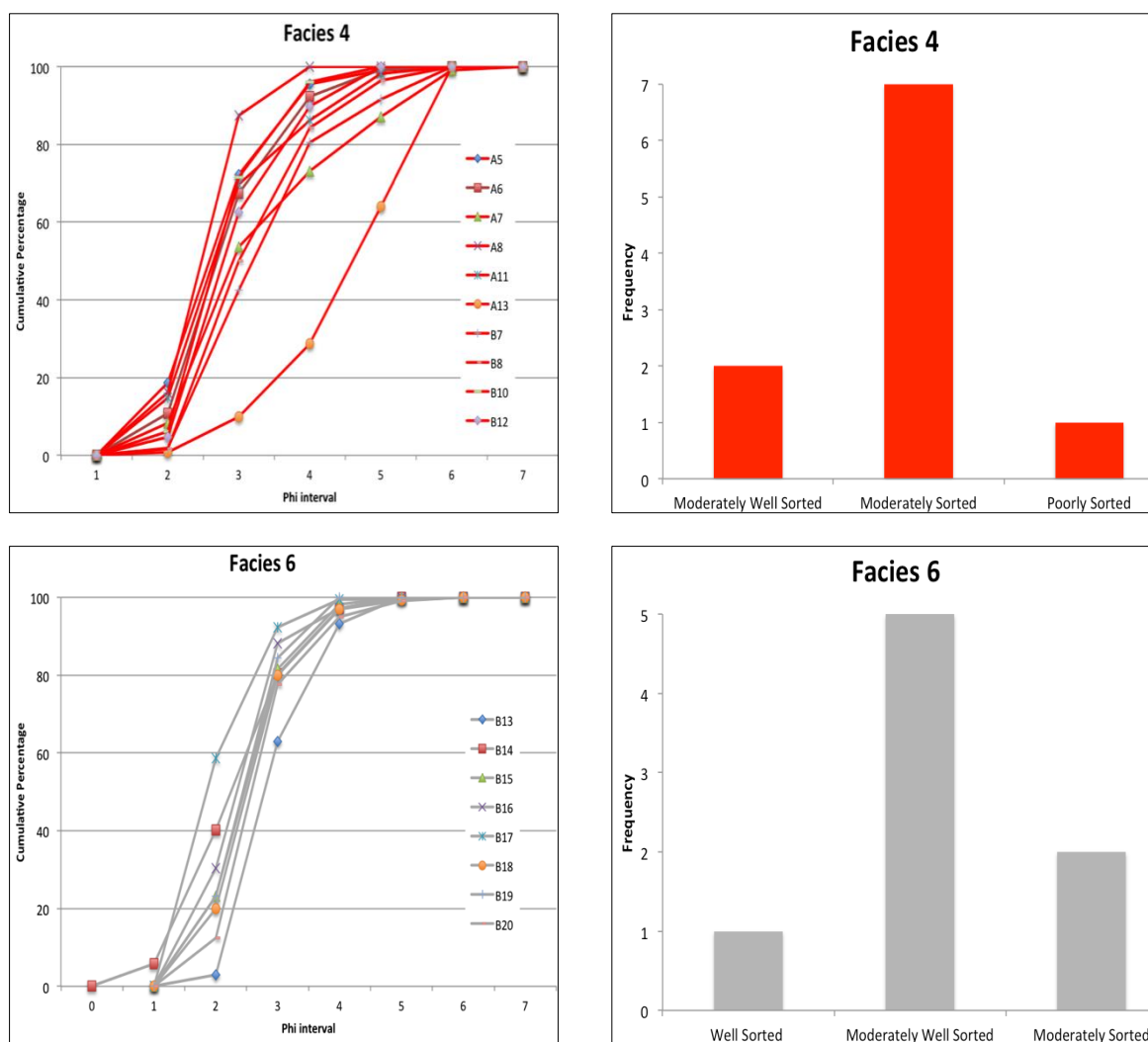
Figure 5.27: Cumulative grain size distribution plots for each analysed facies. Sorting is represented by the inclination of each curve and additionally depicted in histograms for clear evaluations. Sorting is defined using the standard deviation of grain sizes and further characterized according to Folk (1974).

Facies 1 depicts a normally distributed curve exhibiting predominantly a sharp increase between phi-ranges 3 to 4, characterizing an abundance of very fine sand. Outlying samples (A3 and A18) show a predominance of finer grain-fractions within the range of coarse silt. Facies 1 shows moderate- to moderately-well sorting.

Facies 2 represents a positively skewed curve in which all three samples show a sharp increase between phi-ranges 2 to 3, characterizing fine sand. Similar to Facies 1, samples show moderate- to moderately-well sorting.

Facies 3 show comparable characteristics to Facies 2, illustrating a positively skewed curve. The prevailing grain size is difficult to determine from illustrated diagrams, however a sharp increase between phi-ranges 2 to 4 suggests an overall dominant grain fraction of fine to very fine sand. Sorting is predominantly moderately-well.

Facies 4 illustrates a wider spread of grain sizes however the majority of samples depict a sharp increase between phi-ranges 2 to 3, indicating a predominance of fine sand. Sample A13 does not follow the general trend of Facies 4 and exemplifies a predominance of finer grain fractions. Moderate sorting is largely dominant.

Facies 6 shows a positively skewed curve in which samples exhibit a sharp increase between phi-ranges 1 to 3 characterizing an abundance of moderately-well sorted, fine- to medium grained sand.

5.2.7 Grain Contacts

Contacts are at times difficult to establish due to quartz cementation masking the original detrital grains. The quartz cement welds grains together typically causing an overestimation of long or sutured contacts. The ability to ascertain quartz cement is difficult through microscopic analysis, which subsequently may lead to skewed results. Grain contacts are only assessed in sand-prone samples as matrix-rich samples inhibit the ability to observe detrital grain contacts.

Figure 5.28 shows that long grain contacts are the predominant feature throughout all facies, subsequently followed by concave-convex contacts. Tangential contacts, sutured contacts and floating grains are less frequently noted throughout successive facies. Results indicate that mechanical compaction has affected a majority of sediments, consequently causing a reduction in the bulk volume. Samples containing mainly tangential or floating grains are typically seen as fully calcite cemented.
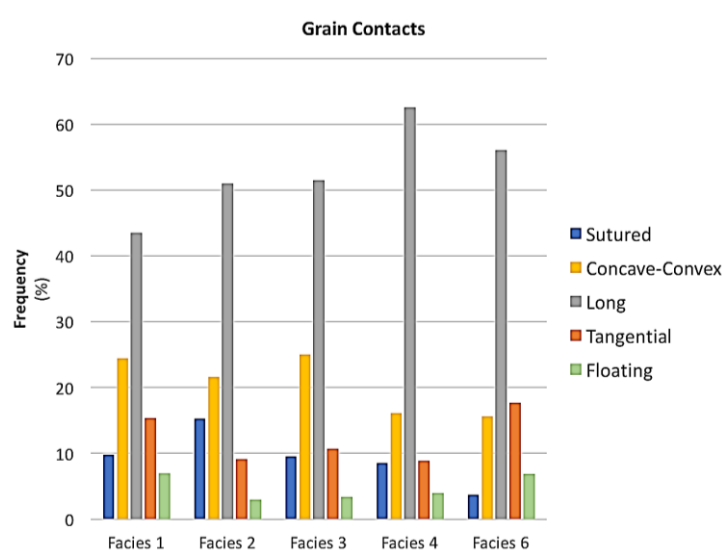
Figure 5.28: Grain contact analysis showing distribution between floating, tangential, concave-convex, sutured and long grain contacts.
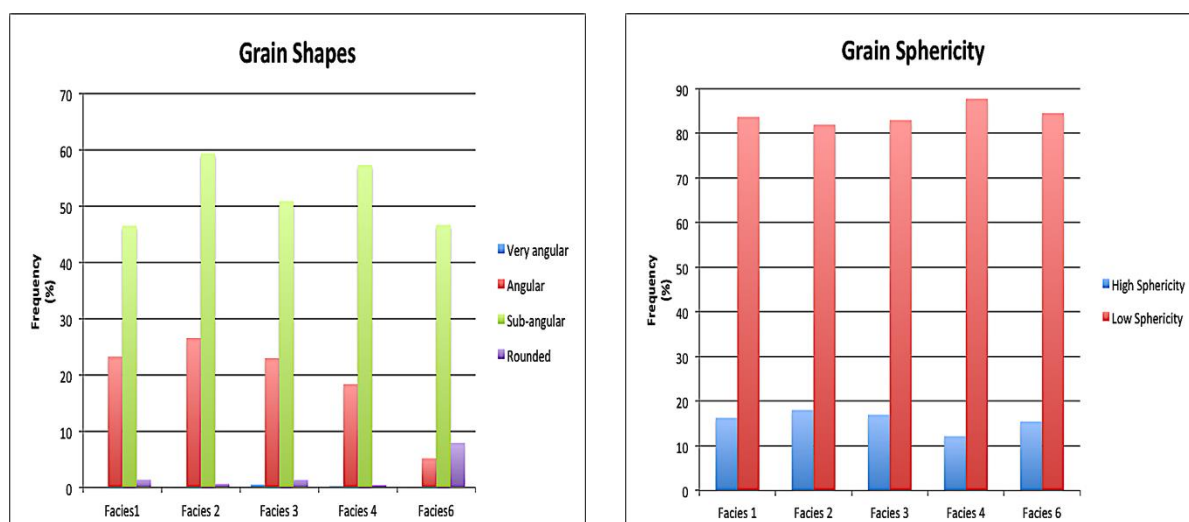
Figure 5.29: Grain shape analysis showing a prevalence of sub-angular, low spherical grains throughout all facies.

5.2.8 Grain Shapes

Similar difficulties as previously noted are encountered when determining grain shapes. Quartz cement distorts many of the original grains possibly leading to biased results. According to Figure 5.29 a prevalence of sub-angular, low spherical grain shapes are predominantly observed throughout all samples. The incidence of low spherical grains contra high spherical is prevailing.

In order to determine whether there is any relation between intergranular volume, grain size, sorting and amount of matrix, three additional diagrams are further illustrated (Figure 5.30). Empirical studies (Figure 3.6) suggest that coarser-grained sands compact more readily than finer-grained sands. Heterolithic sandstones containing an abundance of matrix have also shown a higher loss of porosity due to ductile deformation and reduced friction between grains. Sandstones consisting primarily of rigid grains tend to reorganize into a close packed geometry with a theoretical intergranular porosity of 26% which is subsequently reduced during chemical compaction.
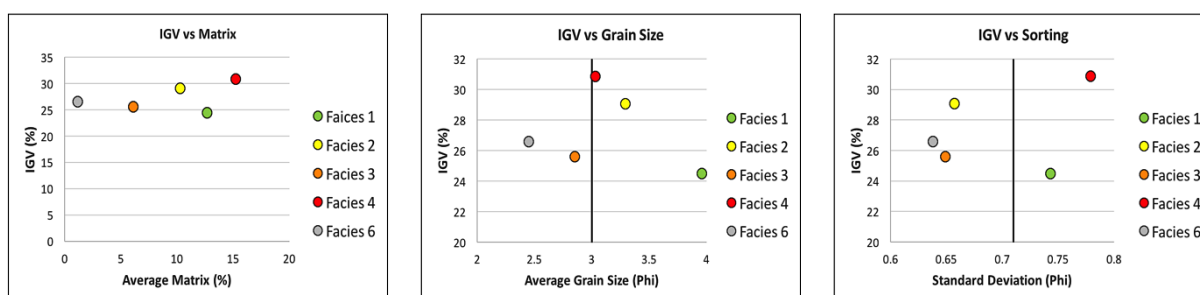
Figure 5.30: Intergranular volumes vs matrix, grain size and sorting.

No explicit trend is seen between IGV and matrix content. Facies 4 contains the highest percentage of matrix yet yields the highest IGV. Facies 6 resembles the empirically tested data of clean, well-sorted sandstones consisting largely of rigid grains, resulting in a close packed geometry and an IGV of approximately 26%. Facies 1, 2 and 3 illustrate intergranular volumes ranging from 24-29% and intermediate matrix values ranging between 6-12%.

With the exception of Facies 1, a slight trend can be assumed between grain size and IGV. Finer sand fractions (Facies 2 and 4) show a higher IGV than the coarser grained sand fractions (Facies 3 and 6). Facies 1 illustrates the finest grain size according to Wentworth's Phi scale yet exhibits the lowest IGV values resulting in an anomaly in trending data.

No trend is observed between IGV and sorting. Higher sorting degrees are expected to yield higher IGV values. Facies 1 and 4 both illustrate moderate sorting and exhibit the lowest (Facies 1) and the highest (Facies 4) intergranular volumes. Facies 2, 3 and 6 depict moderately well sorting and show intermediate intergranular volumes.

5.3 Petrophysical Analyses

Petrophysical analyses are conducted using well log data from both wells in order to assess porosity, evaluate depositional environments and estimate to which depth sediments have been buried. The geothermal gradient is in turn calculated using present day bottom hole temperatures in order to determine which temperature sediments endured at maximum burial. These parameters are vital when characterizing a reservoir as porosity and permeability are largely dictated by mechanical and chemical compaction. Mechanical compaction is directly related to effective stress (burial) and causes a reduction in bulk volume (closer packing of framework grains). Chemical compaction is temperature induced and is initiated at approximately 70ºC causing mechanical compaction to cease. In order to estimate the temperature that sediments have been exposed to, the maximum burial depth is assessed using well log data for both respective wells along with empirically tested data by Mondol (2009).

The gamma-ray log, and neutron-porosity logs are displayed for logged intervals in order to compare petrophysical data with interpreted petrographical results.

The gamma ray-, sonic-, neutron- and density logs are in turn displayed for entire cored sections with the intent of determining the transition from mechanical to chemical compaction as a function of burial depth. Formation data is provided by NPD Fact Pages and illustrated in different colours (Figure 5.32).

5.3.1 Gamma Ray Logs

The gamma ray logs for both wells illustrate a general cleaning upwards trend from Fruholmen Formation to Stø Formation, representing a progressive decrease in clay mineral content (Figure 5.31). This coincides well with petrographic results indicating that Stø Formation was deposited in a high-energy shallow marine to fluvial-tidal environment. Point count results show a mature, quartz-rich sandstone, consisting of very little depositional matrix.

Fruholmen Formation illustrates a varied gamma ray response, indicating a mixed energy depositional regime. Facies 1 is characterized by a predominantly high gamma ray response essentially portraying a clay-rich lithology which corresponds well with petrographic results. Suggested depositional environment for Facies 1 is within a mouth bar fringe zone, receiving mostly suspension deposits.

Facies 2, 3 and 4 illustrate varying gamma ray responses, however several interstitial bell-shaped trends can be inferred. Facies 3 generally illustrates a lower gamma ray response than Facies 4 representing a cleaner sandstone. Wisting (7324/8-1) shows several 'dirtying-up' bell shaped trends illustrated by a progressive increase in the gamma ray response between Facies 3 and 4. This signifies a more clay-rich lithology in Facies 4 indicating a decrease in depositional energy which according to Myers & Milton (1996) can be related to meandering or tidal channel deposits. Facies 3 and 4 are respectively interpreted as part of a mouth bar and distributary channel environment and the increase in gamma ray response seen in Facies 4 is likely caused by significant amounts of mud-rich rip-up clasts as inferred by sedimentological core logging. The rip- up clasts possibly testifies to an increase in depositional energy allowing for scouring and/or bank collapse.
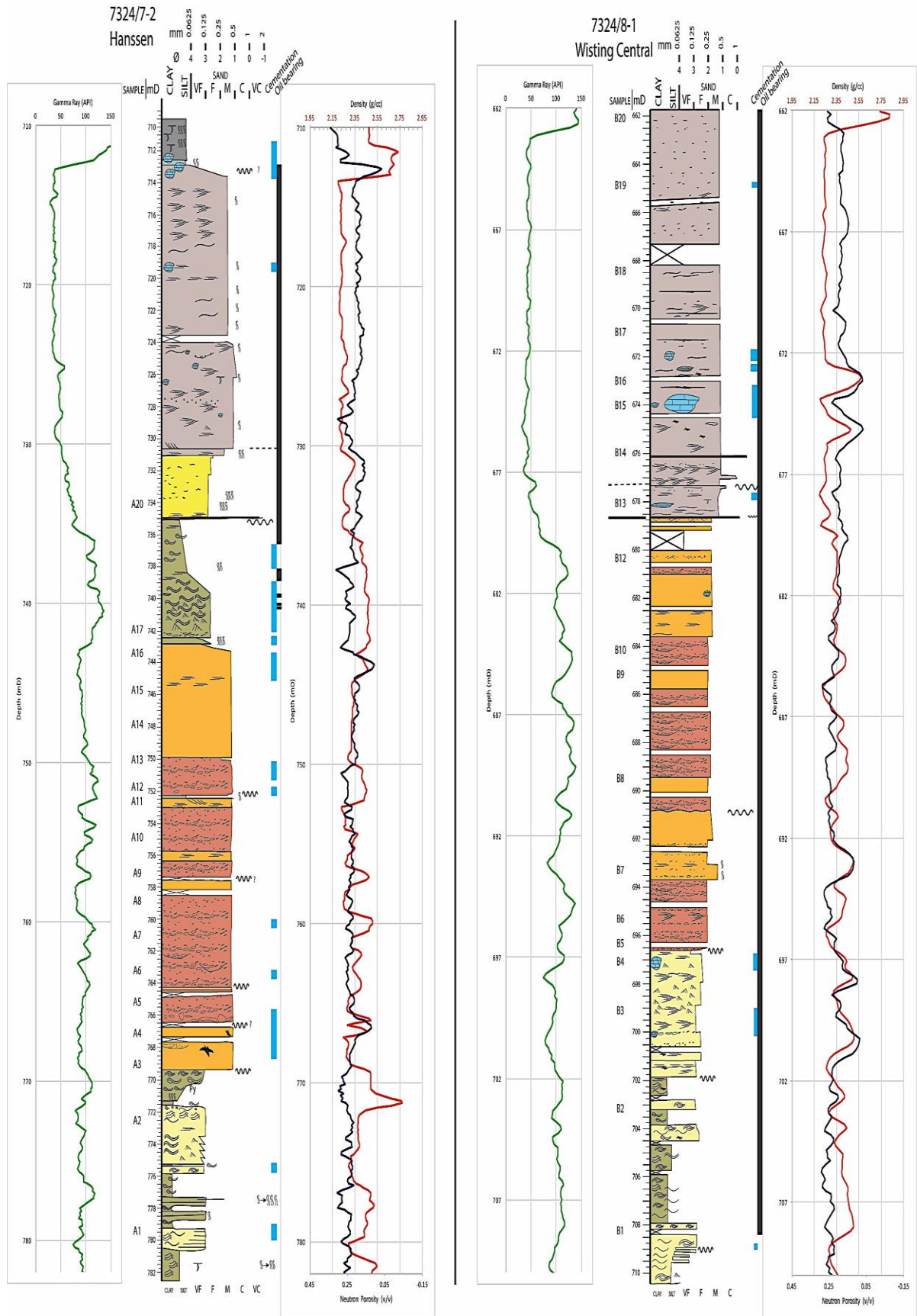
Figure 5.31: Gamma ray log (green) illustrating a general cleaning-upwards trend from Fruholmen Formation to Stø Formation. Neutron porosity (black)-density (red) cross-plots alongside logged succession depicting oil filled porosity in Stø Formation whereas Fruholmen Formation shows comparatively reduced parameters, indicating mainly water filled or poor porosity.

5.3.2 Neutron and Porosity Logs

Neutron porosity and density logs are cross-plotted in order to depict porosity and hydrocarbon index throughout logged intervals (Figure 5.31). Neutron porosity and density cross-plots have to be used with caution, as explained in section 4.3.5 neutron logs can lead to both over- and underestimation of porosity. Therefore, these cross-plots are illustrated and used in conjunction with petrographical data to confirm or discuss any disparities.

Stø Formation accordingly shows oil filled porosity and corresponds well with observed petrographical data. Fruholmen Formation shows a varied response but significantly reduced parameters when compared to Stø Formation. Facies 1, 2 and 4 generally illustrate reduced porosity which fits well with petrographical data showing high depositional matrix, cemented intervals and mud-rich rip-up clasts. Facies 3 is interpreted as a moderately well-sorted, generally structureless sandstone and shows comparatively average porosity filled with interstitial water.

5.3.3 Sonic Logs

The sonic log shows a general increasing trend in Vp as a function of depth in both wells (Figure 5.32). The transition from mechanical to chemical compaction is based on Vp-depth trends and is depicted by an abrupt increase in Vp for the same given lithology. This break is however not clearly delineated in either well. A slight increase in the Vp-trend line is however noted at 690m MD in Hanssen and 640m MD in Wisting Central, depicted by simplified trend-lines (Figure 5.32). When subsequently correlated to the gamma ray log the increase in Vp is seemingly not caused by a change in lithology. These depths will therefore be used as an indication as to where mechanical compaction transitions into chemical compaction (marked by horizontal red lines). Mechanical compaction is seen in the upper part of both respective wells ranging from 520-690m in Hanssen and 495-640m in Wisting Central.

Anomalously high values are observed in e.g. Knurr Formation reaching Vp-values of 3600m/s (Hanssen) and up to 4600m/s (Wisting Central). Correspondingly low Vp-values are seen in e.g. Hekkingen Formation, showing Vp-values deviating from the general trend. These low Vp-readings are respectively seen as low bulk densities and high gamma readings. In reference to NPD Fact Pages the anomalously high Vp-readings in Knurr Formation are caused by carbonate cemented intervals whereas the anomalously low values are induced by organic rich sediments found in Hekkingen Formation.
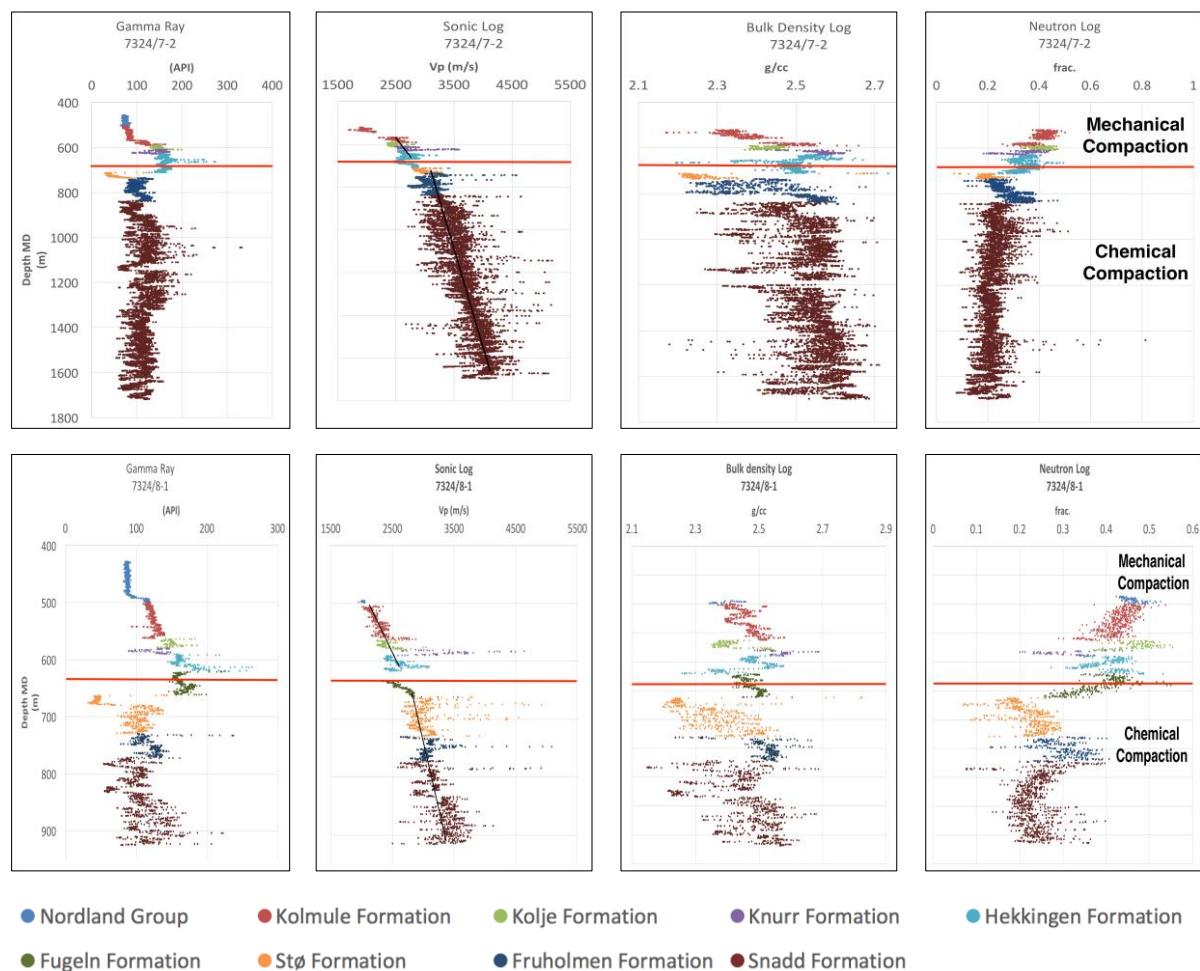
Figure 5.32: Compaction trends observed in Hanssen (7324/7-2) and Wisting (7324/8-1). Red horizontal line illustrates the interpreted transition zone from mechanical to chemical compaction.

The neutron logs show an inverse relationship to the corresponding bulk density logs and registers hydrogen content contained in pore fluids (water or hydrocarbons) or hydrogen bound within mineral structures (e.g. smectite). Both wells depict an overall decrease in neutron porosity, with the exception of Stø and Fruholmen Formations which deviate from the general trend and indicate a successive increase in neutron porosity.

The transition from mechanical to chemical compaction seen in Figure 5.32 places Stø and Fruholmen Formations within the chemical compaction regime. However, the temperature at current burial depth is not high enough to represent the onset of chemical compaction (Table 5.3) thus placing both wells at preceding deeper burial.

5.3.4 Uplift Estimation

The geothermal gradient is calculated based on present day bottom hole temperature readings.

Hanssen: $G_g = \frac{51°-2°}{1679m-417,5m} * 1000m = 38,8°C\ km^{-1}$

Wisting Central: $G_g = \frac{29°-2°}{905m-398m} * 1000m = 53,0°C\ km^{-1}$

In order to estimate maximum burial and subsequent uplift, empirically tested compaction curves published by Mondol (2009) are used. A 50:50 kaolinite-silt curve is implemented as this is assumed to best fit the shale lithology observed. Shale data is segregated based on cut-off values of 100 API in Hanssen and 110 API in Wisting and further used to estimate the uplift in both respective wells. The shale data is initially plotted at its current depth (Figure 5.33: blue) and subsequently adjusted (Figure 5.33: green) in order to best fit the 50:50 kaolinite-silt curve (Figure 5.33: solid red line). Outlying samples in Wisting can possibly be explained by a differing shale lithology causing sediments to compact more readily. Maximum burial depth and associated temperatures of both respective wells are further calculated based on estimated uplift and presented in Table 5.3.
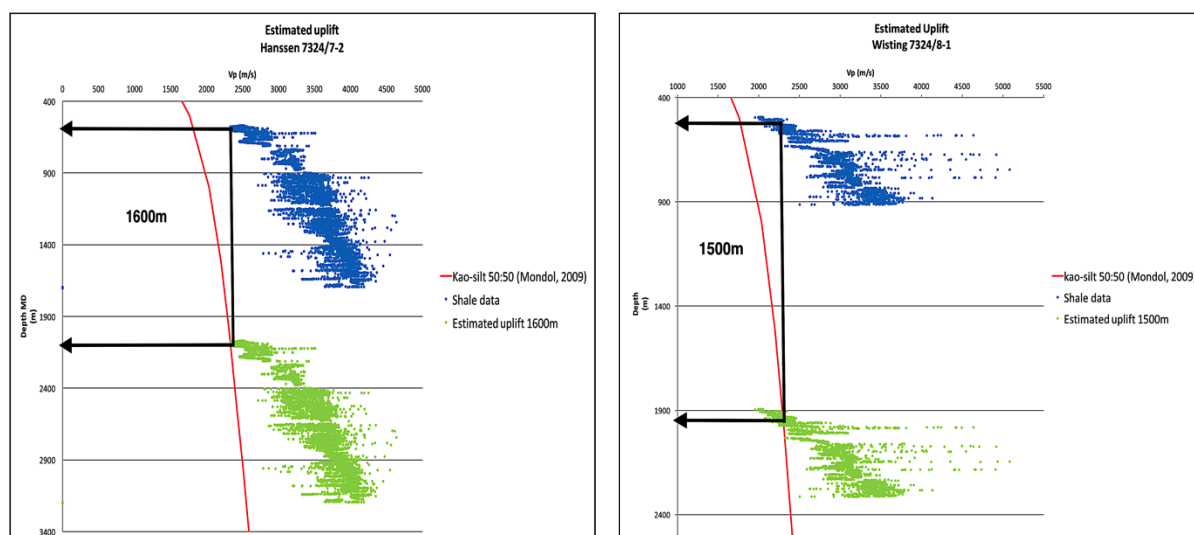
Figure 5.33: Exhumation estimates based on empirically tested data (kao-silt 50:50) by Mondol (2009). Hanssen (7324/7-2) shows an approximated uplift of 1600m whereas Wisting Central (7324/8-1) depicts a slightly lower estimate of 1500m.

Table 5.3: Temperature interval at present and estimated maximum burial depths of Stø and Fruholmen Formations Temperature calculations are based on bottom hole temperature of both respective wells.

Well	Present depth of cored wells	Temperature interval at present burial depth	Estimated uplift	Maximum burial depth of cored interval	Temperature interval at maximum burial depth
Hanssen 7324/7-2	710-782m MD	27.55-30.34°C	1600m	2310-2382m MD	89.6-92.4 °C
Wisting 7324/8-1	662-710m MD	35.09-37.63 °C	1500m	2162-2210m MD	114.6—117.1 °C

6. Discussion

6.1 Introduction

The objective of this thesis is to characterize the reservoir potential in Fruholmen and Stø Formations through petrographic and petrophysical analyses of 2 wells (Hanssen 7324/7-2 and Wisting Central 7324/8-1) located in the southwestern Barents Sea. Reservoir quality is often defined by its porosity and permeability which in turn are functions of provenance, depositional environment, climate and diagenesis. This chapter intends to discuss the obtained results from sedimentological, petrographic and petrophysical analyses so as to gain an understanding of the geological evolution that has led to current observations. Results are discussed in a chronological order from provenance and depositional environments to burial history and subsequent uplift and will be further assessed with regard to published literature. Concluding remarks on influential factors affecting the reservoir quality of each analysed facies will be evaluated at the end.

6.2 Climate, Provenance and Depositional Environment

Primary influences on reservoir quality are paleoclimate, provenance and depositional environment. A marked change is seen between Facies 1 through 4 (Fruholmen Formation) and Facies 6 (Stø Formation), whereby two different facies associations are inferred (Figure 5.3). This change is mainly reflected in mineralogical framework constituents and matrix content. Fruholmen Formation is categorized as a subarkosic arenite showing moderate amounts of feldspar (mainly plagioclase) and matrix (allogenic clay). Stø Formation is classified as a quartz arenite, showing little feldspar and negligible amounts of matrix. The lack of feldspars and matrix in Stø Formation suggests a more mineralogically mature sandstone. Similar changes in composition have been observed in previously published studies by e.g. Ryseth (2014) who examined more explicitly, differences between Snadd Formation (Late Carnian to Early Norian) and Tubåen Formation (Late Rhaetian to Sinemurian). This regional change may be caused by one or several coinciding factors such as climatic changes, changes in palaeodrainage directions, changes in basin subsidence rates (Bergan & Knarud, 1993) or as suggested by Ryseth (2014), "A temporal change in the composition of erosion products from the east (Uralides) to a more quartz-rich composition in the Late Triassic to Early Jurassic". Notably, a significant hiatus exists between Fruholmen and Stø Formations where Tubåen is completely absent and Nordmela appears as a condensed succession in Hanssen (7324/7-2). This hiatus represents millions of missing

years whereby changes in climate, depositional environment, tectonics and provenance are to be expected.

6.2.1 Climate

Climatic changes can have numerous implications on sediments. A more humid climate and higher annual precipitation will lead to larger fluvial discharge and increased capacity of rivers which will have a major impact on weathering and early diagenesis of mineral assemblages. Increased precipitation may lead to a higher ground water table which can subsequently cause an increase in meteoric water flow rate and enhanced mineral dissolution (Bergan & Knarud, 1993). Although a change in climate is inferred, it is not likely be the sole reason behind the distinct change in mineral composition and maturity seen between Fruholmen and Stø Formations.

The principle weathering reaction occurring at shallow depth due to meteoric flushing is the dissolution of feldspar and mica and precipitation of kaolinite. It can therefore be assumed that if the initial mineral assemblage of Fruholmen Formation and Stø Formation was the same, a higher percentage of leached feldspars and subsequent kaolinite precipitation is expected in Facies 6 (Stø Formation) which is not the case. Feldspars are far more infrequent and kaolinite is observed only in trace amounts. Therefore, two further scenarios are discussed. Assuming the mineral composition was initially the same, additional reworking of previously deposited sediments can be implied. Continuous leaching and reworking would remove chemically precipitated minerals such as kaolinite and potentially further reduce the amount of feldspars. This would increase the quartz to feldspar ratio and result in a more mature sandstone. Regional subsidence and vast sediment accumulations are characteristic from the Triassic period (Fruholmen Formation) (Henriksen et al, 2002; Glørstad-Clark et al., 2010). These features are significantly reduced during the Jurassic time period (Stø Formation) theoretically meaning that the influx of sediments and the rate of subsidence are in equilibrium. Aggradational stacking patterns of decimetre to metre scale trough and planer cross-stratification sets support this theory. By maintaining a fixed position of the coastline over long periods of time, extensive reworking of sediments is able to proceed.

The second scenario is a change in provenance which can cause the initial mineral assemblage to be different from the onset of weathering. When the provenance is changed it follows that drainage patterns are altered, which may further lead to reworking of previously deposited sediments along with new sediment input.

6.2.2 Provenance

Provenance studies on Svalbard have been conducted by Pozer Bue & Andresen (2015) based on zircon analyses within the Mesozoic successions. These authors concluded that three subdivisions can be made based on three different signatures. Two endmember groups are clearly distinguished and a third group displaying mixed characteristics are found on Svalbard. The first endmember is sampled from Early- to Middle Triassic Formations and show zircon ages corresponding to a western source area namely Greenland and Artic Canada. Analysed samples from the Late Triassic (equivalent to Fruholmen Formation) show a distinctly younger zircon age signature which can be associated with the Uralian orogeny in the east. Early- to Middle Jurassic sediments (equivalent to Stø Formation) display characteristics from both endmember groups but also prominent signatures from the Caledonides, indicating either a new and different source area and/or mixing of the previously described endmember groups i.e. Early- to Middle Triassic westerly source and Late Triassic easterly source. Mørk (1999) confers similar observations from a study conducted on Triassic sandstones from a vast area (ranging from the Pechora Sea and Novaya Zemlya in the southeast to the western Barents Sea and Svalbard). A distinct increase in sandstone maturity is seen on a regional scale in the Artic during the Latest Triassic to Early Jurassic, which may be related to extensive reworking caused by a regional transgression.

According to bulk XRD-analysis Fruholmen Formation (Facies 1 through 4) displays moderate amounts of feldspar content (20-25%) with a predominance of plagioclase. Fruholmen Formation was deposited during the Late Triassic (Early Norian to Rhaetian) which according to previously discussed studies suggests a predominant source area from the east (Figure 6.1). This coincides with the abundance of plagioclase feldspars (Figure 5.12) found in Fruholmen Formation which is characteristically seen in deposits transpiring from the Uralian hinterland (Mørk, 1999). When point counted, the feldspars are largely considered altered and unidentifiable meaning that feldspars could not be identified as either plagioclase or K-feldspar. This infers that a significant amount of feldspar dissolution took place during early diagenesis which inherently suggests that kaolinite was precipitated. This theory is supported by moderate amounts of kaolinite and dickite detected in bulk XRD-analysis in Facies 1 through 4. The high degree of feldspar alteration can possibly be related to the increasingly humid climate that is proposed during this time period.

Stø Formation (Facies 6) is classified as a mature quartz arenite constituting on average 87% quartz, 7% feldspar and only trace amounts of kaolinite. In accordance with previous
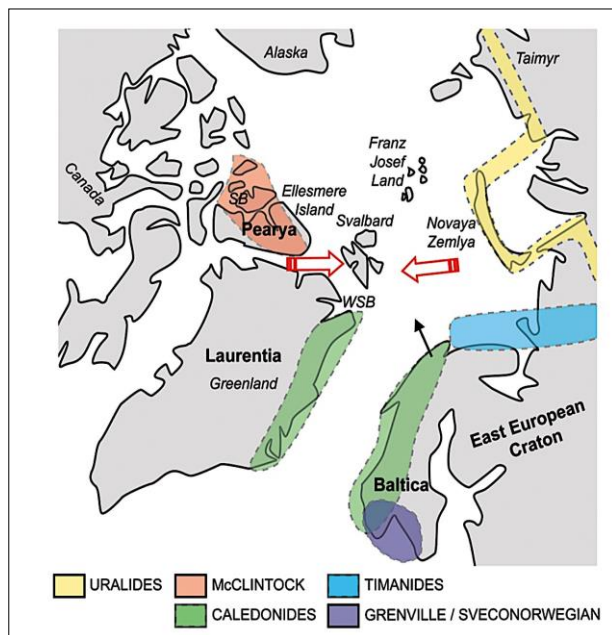
Figure 6.1: Red arrows depicting main source areas during the Triassic. Early- to Middle Triassic corresponding to a westerly source (Greenland and Artic Canada) and Late Triassic corresponding to an easterly source (Uralides). Early- to Middle Jurassic deposits show a mixed zircon signature potentially inferring a new source area from the Caledonides (black arrow) along with erosion and reworking of local source areas *(modified from Pozer Bue & Andresen, 2015)*.

Discussion studies it seems likely that Stø Formation was subjected to extensive reworking resulting in chemically unstable minerals repeatedly being leached, precipitated and reworked. Tectonically the Hoop Fault Complex was active during Mid Triassic-Late Jurassic (section 2.2.1 Tectonic and stratigraphic evolution of the Barents Sea) meaning that local source areas may have transpired from uplift and erosion, potentially resulting in reworking of underlying formations (Fruholmen, Tubåen and Nordmela) and subsequent deposition of a mineralogically more mature sandstone in Stø Formation.

Stø Formation (Late Pliensbachian to Bajocian) according to Pozer Bue & Andresen (2015) falls under the group of mixed zircon signatures. A possible theory postulated by Ryseth (2014), refers to Late Triassic-Early Jurassic uplift and erosion of the Caledonides. This would provide a new sediment input and a change in drainage patterns in addition to potential reworking of previously deposited sediments (Figure 6.1). This theory is further supported by palaeogeographic reconstructions by Smelror et al. (2009) who proposes that a major marine embayment developed in the South and North Barents basins subsequently preventing sediments from the Uralides reaching the western Barents Sea. This impediment would successively change the initial mineral assemblages seen between Fruholmen and Stø Formations.

6.3 Diagenesis

Diagenetic processes change the original reservoir properties and are caused by early chemical reactions, mechanical compaction and chemical compaction. All three diagenetic processes are seen throughout both wells indicating e.g. to which temperature sediments have been exposed to. The implications on reservoir properties caused by these processes will be further discussed in the following sections.

6.3.1 Intergranular Volume

The intergranular volume is the volume of pore space, cement, and depositional matrix in grain-supported sandstones subsequent to mechanical and chemical compaction (Eq. 8) (Paxton et al., 2002). All analysed samples are grain-supported, very fine- to medium-grained sand and range from moderate- to moderately-well sorted. Cements that are included from point counted results include calcite, quartz and authigenic pore-filling minerals such as kaolinite and chlorite.

Figure 5.25 illustrates that a majority of samples plot in the lower left area of the diagram, exemplifying that the predominant loss of porosity is caused by compactional processes and relatively little by cementation. Further evidence supporting a significant compactional regime is seen in the textural analysis where a majority of grain contacts are measured as straight-elongate (long) followed by concave-convex.

Maximum estimated burial for both wells ranges between 2162-2382m, which equates to approximately 21-24MPa and is theoretically able to reduce porosity to 35-25% in clean sandstones. Matrix and ductile grains accentuate mechanical compaction by filling available pore spaces when compressed and is therefore able to reduce porosity further. The resultant porosity observed in Fruholmen Formation, which comprises relatively high matrix constituents is therefore expectedly diminished due to mechanical compaction. Stø Formation exemplifies a relatively clean, fine- to medium-grained, mature sandstone which accordingly, shows higher porosity values. Sandstones consisting primarily of rigid grains typically exhibit a close packed geometry subsequent to mechanical compaction, leading to a theoretical porosity value of approximately 26%. Average porosity in Facies 6 is measured at 19% meaning that an additional 7% porosity loss is caused by chemical processes.

The four outlying values (plotted as triangles) shown in the upper right area (Figure 5.25) are fully calcite cemented samples illustrating high intergranular volumes but relatively low intergranular porosities. The average porosity loss due to compactional processes seen in calcite cemented samples is 12.50% and is significantly higher in non-calcite cemented samples (data plotted as circles) which averages 35.77% (Table 5.2). Calcite cement can therefore be assumed to have developed during early diagenesis as this would impede mechanical compaction by strengthening the grain-framework and effectively counteract vertical stress. Intergranular porosities illustrated in Figure 5.25 are further adjusted according to Equation 12 (Table 6.1). By subtracting cement and depositional matrix from intergranular volume a more accurate estimate with regard to point counted porosity values are obtained (Table 6.1).

Table 6.1 Average intergranular porosity values calculated using equations by Houseknecht (1987) (Eq.11) and Paxton et al. (2002) (Eq. 12). A large discrepancy is seen between the two calculated values. The reduced porosity according to Paxton et al. (2002) is due to matrix being subtracted from intergranular porosity.

	Avg. Intergranular Porosity	
Facies	**(Houseknecht, 1987)**	**(Paxton et al., 2002)**
1	17.33%	4.67%
2	16.75%	3.00%
3	16.56%	10.81%
4	21.04%	5.83%
6	20.25%	19.04%
Calcite cemented	7.46%	1.42%

Intergranular volume is based on point counting, which is a subjective method whereby results are highly dependent on experience. Examples that can potentially lead to skewed results are given by Paxton et al. (2002) and will be further discussed with emphasis on Facies 4, which may lead to future reassessment of results in this thesis. Note also that all samples are not point counted due to exceedingly fine grain sizes. This also leads to skewed results as samples not included would significantly alter the averages seen in respective facies. For example, only three of six samples were point counted for Facies 1 meaning that half of the samples are not grain supported and are subsequently not considered for reservoir quality. For complete point counted data see Table 10.4 and 10.5.

Mechanical compaction is a result of increased burial and typically includes grain rearrangement, ductile deformation, dissolution and brittle fracturing. Therefore, heterolithic sandstones containing an abundance of ductile grains or matrix (e.g. Facies 4) are expected to undergo severe porosity loss during the mechanical compaction regime. When conducting petrographic point counting, care must be taken not to confuse clay-rich ductile grains with depositional matrix. Clay-rich ductile grains are originally part of the grain-framework, however when exposed to vertical stress these grains can readily compact filling available pore space (Figure 6.2). If compacted clay-rich ductile grains are mistakenly counted as depositional matrix the resultant intergranular volume will be interpreted as higher and any further calculations will be biased (IGV = intergranular pore space + intergranular cement + depositional matrix) (Paxton et al., 2002).

According to logged core data (Figure 5.2) Facies 4 consists of an abundance of clay-rich, lithified rip-up clasts of varying sizes. Therefore, the relatively high intergranular volume illustrated in Facies 4 is subject to discussion. An overestimation of depositional matrix may lead to the suspiciously high intergranular volumes seen in the heterolithic, moderately sorted sandstone of Facies 4.

Ductile-Grain Sandstone
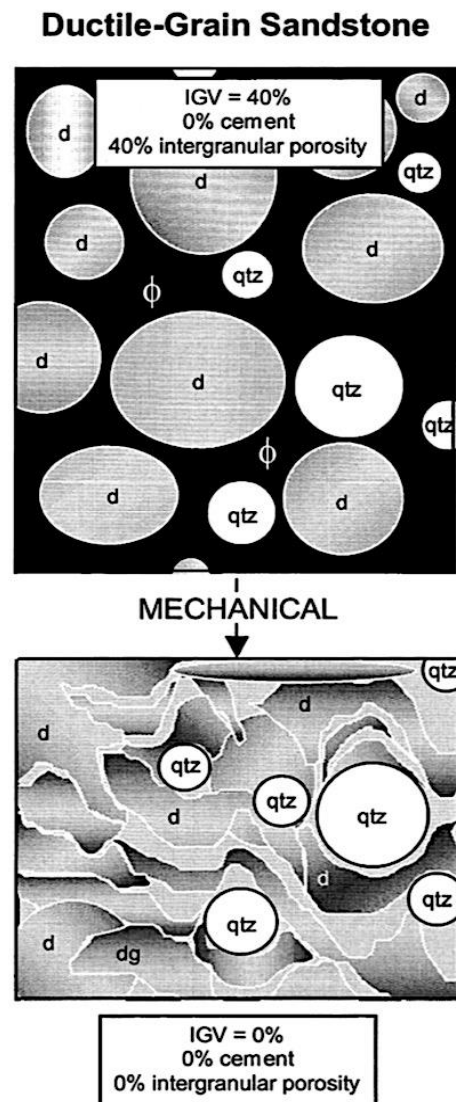
Figure 6.2: Progressive compaction of ductile and rigid grains. Note that intergranular volume decreases from 40% to 0% due to ductile deformation. When point counting, it is important to differentiate between ductile deformation and depositional matrix (after Paxton et al., 2002).

However, following the intergranular porosity equation by Paxton et al. (2002), (whereby matrix is subtracted from intergranular volume), renders very little porosity (5.83%) which also seems unlikely according to core plug data. The rip-up clasts seen in core logs are sporadic and varying in size, meaning that the porosity and permeability may differ depending on where samples are located.

Core plug data from Fruholmen Formation illustrates varying trends whereby permeability is generally depicted lower than porosity. Porosity trends for Fruholmen Formation range between 15-30%, illustrating significantly higher values than point count estimates. A possible cause for this discrepancy can be explained by the overall high matrix constituent in Fruholmen Formation. Matrix consists of fine grained particles which in turn, exhibit microporosity which is not detected during microscopic analysis. Although higher porosity values are observed in core-plug data, reservoir quality is diminished due to poor permeability caused by the extensive matrix contents.

Facies 6 is classified as a moderately-well sorted, fine grained sandstone and illustrates good reservoir quality (with the exception of two calcite cemented samples). The average intergranular volume is 25.25% which is expected from a mechanically compacted rigid grain sandstone (Paxton et al., 2002). The reservoir quality is further dependent on quartz cementation which is a function of deeper burial. According to point counted results, quartz cement is limited in Facies 6 which requires further explanations as estimated burial temperatures exceed 100°C in Wisting Central. Effects and consequences of deeper burial will be further discussed in section 6.3.4 (Chemical compaction).

Allogenic clays

Allogenic clays are predominantly seen in Fruholmen Formation (Facies 1 through 4), and are characterized as dispersed matrix or clay laminae. This can be correlated to depositional environments and is likely a factor of the tidally influenced regimes of Fruholmen Formation. The high percentages of allogenic clays seen in Facies 1, 2 and 4 have severe implications on intergranular porosity and furthermore, reservoir quality.

Mud draping is also seen in the Stø Formation from core photographs, which further indicates a tidally influenced depositional environment. However, point count results show negligible amounts of depositional matrix. Samples from the Stø Formation are predominantly taken from clean sandstone intervals in Wisting Central (7324/8-1) and may possibly be different if also sampled from Hanssen (7324/7). When analysed in SEM (samples B13 and B14), Stø Formation illustrates a predominant illite coating partially lining quartz grains (Figure 5.18 and Figure 5.19). This illitic grain coating can potentially be the result of clay infiltration subsequent to sediment deposition and/or a consequence of clay diagenesis subsequent to burial. The coating is not complete but partially covers individual grains and will be further discussed in section 6.3.4 (Chemical compaction).

6.3.2 Early Chemical Reactions

As explained in section 3.3.1, early chemical reactions take place in an open system meaning that sediments are able to react with the atmosphere or water. Therefore, these processes are limited to sediments within initial 10m of burial (Bjørlykke, 2015).

Kaolinitization

The main reaction corresponding to early diagenesis in studied samples is leaching of feldspar and muscovite and precipitation of pore filling authigenic kaolinite (Eq. 1 and 2 respectively). In order for these reactions to take place feldspar and muscovite have to be part of the initial mineral assemblage in addition to being exposed to a sufficient meteoric water flux. Furthermore, kaolinite is only able to precipitate if the resultant silica and potassium that is released from feldspar dissolution is continuously removed from the system. Therefore, when kaolinite is observed during early burial, sediments inevitably have to be considered as permeable, allowing a through flow of water.

Fruholmen Formation illustrates moderate amounts of feldspar and muscovite and smaller amounts of kaolinite and dickite (Figure 6.3) (dickite is the thermodynamic reaction product of kaolinite at temperatures exceeding 90ºC and will be discussed in section 6.3.4,
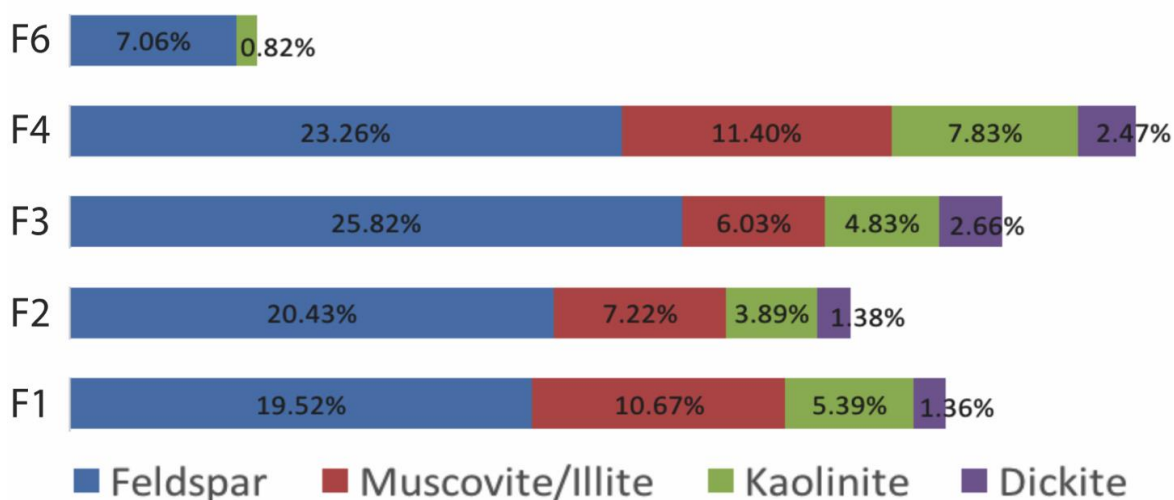
Figure 6.3: Average XRD-results for feldspar, muscovite/(illite), kaolinite and dickite for each analysed facies. The extent of feldspar alteration and kaolinite precipitation are signs of early diagenetic processes related to meteoric water flushing. Facies 1 through 4 show significantly higher values when compared to Facies 6.

however is for obvious reasons included here as part of the early feldspar/muscovite reaction). According to Bjørlykke (1998), the flux of water has to be significant to dissolve adequate amounts of feldspar and mica in order to precipitate a small percentage of kaolinite. These parameters are commonly met in fluvial and shallow marine environments in addition to humid climates (Bjørlykke, 1998), which coincides with interpreted depositional model applied to Fruholmen Formation (Figure 5.3). Sediments of the Fruholmen Formation must therefore have been exposed to substantial meteoric water flushing prior to deeper burial. This theory is strengthened by point counted results which demonstrate that the vast majority of feldspars are classified as altered/unidentifiable (Table 10.4 and Table 10.5). In order for sediments to be exposed to high meteoric flushing, sedimentation must also have occurred at an adequately slow rate for extensive leaching to take place. According to point counted samples Facies 1 through 4 classify as subarkosic arenites, however when taking into consideration extensive feldspar alteration, Fruholmen Formation may originally have plotted as an arkose, however, this is speculative.

Stø Formation shows considerably less signs of early chemical reactions. This is likely due to extensive reworking of underlying sediments as well as a new sediment source area containing less feldspathic minerals.

The effect of kaolinite on reservoir potential is trivial due to the relatively small amounts observed in XRD-analysis (Figure 6.3), however may have some implications on permeability.
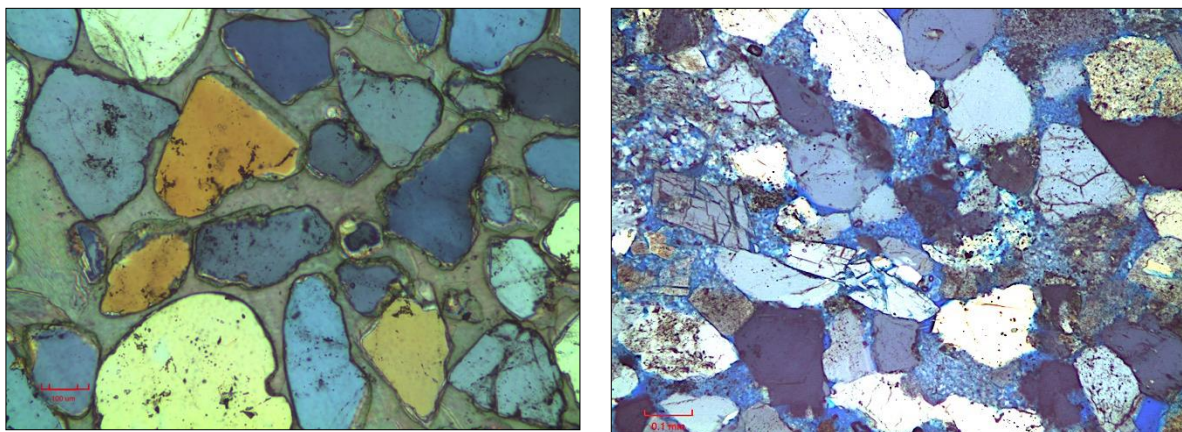
Figure 6.4: (Left) Calcite cemented interval (Sample B16, Facies 6) showing floating or tangential contact texture of quartz grains. (Right) Non-cemented sample showing grain rearrangement in terms of long and sutured contacts in addition to grain crushing caused by mechanical compaction (Sample B12, Facies 4).

Carbonate cementation

Calcite is observed in Facies 2 (samples B3 and B4), Facies 3 (sample A16) and Facies 6 (samples B16 and B17) as relatively thin intervals of pore-filling cement. Samples above and below the cemented samples show little or no calcite cement, suggesting that the pore-filling calcite is vertically discontinuous. Calcite cemented intervals are sporadically located throughout wells and facies meaning no direct trends can be inferred.

Textural differences are however noted, within calcite cemented thin-sections grains appear to be floating or exhibit tangential contacts. This implies that calcite cement precipitated and filled pores prior to mechanical compaction, preventing grain reorganization and crushing (Figure 6.4).

The inherent consequences of calcite cemented intervals are creating impermeable barriers that may severely affect the reservoir quality. However, the lateral extent is not known whereby no direct implications can be inferred.

No specific analyses were conducted in order to determine the origin of calcite. The dissolution of carbonate sediments and precipitation of calcite cement precedes that of feldspar leaching and thereby potentially creates barriers during early burial. This barrier may impede meteoric water flushing and protect subsequent leaching of feldspars in its ambient surrounding. However, due to sample spacing no immediate effects are observed that can confirm this theory.

6.3.3 Maximum Burial Estimates

Estimated maximum burial coupled with geothermal gradient histories are critical in order to evaluate the exploration potential of an area. Maturation and expulsion of hydrocarbons are highly dependent on the time spent within certain temperature ranges. Reservoir rocks are correspondingly a function of time, temperature and burial depths.

Increasing burial depth equates to an increase in ambient temperature, which changes mineral stability. Different methods are used to estimate exhumation, however are many times difficult to constrain due to significant erosion of sediments (hiatus). Results acquired from petrophysical analysis in conjunction with empirical compaction curves resulted in uplift estimations of 1600m and 1500m for Hanssen (7324/7-2) and Wisting Central (7324/8-1) respectively. Estimations correspond seemingly well when compared to published exhumation appraisals by Baig et al. (2016) (Figure 2.5). Although results agree with published data, uncertainties surrounding uplift is evident. Hanssen (7324/7-2) and Wisting Central (7324/8-1) are located 7km apart and show a 100m discrepancy in uplift. In order to depict whether the cause of this discrepancy is caused by wells being situated on different fault blocks within the Hoop Fault area, seismic analysis is necessary and does not cover the scope of this thesis.

When constructing uplift evaluations, mechanically compacted curves of empirical data are used. Limitations as to how accurately these curves fit the lithology in wells can be a constraining factor. Furthermore, if the mechanically compacted domain is assumed to be partly or entirely eroded due to exhumation, then empirical data curves become difficult to use or render obsolete. Presumptions are made based on sonic log data in which the transition between mechanical and chemical compaction is not clearly delineated in either well. If the mechanically compacted regime has in fact been completely eroded then exhumation cannot be estimated using this method. Consequently, exhumation results acquired in this thesis can only be used as approximations and cannot be accurately construed for the two wells.

Studies conducted on preglacial uplift and subsequent erosion of Svalbard and the Barents Sea region (Figure 6.5) shows Cenozoic sedimentation along the western Barents Sea margin (negative contours) and estimated erosion for the Barents Shelf (positive contours). The location of Hanssen (7324/7-2) and Wisting Central (7324/8-2) show erosional estimates within the range of 1500-2000m which again, corresponds well with estimated uplift based on sonic well log data.

The geothermal gradient is calculated using the recorded bottom hole temperature of the wells and equates to 38,8ºC Km^{-1} for Hanssen (7324/7-2) and 53,0ºC Km^{-1} for Wisting Central (7324/8-1), rendering a 14,2ºC Km^{-1} difference. Considering the geographical proximity of the two wells, results have to be deliberated. When estimating the geothermal gradient several important implications have to be considered. The recorded bottom hole temperatures of both cores does not necessarily represent an accurate present day
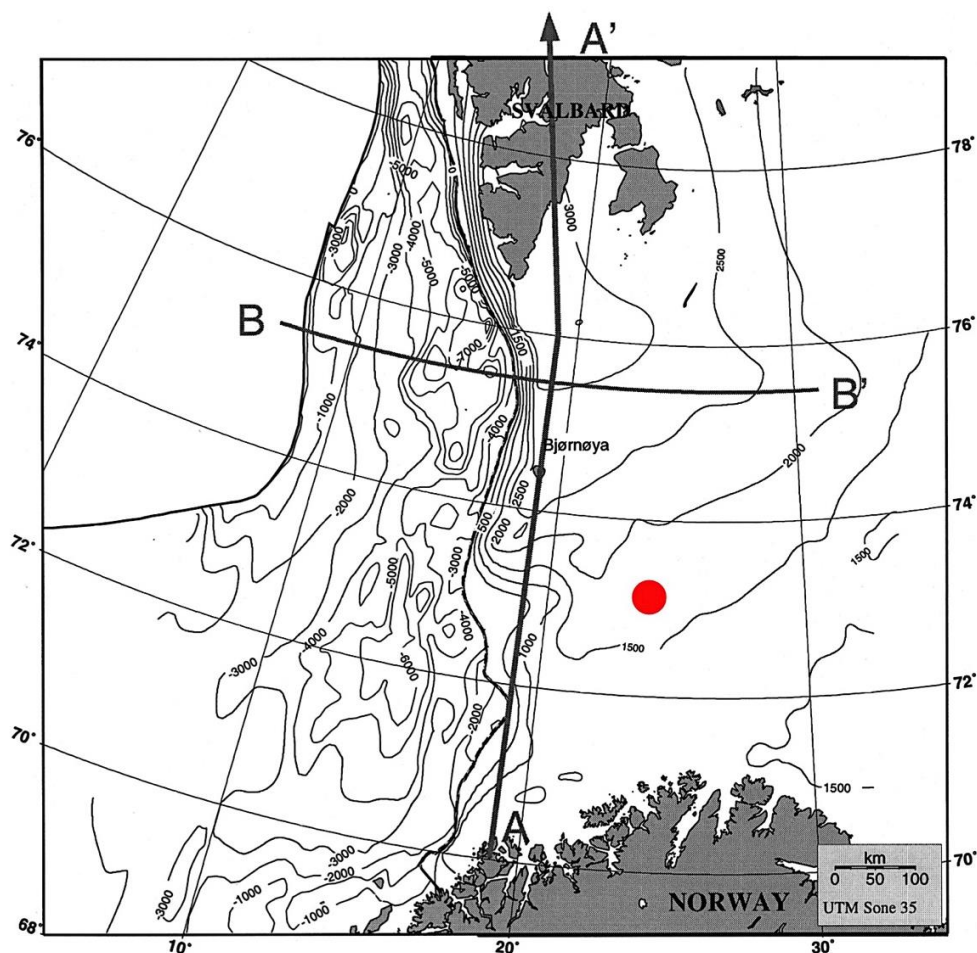
Figure 6.5: Thickness of Cenozoic sedimentation (negative contours) along the western Barents Sea margin and erosion estimates (positive contours) for the Barents Shelf. Approximate position of Hanssen and Wisting Central is marked by red circle (73º29'N, 24º14'E and 73º27'N, 24º24'E, respectively). *(modified after Dimakis et al., 1998).*

temperature, whereby further calculations and estimations of burial temperatures become skewed.

Maximum burial temperatures for the cored intervals are moreover based on exhumation estimates. Calculations show an estimated temperature range from 89,6-92,4ºC in Hanssen (7324/7-2) and 114,6-117,1ºC in Wisting Central (7324/8-1). In order to attain more accurate results, fluid inclusion analyses are highly recommended.

Temperature dependent reactions such as quartz cementation (initiated at 70ºC) and transformation of kaolinite to dickite (coexistent polymorphs at 90ºC) are used as auxiliary methods for interpreting the minimum temperatures that sediments have sustained. Considering the relatively small amounts of quartz cement that are noted from the quartz-rich Stø Formation in Wisting Central (7324/8-1), it seems likely that estimated maximum temperatures are overstated. Although partial illite coatings are observed in Stø Formation and are potentially a limiting parameter of quartz nucleation, temperature ranges of 114,6-117,1ºC are expected to yield more substantial quartz cementation than what is depicted

94

(Figure 3.8). Coexistent kaolinite and dickite are observed in Fruholmen Formation in both wells, indicating that temperatures have reached a minimum of 90ºC.

A steep geothermal gradient is produced by rapid uplift (erosion) which can possibly be an affect felt in the Southwestern Barents Sea (Figure 4.9). When rocks are rapidly uplifted due to erosion and isostatic rebound, the ambient temperature will increase due to warmer rocks being brought to the surface, which may partly explain the abnormally high geothermal gradient seen in particularly Wisting Central (7324/8-1). Studies conducted on western margin fans within the Barents Sea show that 2/3 of the sediments were deposited during the last 2.5 m.y. indicating that erosion must have proceeded rapidly within this time period. These high erosional rates are assumed to be caused by the glaciation that prevailed during the same period of time (Dimakis et al., 1998). This reasoning is however highly speculative and provides a supplementary point for further discussion.

6.3.4 Chemical Compaction

Chemical reactions occurring at deeper burial depths are considered to take place in a chemically closed system. Governed by a thermodynamic drive, precipitated minerals are more stable than the minerals being dissolved (Bjørlykke, 1998).

Quartz cementation

Once burial depth reaches a geothermal gradient corresponding to approximately 70ºC, quartz cementation is initiated representing a transition zone from mechanical- to chemical compaction. A small amount of quartz cement (2-4%) is needed to adequately strengthen the grain framework and counteract any further porosity loss caused by mechanical compaction (Bjørlykke & Jahren, 2015). The average amount of quartz cement in each Facies is relatively low (2-7%) (Table 10.4 and 10.5) however is still within sufficient range in order to terminate mechanical compaction.

Quartz cementation increases exponentially with temperature so long as sufficient surface areas are available (Figure 3.8). As quartz cementation proceeds, the available surface area decreases and subsequently retards the process (Bjørlykke & Jahren, 2015).

The variation in quartz cement seen in all facies is mainly attributed to the available surface area, (e.g. grain coatings in Stø Formation) and an unknown time of exposure to temperatures exceeding 70ºC.

Dissolution of quartz is also catalysed by mica or clay minerals located between grain contacts (Bjørlykke & Jahren, 2015), which can commonly be seen in the form of stylolites. Fruholmen Formation contains substantial amounts of matrix and moderate mica

constituents meaning that a catalytic effect may intuitively lead to an increase in the precipitation rate of quartz cement, however no such evidence was noted during analyses.

Stø Formation shows limited amounts of quartz cement (average 3.44%), which is potentially underestimated due to difficulties differentiating detrital quartz from quartz cement. However, delimiting factors are also encountered. A partial grain coating rim is seen lining many quartz grains. This illitic coating is potentially able to hinder or retard quartz cementation and is further discussed in the following section.

Illitization

Illite is sporadically observed during SEM-analysis throughout Fruholmen Formation as a pore-filling mineral. Stø Formation consists of relatively lower percentages of pore filling clays however, partial grain coated rims of illite are observed (Samples B13 and B14). The percentage of illite is difficult to quantify in bulk-XRD analysis due to the similar peaks produced by clastic mica (Bjørlykke, 1998).

Infiltration of any detrital clay can occur shortly after deposition as a result of water containing suspended clay particles. The allogenic clays are subsequently deposited on grain surfaces and in pore spaces (Matlack, 1989). The illitic clay seen in Fruholmen and Stø Formations can suggestively be deposited as part of infiltrated material and depending on the mineral constituents, subsequently altered due to diagenetic reactions. Different compositions are conceivable and difficult to ascertain through acquired results. Plausible alternatives are detrital illite, detrital smectite or detrital mixed – layer illite/smectite.

If the original composition of infiltrated clays are illitic, then no further chemical alterations transpire during diagenesis. If however the original composition is smectite or mixed-layer illite/smectite then diagenetic alterations are induced at approximately 70ºC, forming characteristic fibrous textures that are detrimental for reservoir permeability. In order for this reaction to transpire, a source of potassium has to be readily available which is typically fulfilled in the presence of K-feldspar. SEM analysis show very little fibrous textures associated with diagenetically formed illite, however are observed on occasion in Fruholmen Formation (Figure 6.6). Although no indication of smectite was observed during XRD- or SEM-analyses this reaction occurs at significantly reduced temperatures (65-75ºC), which can potentially explain the absence of smectite if complete alteration has taken place.

Authigenic illite can also form as an alteration product of kaolinite but is not favoured below temperature ranges of 120-140ºC (Bjørlykke, 1998), due to the increased energy that is required in order for illite to nucleate. Maximum burial temperatures are suggestively less than 120ºC which discredits the occurrence of this diagenetic reaction.
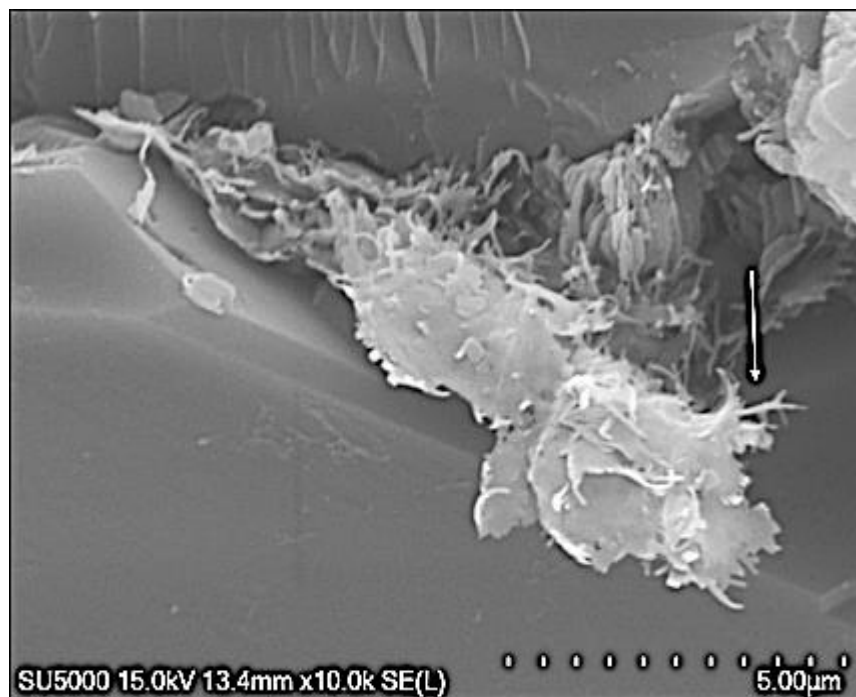
Figure 6.6: SEM image showing the onset of illitization (Sample A17, Facies 4). Note the fibrous textures starting to develop (indicated by arrow).

Results indicate that detrital clay infiltration is a likely source of the pore-filling illite observed in Fruholmen Formation, however no conclusive answers can be drawn with respect to which type of clay (illite, smectite or mixed layer illite/smectite) was originally infiltrated. Few fibrous textures are observed during SEM-analysis, possibly indicating precursory minerals such as smectite or mixed-layer illite/smectite (Figure 6.6).

Stø Formation consists of relatively low percentages of pore filling clays however, partial grain coated rims of illite are observed during SEM-analyses (Samples B13 and B14). Images show illite as a thin (2μm), partial grain coating rim (Figure 5.18), devoid of the characteristic authigenic fibrous textures which expectedly form due to diagenetic reactions.

Experimental simulations of suspended clay infiltration have been conducted by e.g. Crone (1975) and Matlack (1989). Under simulated vadose conditions, Crone (1975) found that infiltrated clay (mixed-layer illite/montmorillonite) formed meniscus-shaped bridges between framework grains around points of contact and near contacts. Further studies by Matlack (1989) showed that several variables affect the infiltration process and emplacement of allogenic clays in sandstones. The shape and size of framework pores control the initial capacity of water infiltration. Medium grained sands exhibit larger pore throats and higher permeability, resulting in greater flow rates. Finer grained sands and poorly sorted sediments are less permeable and more likely to form stagnant pore water conditions, resulting in pore filling clays and mudcakes as opposed to grain lining.

Depositional environments are also of equal importance when pore lining clays are observed. Sediments deposited in environments with fluctuating water levels typical of delta plains and point bars are more likely to experience infiltration than others (Matlack, 1989). In order to retain infiltrated clays, subsequent reworking of sediments has to be limited. Chemical parameters affecting the adhesion of suspended clays to grain surfaces were also observed when comparing simulated laboratory studies using distilled water and experiments using untampered water from the Missouri River suggesting that chemical composition of infiltration waters may yield variable results.

Stø Formation is a fine- to medium-grained, moderately well sorted sandstone exhibiting good permeability and potential for clay infiltration. The partial grain coatings observed in two samples inherently suggest that reworking subsequent to deposition has been limited. The depositional environment for Stø Formation is interpreted as subaqueous dunes formed in large sandflats within a high-energy shallow marine to fluvial-tidal environment. This type of environment is exposed to many variable factors e.g. fluctuating water levels imposed by tides, sediment input and reworking by waves. By implying a tidally influenced environment, possibilities of vadose zones arise. If the sandflats in Stø Formation where intermittently subaerial then the prospect of infiltration and clay emplacement is increased. The partial grain-coatings also contest little reworking of sediments subsequent to infiltration. Stø Formation is interpreted as an extensively reworked sandstone, meaning that clay infiltration must have taken place subsequent to reworking in order to be preserved.

Only two samples (B13 and B14) from Stø Formation (Wisting Central) were analysed in which partial illite coatings were observed. Due to this small quantity of analysed samples and close proximity within the core, no direct implications can be drawn as to whether these coatings are sporadically distributed or continuous throughout the Stø Formation in Wisting Central. However, due to the good porosity seen throughout the Stø Formation intuitive assumptions can be made based on quartz cementation. Grain-coatings reduce the surface area available for quartz nucleation and can potentially preserve intergranular porosity. Despite temperatures exceeding 70ºC, quartz cement only represents 0-8% of the intergranular volume in all analysed samples. The proposed low percentage of quartz cement can potentially be explained if the observed illite coating was deposited as an allogenic, infiltrated clay, adhering to grains during early burial.

The intergranular volume in Facies 6 is approximately 26% which is expected from mechanically compacted clean sandstones. Only a small percent (2-4%) quartz cement is

required to effectively shut down mechanical compaction (Bjørlykke & Jahren, 2015). According to point count results, quartz cement is sufficient in order to terminate mechanical compaction but further limited due to restricted surface areas caused by partial grain coatings.

6.4 Reservoir Quality

Reservoir quality will be further assessed with regard to previously discussed parameters, which effectively determine the porosity and permeability observed in both respective wells.

Based on core plug data, sedimentological logging and thin section analyses, Facies 1 and 2 can be discarded with regard to reservoir quality. Several samples could not be analysed petrographically due to the amount of fine-grained matrix constituting the bulk of these samples. Thereby, reservoir quality is assumed negligible and will not be further discussed. Facies 3, 4 (Fruholmen Formation) and Facies 6 (Stø Formation) show varying qualities with regard to reservoir properties and will subsequently be discussed and characterized.

6.4.1 Facies 3 – Fruholmen Formation

Facies 3 is a relatively clean, fine grained, moderately-well sorted sandstone. An average of 39% of initial porosity of non-calcite cemented samples is estimated to be lost due to compactional processes and 20% due to cementation (Table 5.2). This results in an intergranular porosity average of 15% according to equations published by Houseknecht (1987). The intergranular volume however, also represents depositional silt and clay-sized particles (matrix), characteristically containing micro-porosities which can subsequently render the permeability of a reservoir. Therefore, a more accurate estimation of the reservoir quality is gained from point counted results (or intergranular porosity according to Paxton et al., 2002), showing an average of approximately 10%. Following reservoir appraisal values published by Tissot & Welte (1984), 10-15% porosity characterizes Facies 3 as *fair*.

Maximum burial for logged core sections are estimated between 2,162-2,382m with temperature ranges of 89-117ºC which places cores at intermediate burial depths. Expectedly, the dominant pore reducing parameter is mechanical compaction. Mechanical compaction is further dependent on four factors: clay content, percentage of ductile grains, textural parameters (e.g. sorting), and burial depth/effective stress (Blatt, 1992).

Relatively high matrix, mica and lithic fragments (12.3% total) observed in Facies 3 may have had a significant impact on mechanical compaction. Ductile grains and matrix are

able to bend around the more ridged quartz and feldspar grains to fill pore spaces and increase grain packing arrangements. Allogenic clays (matrix) further augment mechanical compaction by reducing friction that can arise between framework grains. Core-plug data show a large variation in permeability. Samples range from very good to poor indicating a spread in reservoir quality. Intermittently occurring matrix laminae may cause impermeable barriers resulting in poor permeability.

The effects of chemical processes are specifically seen as long and concave-convex grain contacts, caused by dissolution of quartz grains at points of contact. Although mechanical compaction is the dominating pore reducing factor, quartz cement is estimated at 4.8% which is adequate according to Bjørlykke & Jahren (2015) to stabilize grain-framework and prevent further mechanical compaction. In the absence of grain-coatings it is assumed that quartz cement initiated at approximately 70ºC and successively concluded mechanical compaction.

Authigenic minerals such as kaolinite, illite and quartz cement are difficult to identify when point counting and are likely underestimated. Point counted results show a predominance of altered/unidentifiable feldspars which inherently suggests that kaolinite is an important factor to be considered. SEM-analyses show prevailing quantities of pore-filling kaolinite intermixed with small amounts of illite, which further suggests that reservoir quality is characteristically no more than *fair*.

6.4.2 Facies 4 – Fruholmen Formation

Facies 4 illustrates a very fine-grained, moderately sorted sandstone. Approximately 23% of initial porosity is estimated to be lost due to compactional processes and 25% due to cementation. This results in an intergranular porosity (according to Houseknecht,1987) of 21.04% which again represents high values of depositional silt and clay-sized particles (matrix). Point count results show an average primary porosity estimation of 5.38%, which further characterizes this facies in terms of reservoir properties as *poor*.

Significant amounts of mud-rich, rip-up clasts of varying size and quantities are seen throughout Facies 4 but are not laterally continuous. Core-plug data show several samples plotting with good porosity and permeability meaning that the surrounding sand in which the rip-up clasts are situated is potentially better than what point count results depict.

Comparably to Facies 3, a high degree of pore-filling kaolinite intermixed with small amounts of fibrous illite is seen during SEM-analyses. The initial alteration process can again be related back to early weathering reactions of feldspars, indicating that significant

amounts of meteoric water flushing took place. With regard to reservoir quality the kaolinite-illite mixture is unfavourable.

Quartz cement on the other hand is minimal at 2.92% which is marginally sufficient in order to terminate mechanical compaction. Indicated burial temperatures are well within quartz cementation ranges, which means that either quartz cement is underestimated when point counted or negligible surface areas were available for quartz cementation to nucleate. Either one of these explanations is plausible, and thereby difficult to ascertain. With high amounts of mechanically compacted depositional matrix and/or rip-up clasts, a large portion of available pore space is subsequently occupied by fine-grained particles..

Point-counted samples indicate that primary porosity varies between samples (approximately 0-10%), meaning that some samples exhibit better porosities than others. This may also indicate that the fine-grained particles are intermittently occurring rip-up clasts following that certain parts of Facies 4 have better porosities and others are negligible. When porosities are averaged a predominance of poor porosity is obtained which may be somewhat skewed. If more samples within Facies 4 were point counted and a distinct differentiation is made between depositional matrix and deformed mud-rich rip-up clasts a more accurate intergranular volume is attained which could potentially lead to better reservoir quality.

6.4.3 Facies 6 – Stø Formation

Facies 6 is a relatively clean, fine-grained, moderately well sorted sandstone. Approximately 37% of initial porosity is estimated to be lost due to compactional processes and 13% due to cementation. This results in an intergranular porosity (according to Houseknecht, 1987) of 20%. Point count results show an average primary porosity estimation of 17% which further characterizes this facies in terms of reservoir properties as *good*. Facies 6 shows very little depositional matrix and quartz cement, meaning that a high percentage of accounted intergranular volume consists of primary porosity. Furthermore, two out of eight samples are partially or fully calcite cemented which notably lowers the average primary porosity. Fully cemented samples may however create impermeable vertical barriers depending on the lateral extent which may for obvious reasons have implications on potential reservoir quality.

Exceptionally low quartz cement values are estimated from point count results. This is suggestive a result of allogenic grain coating clay. SEM-analysis show a partial illitic grain coating on many quartz grains which can potentially explain the lack of quartz cement and preservation of porosity. By reducing available surface areas needed for quartz cement

to nucleate this allogenic illite may have inhibited or retarded quartz cementation during burial temperatures exceeding 70ºC allowing for a lower than expected average. 3.86% cement is however adequate for mechanical compaction to terminate by which no extensive grain crushing or contact dissolution is observed.

6.4.4 Porosity and Permeability

According to core plug data, Facies 3 and 4 in Hanssen show that half of tested samples have good to very good horizontal permeability, the other half falling below or close to the cut-off line for fair horizontal permeability. Porosity remains above the good cut-off line for all samples, with the exception of one sample in Facies 3.

Slightly lower qualities are observed in Wisting Central showing four samples (two from Facies 3 and two from Facies 4) with good to very good horizontal porosity and within the fair permeability zone and 2 samples bordering fair to good horizontal porosity but falling below fair horizontal permeability. Notably, less samples are taken from both respective facies in Wisting which may lead to slightly skewed observations. Overall reservoir quality for Fruholmen Formation increases from Facies 1 and 2 to Facies 3 and 4 indicated by better porosity and permeability.

Facies 6 is not included in diagram data for Hanssen due to no further data sampling and can therefore not be discussed or compared with regard to petrographic analyses. However, Facies 6 is sampled in Wisting Central and is subsequently represented in the porosity-permeability diagram. Nonetheless, many of the sampled depths show no available core plug data whereby only 4 data plots are represented in the diagram, one of which is fully cemented showing negligible values. The remaining 3 show very good horizontal porosity and very good to good horizontal permeability.

Comparing this quantitative data with previously discussed petrographic analyses it renders plausible that Facies 6 shows the best reservoir potential. Facies 3 is conclusively *fair* in terms of reservoir quality due to moderate primary porosity observations, persistent pore filling kaolinite/illite in addition to relatively high values of quartz cement and depositional matrix. Facies 4 requires further data collection potentially increasing the reservoir potential. The interstitial sand shows similar properties to that of Facies 3, indicating that porosity and permeability is inherently better between the mud-rich rip-up clasts. Table 6.2 summarizes the results from petrographical analyses with resulting reservoir quality

Table 6.1: Mineral composition and textural properties with resultant reservoir quality for each analysed facies.

	Properties	Facies 3	Facies 4	Facies 6	Effect on Reservoir Quality
Initial Composition	Quartz	48.18%	46.75%	68.19%	• Framework grain
	Feldspar	16.90%	15.46%	4.06%	• Framework grain • Early diagenic dissolution and precipitation of pore-filling kaolinite
	Allogenic Clay (matrix)	6.1%	15.21%	1.16%	• Increases mechanical compaction due to reduced friction between framework grains • Reduces primary porosity
Authigenic Minerals	Kaolinite	2.40%	5.88%	0.09%	• Pore-filling mineral
	Calcite Cement	2.20%	0.17%	5.28%	• Reduces porosity • Creates vertical barrier to fluid flow • Prevents feldspar dissolution • Reduces mechanical compaction
	Quartz Cement	4.81%	2.92%	3.86%	• Reduces porosity • 2-4% enough to terminate mechanical compaction
	Illite	Pore-filling mineral seen intermixed with kaolinite (allogenic?)	Pore-filling mineral seen intermixed with kaolinite (allogenic?)	Grain Coating (allogenic?)	• Pore-filling illite is detrimental to reservoir quality • Grain-coating allogenic illite inhibits/retards quartz nucleation (?)
Texture	Grain Size	Fine Sand	Very Fine Sand	Fine - Medium Sand	• Smaller grain-sizes reduce mechanical compaction due to larger surface areas
	Sorting	Mod. Well Sorted	Mod. Sorted	Mod. Well Sorted	• Better sorting generally reduces mechanical compaction
	Avg. Intergranular Volume	24.42%	30.88%	25.25%	• Volume between framework grains occupied by porosity, matrix and cement
	Avg. Intergranular Porosity (Houseknecht, 1987)	16.56%	21.04%	20.25%	• Volume between framework occupied by porosity and matrix
	Avg. Point Counted Porosity	10.00%	5.83%	16.73%	• Porosity available for hydrocarbon storage
	Mechanical Compaction	38.95%	22.81%	36.88%	• Loss of porosity due to effective vertical stress
	Chemical Compaction	19.65%	24.58%	12.50%	• Loss of porosity due to mineral alteration
Reservoir Quality		FAIR	POOR	GOOD	

7. Conclusions

The objective of this study is to characterize the reservoir quality of Fruholmen and Stø Formations respectively in Hanssen (7324/7-2) and Wisting Central (7324/8-1). Reservoir characterization is based on sedimentological logging, petrographic- and petrophysical analyses. XRD-analysis and point count analyses (mineralogical composition, grain size, grain contacts and grain shapes) have been conducted on grain supported samples in both respective wells. Furthermore, SEM and CL-analyses were conducted on a few select samples in order to gain a better understanding of authigenic minerals (i.e. clay content and quartz cement). The reservoir quality ascribed to each facies is a function of provenance, depositional environment and burial diagenesis. Conclusively, each of these parameters play a significant role when characterizing the reservoir potential that can be expected in the vicinity of respective drill cores. Facies 1 and 2 show negligible porosity and permeability due to high matrix content whereby reservoir quality is discarded. Facies 3 and 4 show fair and poor reservoir quality respectively. Facies 4 contains a high content of mud-rich rip-up clasts which may mask a potentially better reservoir quality. During petrographical analyses these rip-clasts should be considered as part of the grain framework and not depositional matrix which may have led to skewed results. Facies 6 shows good reservoir characteristics illustrated by high primary porosity, little cement and negligible depositional matrix. The following processes are contributory factors influencing the reservoir quality seen through logged intervals of Hanssen (7324/7-2) and Wisting Central (7324/8-1):

- Initial mineral composition is largely governed by provenance and consequent depositional environments. A difference in mineral composition and maturity is seen between Fruholmen and Stø Formations which leads to substantial disparities in subsequent analyses. A change in mineral composition is believed to have been caused by a change in provenance from the Uralides to a more proximal Caledonide source area in addition to extensive reworking of sediments. Moderate amounts of feldspar are seen throughout Fruholmen Formation consequently leading to a higher constituent of authigenic kaolinite. Stø Formation on the other hand illustrates relatively low percentages of feldspar and a higher degree of detrital quartz, further suggesting a change in depositional environments and reworking of previously deposited sediments.

- Depositional environments are of great importance as this determines grain size and sorting within formations and largely dictates the resultant reservoir quality observed in each analysed facies. The energy of depositional regimes governs the ability to erode, transport or deposit sediments leading to a variation in grain size and sorting. Facies 1 and 2 render poor reservoir qualities due to the high constituent of fine grained matrix seen throughout samples. These Facies have been interpreted to be deposited within a mouth bar fringe zone and transition zone between distal (F1) and proximal (F3) environments in an interdistributary bay and mouth bar complex. Facies 3 and 4 illustrate fair and poor reservoir quality respectively and demonstrate higher-energy (more proximal) characteristics of a mouth bar and distributary channel environment. Despite the large amount of rip-up clasts seen in Facies 4 the interstitial sand shows similar characteristics to that of Facies 3 possibly representing a better reservoir quality that depicted herein.

- The original feldspar and mica composition in addition to meteoric water flux (early diagenesis) is fundamentally important with regard to the amount of authigenic kaolinite observed. Kaolinite is an alteration product of feldspar and mica which means it has relatively little effect on porosity however it may impede permeability. Facies 1 through 4 all show significantly altered feldspars and moderate amounts of authigenic kaolinite.

- Mechanical compaction is the predominant pore reducing factor in all analysed facies (excluding calcite cemented intervals) based on equations provided by Houseknecht (1987) and Paxton et al. (2002).

- Quartz cement (chemical compaction) is initiated at approximately 70°C and proceeds until ambient temperatures are reduced. All facies show an average of 2-8% quartz cement which, according to Bjørlykke & Jahren (2015) is sufficient in order to terminate mechanical compaction. In clean sandstones, quartz cement is the main pore reducing parameter subsequent to mechanical compaction. Therefore, a substantial amount of pore-filling quartz cement is expected in Facies 6. However, point counting rendered an average of 3% quartz cement suggesting further discussions as to why such low cement

percentages were observed. For more accurate results, additional cathodoluminescence analysis is recommended in order to confirm or discredit point count results. However, a thin allogenic illite coating is seen partially lining quartz grains which may have inhibited or retarded quartz nucleation and resulted in subdued cementation and good porosity.

- When buried to adequate ambient temperatures and in the presence of potassium, smectite becomes thermodynamically unstable and produces illite via mixed-layer minerals. Authigenic illite is regarded as detrimental for reservoir quality, but is only seen in small quantities (mainly within Facies 3 and 4) when analysed in SEM.

8.   Further Work

In order to characterise Fruholmen and Stø Formations with greater accuracy several additional analyses are recommended.

- Clay XRD-analysis would help ascertain which types of clay minerals are found in each facies as well as to what extent. Authigenic clay, especially illite is detrimental to reservoirs whereby further analysis would be beneficial.

- A more comprehensive cathodoluminescence analysis with emphasis on quartz cement would be helpful to more accurately determine intergranular volumes. Point counted values are rough estimates due to difficulties encountered when differentiating between detrital quartz grains and cement.

- To gain a better understanding of provenance and palaeogeographic drainage patterns, a zircon analysis is beneficial. An understanding of the geographical extent of reservoirs is imperative prior to drilling whereby zircon analysis could lead to a more comprehensive understanding of where sediments are predominantly sourced.

- Trace fossil analyses could also be beneficial in order to more accurately determine and understand depositional environments.

- A new point count analysis of Facies 4 is recommended in order to re-evaluate reservoir potential.

9. References

Adams, A.E., Mackenzie, W.S., & Guilford, C. 1984. *Atlas of sedimentary rocks under the microscope.* Longman: Wiley.

Allen, J.R.L. 1980. Sand waves: A model of origin and internal structure. *Sedimentary Geology, 26* (4), 281-328.

Ali, S.A., Clark, W.J., Moore, W.R., & Dribus, J.R. 2010. Diagenesis and Reservoir Quality. *Oilfield Review, 22* (2), 14-27.

Baig, I., Faleide, J.I., Jahren, J., & Mondol, N.H. 2016. Cenozoic exhumation on the southwestern Barents Shelf: Estimates and uncertainties constrained from compaction and thermal maturity analyses. *Marine and Petroleum Geology, 73,* 105-130.

Bergan, M. & Knarud, R. 1992. Apparent changes in clastic mineralogy of the Triassic-Jurassic succession, Norwegian Barents Sea: possible implications for palaeodrainange and subsidence. *Artic Geology and Petroleum Potential, Norwegian Petroleum Society (NPF), Special Publication,* 2, 481-493

Berglund, L.T., Augustson, J., Færseth, R.B.F., Gjelberg, J. & Ramberg-Moe, H. 1986. The evolution of the Hammerfest Basin. *In: Habitat of hydrocarbons on the Norwegian Continental Shelf. Norwegian Petroleum Society.* Edited by Spencer, A.M. Springer.

Bjørlykke, K. 1998. Clay mineral diagenesis in sedimentary basins – a key to the prediction of rock properties. Examples from the North Sea Basin. *Clay minerals, 33* (l), 15-34.

Bjørlykke, K. 2015. Introduction to Sedimentology – Sediment transport and sedimentary environments *In: Petroleum Geoscience: From Sedimentary Environments to Rock Physics.* Edited by Bjørlykke, K. Ed. 2. Berlin: Springer.

Bjørlykke, K., **Høeg, K. & Mondol, N.H.** 2015. Introduction to Geomechanics: stress and strain in sedimentary basins. *In: Petroleum Geoscience: From Sedimentary Environments to Rock Physics.* Edited by Bjørlykke, K. Ed.2. Berlin: Springer.

Bjørlykke, K. & Jahren, J. 2015. Sandstones and Sandstone Reservoirs. *In: Petroleum Geoscience: From Sedimentary Environments to Rock Physics.* Edited by Bjørlykke, K. Ed. 2. Berlin: Springer.

Blatt, H. 1992. *Sedimentary Petrology.* Ed. 2. New York: W. H. Freeman and Company.

Blatt, H., Tracy, R.J., & Owens, B.E. 2006. *Petrology - Igneous, Sedimentary, and Metamorphic.* Ed. 3. New York: W. H. Freeman and Company.

Breivik, A.J. 1998. *Crustal structure and development of the SW Barents Sea and the adjacent continental margin.* Doctor Scientiarum Thesis, University of Oslo, Norway.

Chuhan, F. A., Kjeldstad, A., Bjørlykke, K., & Høeg, K. 2002. Porosity loss in sand by grain crushing. Experimental evidence and relevance to reservoir quality. *Marine and Petroleum Geology* 19 (1), 39-53.

Dalrymple, R.W., Kurcika, C.E., Jablonski, B.V.J., Ichaso, A.A. & Mackay, D.A. 2015. Deciphering the relative importance of fluvial and tidal processes in the fluvial–marine transition. *In: Developments in Sedimentology.* Edited by Philip, J., Ashworth, J.L.B. & Daniel, R P. Elsevier.

Dashtgard, S.E. & La Croix, A.D. 2015. Sedimentological trends across the tidal–fluvial transition, Fraser River, Canada: A review and some broader implications. *In: Developments in Sedimentology.* Edited by Philip, J., Ashworth, J.L.B. & Daniel, R.P. Elsevier.

Davis, R.A. 2012. Tidal Signatures and their Preservation Potential in Stratigraphic Sequences. *In: Principles of Tidal Sedimentology.* Edited by Davis JR, R.A. & Dalrymple, R.W. Dordrecht: Springer.

Dimakis, P., Braathen, B.I., Faleide, J.I., Elverhøi, A. & Gudlaugsson, S.T. 1998. Cenozoic erosion and the preglacial uplift of the Svalbard-Barents Sea Region. *Tectonophysics* 300, 311-327

Doré, A.G. 1995. Barents Sea Geology, Petroleum Resources and Commercial Potential. *Artic,* 48, 207-221.

Dott JR, R.H. 1964. Wacke, Graywacke and Matrix-What Approach to Immature Sandstone Classification? *Journal of Sedimentary Research,* 34.

Dutrow, B.L. & Clark, C.M. 2016. X-ray Powder Diffraction (XRD). [Electronic]. *http://serc.carleton.edu/research_education/geochemsheets/techniques/XRD.html* (2017.01.29)

Faleide, J.I., Bjørlykke, K. & Gabrielsen, R.H. 2015. Geology of the Norwegian Continental Shelf *In: Petroleum Geoscience: From Sedimentary Environments to Rock Physics.* Edited by Bjørlykke, K. Ed. 2. Berlin: Springer

Faleide, J.I., Gudlaugsson, S.T. & Jacquart, G. 1984. Evolution of the western Barents Sea. *Marine and Petroleum Geology,* 1, 123-150.

Fitriyanto, A. 2011. Structural analysis of the Hoop Fault Complex, SW Barents Sea. MSc Thesis, University of Oslo, Norway.

Flohr M.J.K. 2000. X-Ray Powder Diffraction. *U.S. Geological Survey.* [Electronic]. https://pubs.usgs.gov/info/diffraction/html/ (2017.01.30)

Folk, R.L. 1974. *Petrology of Sedimentary Rocks: The University of Texas, Geology 370 K, 383 L, 383.* Hemphill

Gabrielsen, R.H. 1984. Long-lived fault zones and their influence on the tectonic development of the south-western Barents Sea. *Journal of Geological Society of London,* 141, 651-662.

Gabrielsen, R.H., Færseth, R.B., Jensen, L.N., Kalheim, J.E. & Riis, F. 1990. Structural elements of the Norwegian continental shelf. Part I: The Barents Sea Region, *Norwegian Petroleum Directorate Bulletin No 6.* 5-32

Gabrielsen, R.H., Sokoutis, D., Willingshofer, E. & Faleide, J.I. 2016. Fault linkage across weak layers during extension: an experimental approach with reference to the Hoop Fault Complex of the SW Barents Sea. *Petroleum Geoscience.* 22, 123-135

Gingras, M.K., MacEachern, J.A., & Dashtgard, S.E. 2012. The potential of trace fossils as tidal indicators in bays and estuaries. *Sedimentary Geology* 279, 97-106.

Glørstad-Clark, E., Faleide, J.I., Lundschien, B.A. & Nystuen, J.P. 2010. Triassic seismic sequence stratigraphy and paleogeography of the western Barents Sea Area. *Marine and Petroleum Geology,* 27(7), 1448-1475.

Gudlaugsson, S.T., Faleide, J.I., Johansen, S.E. & Breivik, A.J. 1998. Late Palaeozoic structural development of the south-western Barents Sea. *Marine and Petroleum Geology.* 15, 73-102.

Henry, D. 2016. Scanning Electron Microscopy – Cathodoluminescence (SEM-CL). [Electronic]. http://serc.carleton.edu/research_education/geochemsheets/semcl.html (2017-04-15).

Henriksen, E., Ryseth, A.E., Larssen, G.B., Heide, T., Rønning, K., Sollid, K. & Stoupakova, A.V. 2011. Tectonostratigraphy of the greater Barents Sea: implications for petroleum systems. *Geological Society, London, Memoirs,* 35, 163-195

Houseknecht, D.W. 1987. Assessing the Relative Importance of Compaction Processes and Cementation to Reduction of Porosity in Sandstones. *AAPG bulletin,* 71(6), 633-642.

Kjølhamar, B. 2015. *The Hoop Area: new testing ground for geophysical technologies* [Electronic]. http://www.tgs.com/uploadedFiles/CorporateWebsite/Modules/Articles_and_Papers/Articles/2015-05%20GEO%20Expro%20v12%20n3%20-%20TGS%20Hoop%20Basin%20-%20Geophysical%20Technologies.pdf (2016-10-15)

Klein, C. & Philpotts, A. 2013. *Earth Materials – Introduction to Mineralogy and Petrology.* New York: Cambridge University Press.

Magoon, L.B. & Dow, G.D. 1994. The Petroleum System – from source to trap. *AAPG Memoir*, 60, 3-23.

Matlack, K.S., Houseknecht, D.W. & Applin, K.R. 1989. Emplacement of clay into sand by in infiltration. *Journal of Sedimentary Research,* 59.

Mondol, N.H. 2009. Porosity and permeability development in mechanically compacted silt-kaolinite mixtures. *SEG Technical Program Expanded Abstracts,* 28, 2139-2143.

Mondol, N.H. 2015. Well Logging: Principles, Applications and Uncertainties. *In: Petroleum Geoscience: From Sedimentary Environments to Rock Physics.* Edited by Bjørlykke, K. Ed. 2. Berlin: Springer.

Myers, K.J. & Milton N.J. 1996. Outcrop and Well Data. *In: Sequence Stratigraphy.* Edited by Emery, D. & Myers, K.J. Oxford: Blackwell Science Ltd

Mørk, M.B.E. 1999. Compositional variations and provenance of Triassic sandstones from the Barents Shelf. *Journal of Sedimentary Research, 69* (3), 690-710.

Nelson, S.A. 2013. Petrology – Sandstones & Conglomerates. [Electronic]. http://www.tulane.edu/~sanelson/eens212/sandst&cong.htm (2017-01-29)

Nichols, G. 2009. *Sedimentology and Stratigraphy.* Ed. 2 West Sussex: John Wiley and Sons, Ltd.

Norwegian Petroleum Directorate 2014. *CO2 storage atlas: Geology of the Barents Sea.* Stavanger: Norwegian Petroleum Directorate. [Electronic]. http://www.npd.no/en/Publications/Reports/Compiled-CO2-atlas/6-The-Barents-Sea/61-Geology-of-the-Barents-Sea/ (2016-09-12)

Olariu, C., Steel, R.J., Dalrymple, R.W. & Gingras, M.K. 2012. Tidal dunes versus tidal bars: The sedimentological and architectural characteristics of compound dunes in a tidal seaway, the lower Baronia Sandstone (Lower Eocene), Ager Basin, Spain. *Sedimentary Geology* 279, 134-155.

Powers, M.C. 1953. A new roundness scale for sedimentary particles. *Journal of Sedimentary Research,* 23.

Paxton, S.T. Szabo, J.O., Ajdukiewicz, J.M. & Klimentidis, R.E. 2002. Construction of an intergranular volume compaction curve for evaluating and predicting compaction and porosity loss in ridged-grain sandstone reservoirs. *AAPG bulletin, 86(12),* 2047-2067.

Pozer Bue, E.P., & Andresen, A. 2014. Constraining depositional models in the Barents Sea region using detrital zircon U-Pb data from Mesozoic sediments in Svalbard. *Geological Society, London, Special Publications 386* (1), 261-279.

Ryseth, A. 2014. Sedimentation at the Jurassic-Triassic boundary, south-west Barents Sea: indication of climate change. *In: From Depositional Systems to Sedimentary Successions on the Norwegian Continental Margin.* West Sussex: John Wiley & Sons, Ltd

Santin, C.E. Abel, M., Goldberg, K. & De Ros, L.F. 2009. PS Automatic Detection of the Degree of Compaction in Reservoir Rocks Based on Visual Knowledge. Poster Presentation at AAPG Annual Convention and Exhibition, Denver, Colorado, June 7-10.

Smelror, M., Basov, V.A. & Norges Geologiske Undersøkelse. 2009. *Atlas: Geological History of the Barents Sea.* Trondheim: Geological Survey of Norway.

Swapp, S. 2017. Scanning Electron Microscopy (SEM). [Electronic]. *http://serc.carleton.edu/research_education/geochemsheets/techniques/SEM.html* (2017.02.17)

Tissot, B.P. & Welte, D.H. 1984. *Petroleum Formation and Occurrence.* Ed. 2. New York: Springer-Verlag Berlin Heidelberg.

Vangdal, B., Midtbø, R.E.A., Litlabø, R. & Johansen A.L. 2014. The Kaolinite to Dickite Transformation as a Geothermometer. *Reservoir Quality of Clastic and Carbonate Rocks: Analysis, Modelling and Prediction: proceedings of a conference,* Geological Society, London, pp. 104.

Wellner, R., Beaubouef, R., Van Wagoner, J., Roberts, H. & Sun, T. 2005. Jet-Plume Depositional Bodies - The Primary Building Blocks of Wax Lake Delta. *Gulf Coast Association of Geological Societies Transactions,* 55

Wilson, M.D. & Pittman E.D. 1977. Authigenic clays in sandstones: recognition and influence on reservoir properties and paleoenvironmental analysis. *Journal of Sedimentary Research,* 47(1).

Worden, R.H. & Burley, S.D. 2003. Sandstone diagenesis: the evolution of sand to stone. *Sandstone Diagenesis: Recent and Ancient, 4,* 3-44

Worden, R.H. & Morad, S. 2003. Clay minerals in sandstones: controls on formation, distribution and evolution. *Clay mineral cements in sandstones,* 1-41.

Worsley, D. 2008. The post-Caledonian development of Svalbard and the western Barents Sea. *Polar Research, 27* (3), 298-317.

10. Appendix

Table 10.1: Summary of well data for Hanssen (7324/-2) and Wisting Central (7324/8-1) respectively *(NPD Fact Pages, 2016).*

Well Data	Hanssen (7324/7-2)	Wisting Central (7324/8-1)
Total depth (mD) [m RKB]	1730.0	930
Final vertical depth (TVD) [m RKB]	1719.0	930
Max Inclination	14.3º	1.6 º
Bottom hole temperature	51 ºC	29 ºC
Water depth	417.5m	398.0m
Kelly Bushing	40.0m	25.0m
Logged interval (mD)	710m-782m	662m-710m
Coordinates	73 º29'27.09" N 24 º14'2.56" E	73 º27'6.18" N 24 º24'15.42" E

Table 10.2: Samples selected from Hanssen (7324/7-2) for petrographic analyses. Facies are colour coded accordingly throughout the study. PC=Point Count, XRD=Bulk-XRD analysis, SEM=Scanning electron microscopy.

Well	Formation	Sample	Depth (mD)	Facies	Petrographic analysis		
					PC	XRD	SEM
Hanssen (7324/7-2)	Fruholmen	A1	779.62	F1	x	x	
		A2	772.66	F2	x	x	
		A3	769.73	F1	x	x	
		A4	767.40	F3	x	x	
		A5	765.48	F4	x	x	
		A6	763.62	F4	x	x	
		A7	761.72	F4	x	x	
		A8	759.74	F4	x	x	
		A9	757.64	F3	x	x	
		A10	755.96	F3	x	x	
		A11	753.90	F4		x	
		A12	752.77	F3	x	x	x
		A13	750.57	F4		x	
		A14	748.64	F3	x	x	
		A15	746.64	F3	x	x	
		A16	744.58	F3	x	x	
		A17	742.91	F3	x	x	x
		A18	735.82	F1			
		A19	735.31	F1	x		
	Nordmela(?)	A20	735.06	F9		x	x

Table 10.3: Samples selected from Wisting Central (7324/8-1) for petrographic analyses. Facies are colour coded accordingly throughout the study. PC=Point Count, XRD=Bulk-XRD analysis, SEM=Scanning electron microscopy.

Well	Formation	Sample	Depth (mD)	Facies	Petrographic analysis		
					PC	XRD	SEM
Wisting Central (7324/8-1)	Fruholmen	B1	707.82	F1		x	
		B2	703.43	F1			
		B3	699.56	F2	x	x	
		B4	697.43	F2	x	x	
		B5	696.58	F3		x	
		B6	695.51	F3	x	x	
		B7	693.77	F4		x	
		B8	689.86	F4	x	x	
		B9	685.41	F3	x	x	
		B10	684.41	F4		x	
		B11	682.68	F3		x	
		B12	680.85	F4	x	x	
	Stø	B13	678.63	F6	x	x	x
		B14	676.47	F6	x	x	x
		B15	674.75	F6	x	x	
		B16	673.82	F6	x	x	
		B17	671.75	F6	x	x	
		B18	668.74	F6	x	x	
		B19	665.57	F6	x	x	
		B20	662.63	F6	x	x	x

Table 10.4. Point count results for Hanssen (7324/7-2). Values are expressed as a percentage of total sample volume.

| Samples | Quartz | | Mica | Feldspar | | | Lithic Fragment | Matrix | Chlorite | Cement | | Kaolinite | Primary Porosity | Secondary Porosity | Unknown | IGV |
	Mono	Poly		Plag	Micro	Altered				Qtz	Calcite					
A1	50.50	3.00	4.25	0.50	1.75	10.75	1.25	2.50	2.00	7.25	1.50	1.75	10.75	2.25	0.00	25.75
A2	42.50	3.50	12.5	2.00	0.50	12.25	5.25	13.75	1.00	2.25	1.50	0.00	3.00	0.00	0.00	21.5
A3	48.25	5.00	10.0	0.25	1.50	9.75	0.00	13.50	3.50	4.75	0.00	2.00	0.50	1.00	0.00	24.25
A4	41.00	5.25	2.00	3.00	0.00	18.00	5.00	4.50	0.00	4.75	0.00	3.00	9.50	4.00	0.00	21.75
A5	43.00	9.50	1.50	0.25	0.00	11.75	5.00	6.00	0.00	3.50	0.00	5.50	8.00	6.00	0.00	23.00
A6	34.00	8.75	2.00	2.50	1.00	11.50	2.50	18.50	1.00	2.75	0.00	8.00	5.50	2.00	0.00	35.75
A7	34.50	6.25	1.50	2.25	0.25	16.50	2.00	23.00	1.50	3.25	0.00	7.00	0.50	1.50	0.00	35.25
A8	37.50	8.25	1.00	2.00	0.75	15.00	2.25	12.25	0.25	2.25	0.00	8.00	9.25	1.25	0.00	32.00
A9	41.25	11.75	0.50	3.25	0.25	17.00	0.00	2.50	0.00	6.50	0.00	2.00	10.75	4.25	0.00	21.75
A10	41.75	8.00	0.50	4.00	0.50	15.50	2.00	4.00	0.50	4.50	0.00	2.25	15.75	0.50	0.25	27.00
A12	47.75	6.75	0.00	2.75	0.75	8.50	1.25	3.75	0.25	6.75	0.00	0.50	15.75	5.25	0.00	27.00
A14	40.75	8.25	2.50	2.75	1.00	10.75	5.50	9.00	0.00	4.50	0.50	4.50	7.00	3.00	0.00	25.50
A15	34.00	12.25	2.00	3.25	0.50	12.50	4.25	7.00	0.00	4.25	0.00	2.25	9.75	8.00	0.00	23.25
A16	25.00	14.50	3.50	3.75	1.00	11.75	3.50	9.25	0.50	1.50	21.25	0.50	3.25	0.25	0.50	36.25
A17	37.50	6.25	4.25	2.50	1.00	14.25	8.00	5.00	0.50	6.50	0.25	3.00	8.25	2.25	0.50	23.50
A19	48.50	4.00	1.50	1.00	1.75	13.75	0.00	22.00	0.50	2.50	0.00	1.50	2.75	0.25	0.00	29.25

Table 10.5. Point count results for Wisting Central (7324/8-1). Values are expressed as a percentage of total sample volume.

Sample	Quartz Mono	Quartz Poly	Mica	Feldspar Plag	Feldspar Micro	Feldspar Altered	Lithic Fragment	Matrix	Chlorite	Cement Qtz	Cement Calcite	Kaolinite	Primary Porosity	Secondary Porosity	Unknown	IGV
B3	46.50	2.50	0.50	2.25	0.75	12.00	1.50	11.25	0.50	1.25	17.50	1.50	0.25	1.75	0.00	32.25
B4	49.25	3.75	0.50	2.75	0.75	9.00	0.50	5.50	0.00	1.50	24.00	2.00	0.25	0.25	0.00	33.25
B6	39.50	9.75	5.00	2.75	2.25	8.75	5.50	8.25	1.00	3.75	0.00	1.50	9.00	0.75	2.25	23.50
B8	41.50	7.25	2.25	1.75	0.25	16.50	0.25	13.00	0.00	2.25	1.00	2.75	9.25	1.50	0.50	28.25
B9	40.50	10.0	4.50	4.00	1.50	10.25	2.25	7.75	1.00	1.75	0.00	4.50	11.50	0.50	0.00	26.50
B12	43.75	6.25	3.00	1.25	0.00	9.25	5.00	18.50	2.50	3.50	0.00	4.00	2.50	0.50	0.00	31.00
B13	58.00	1.75	1.50	1.75	1.25	11.75	1.50	2.25	0.00	6.75	0.00	0.50	11.75	2.25	0.00	21.25
B14	67.00	1.50	0.25	0.25	0.00	6.75	0.00	3.00	0.00	2.50	0.00	0.00	18.75	0.00	0.00	24.25
B15	71.50	0.50	0.00	0.00	0.00	2.75	0.00	1.00	0.00	4.00	0.00	0.00	20.00	0.25	0.00	25.00
B16	61.50	2.00	0.00	0.00	0.00	0.25	0.00	0.50	0.00	0.50	34.75	0.00	0.25	0.25	0.00	36.00
B17	70.25	0.25	0.00	0.00	0.00	0.25	0.00	1.25	0.25	2.25	7.50	0.25	17.50	0.25	0.00	29.00
B18	67.75	1.00	0.25	0.00	0.00	4.25	0.25	0.75	0.00	2.50	0.00	0.00	23.25	0.00	0.00	26.50
B19	74.00	0.75	0.25	0.00	0.00	1.75	0.00	0.00	0.00	4.75	0.00	0.00	18.25	0.25	0.00	23.00
B20	67.50	0.25	0.00	0.00	0.00	2.5	0.00	0.25	0.00	4.25	0.00	0.00	23.25	2.00	0.00	27.75

Table 10.6. XRD-results for Hanssen (7324/7-2). Values are expressed as a percentage of total sample volume.

Samples	Qtz	Plag	K-feld	Albite	Musc/Illite	Kaolinite	Dickite	Calcite	Chlorite	Siderite
A1	71.04	2.59	0.00	13.62	3.79	4.26	0.00	1.25	3.46	0.00
A2	57.89	4.02	2.21	15.08	8.40	2.83	2.69	0.00	4.81	2.07
A3	59.76	8.91	1.27	8.06	12.32	4.62	1.57	0.00	3.85	0.00
A4	63.78	2.94	4.13	12.44	9.09	4.39	1.42	0.00	1.81	0.00
A5	61.57	5.85	6.39	13.68	5.01	2.30	2.57	0.00	2.63	0.00
A6	52.98	9.00	7.48	9.96	11.56	5.28	2.25	0.00	1.48	0.00
A7	48.05	6.42	8.80	9.78	12.01	8.79	2.11	0.00	2.27	1.77
A8	60.18	5.87	4.35	9.75	6.69	4.03	1.62	0.00	3.92	3.59
A9	63.31	12.05	8.49	8.19	2.11	2.88	1.35	0.00	1.62	0.00
A10	64.86	17.80	6.37	0.00	4.20	4.17	0.00	0.00	2.60	0.00
A11	43.30	6.49	7.81	8.14	13.99	12.15	2.08	0.00	4.58	1.46
A12	74.52	10.90	5.09	4.12	0.00	3.89	1.48	0.00	0.00	0.00
A13	42.62	8.84	9.30	7.65	15.16	8.96	2.30	0.00	2.98	2.01
A14	54.09	11.41	7.59	11.65	5.31	4.67	1.49	0.00	3.80	0.00
A15	54.71	11.94	8.45	10.51	5.26	4.11	2.09	0.00	2.92	0.00
A16	48.70	14.33	10.98	0.00	4.81	3.67	3.58	13.94	0.00	0.00
A17	46.92	6.80	7.96	9.49	10.92	5.21	12.7	0.00	0.00	0.00
A20	43.08	4.63	5.54	0.00	16.96	27.10	0.00	0.00	2.75	0.00

Table 10.7. XRD-results for Wisting Central (7324/8-1). Values are expressed as a percentage of total sample volume.

Samples	Qtz	Plag	K-feld	Albite	Musc/Illite	Kaolinite	Dickite	Calcite	Chlorite	Siderite	Pyrite
B1	43.30	24.10	0.00	0.00	15.90	7.30	2.50	0.00	3.52	4.18	0.00
B3	49.59	13.41	8.43	0.00	11.15	5.67	0.00	9.61	2.14	0.00	0.00
B4	50.38	5.39	10.03	2.73	2.10	3.17	1.46	22.37	1.77	0.00	0.00
B5	45.48	5.59	9.40	10.52	11.90	7.50	1.67	0.00	3.52	4.42	0.00
B6	57.25	7.17	10.12	11.42	5.46	4.07	2.01	0.00	2.50	0.00	0.00
B7	31.92	3.33	6.09	7.74	23.52	11.30	6.54	0.00	4.24	5.30	0.00
B8	58.38	4.99	6.74	12.42	8.99	5.47	1.16	0.00	1.86	0.00	0.00
B9	62.27	5.71	9.09	10.62	3.13	3.72	2.48	0.50	2.47	0.00	0.00
B10	48.26	4.25	8.64	7.37	11.76	14.88	1.42	0.00	3.41	0.00	0.00
B11	48.45	6.01	11.08	9.42	10.15	9.66	1.59	0.00	3.48	0.00	0.16
B12	58.15	8.65	10.96	5.86	5.33	5.17	2.60	0.00	3.29	0.00	0.00
B13	83.80	6.71	5.71	1.58	0.00	2.11	0.00	0.00	0.00	0.00	0.00
B14	90.60	7.62	0.00	0.00	0.00	1.78	0.00	0.00	0.00	0.00	0.00
B15	92.66	6.28	0.00	0.00	0.00	0.00	0.00	0.00	0.00	0.00	1.06
B16	65.43	3.33	1.53	0.00	0.00	1.53	0.00	28.19	0.00	0.00	0.00
B17	78.55	5.10	0.00	0.00	0.00	0.00	0.00	16.53	0.00	0.00	0.00
B18	93.23	6.77	0.00	0.00	0.00	0.00	0.00	0.00	0.00	0.00	0.00
B19	92.07	7.92	0.00	0.00	0.00	0.00	0.00	0.00	0.00	0.00	0.00
B20	94.87	3.94	0.00	0.00	0.00	1.13	0.00	0.00	0.00	0.00	0.00